MECHANISTIC INSIGHTS INTO THE ROLE OF MUNC13 IN SYNAPTIC VESICLE DOCKING, PRIMING, AND FUSION

APPROVED BY SUPERVISORY COMMITTEE

Jose Rizo-Rey, Ph.D., Advisor

Xuelian Luo, Ph.D., Committee chair

Luke Rice, Ph.D.

Xuewu Zhang, Ph.D.

DEDICATION

Thanks to all my family, friends, and colleagues. This work wouldn't be possible without your support!

MECHANISTIC INSIGHTS INTO THE ROLE OF MUNC13 IN SYNAPTIC VESICLE DOCKING, PRIMING, AND FUSION

by

BRADLEY JACKSON QUADE

DISSERTATION

Presented to the Faculty of the Graduate School of Biomedical Sciences

The University of Texas Southwestern Medical Center at Dallas

In Partial Fulfillment of the Requirements

For the Degree of

DOCTOR OF PHILOSOPHY

The University of Texas Southwestern Medical Center at Dallas

Dallas, Texas

May, 2019

MECHANISTIC INSIGHTS INTO THE ROLE OF MUNC13 IN SYNAPTIC VESICLE DOCKING, PRIMING, AND FUSION

Publication No._____

Bradley Jackson Quade, Ph.D.

The University of Texas Southwestern Medical Center at Dallas, 2019

Supervising Professor: Jose Rizo-Rey, Ph.D.

Neurotransmitter release is a fundamental aspect of neuronal communication that relies on the fusion of synaptic vesicles with the presynaptic membrane. These fusion events are tightly regulated by the influx of Ca^{2+}, which is sensed by the complex protein machinery at the axon terminal. In order for these Ca^{2+}-mediated fusion events to occur in the correct time and place, protein machines interact with neurotransmitter filled vesicles to dock and prime them for release. Munc13 is one of the essential components of the docking, priming, and fusion machinery.

To understand the role of Munc13 in docking and priming I attempted to structurally characterize the MUN domain and SNARE protein interactions using nuclear magnetic

resonance spectroscopy. Paramagnetic relaxation enhancement and pseudocontact shift experiments were performed to identify the binding site of SNAREs or the SNARE complex on the MUN domain and in both cases the data suggested that there may be binding in multiple locations or that the interactions are promiscuous. I also attempted to crystallize the C_2C domain of Munc13 alone and in the context of larger fragments. I was able to grow crystals of various fragments of Munc13 containing C_2C and adjacent domains, but these crystals were fragile and diffracted poorly. In lieu of a crystal structure, I modeled the C_2C domain based on homologous C2 domains and performed sequence conservation analysis to identify functionally important regions of C_2C that may bind membranes.

Using structural information coupled with reconstitutions, dynamic light scattering, and cryo-electron tomography I explored the functional relevance of membrane binding within the C_1, C_2B, and C_2C domains of Munc13. The C_2C domain was identified as a critical component of Munc13 that enables bridging between liposomes with synaptic vesicle and plasma membrane composition *in vitro* and this bridging ability is integral for synaptic vesicle docking *in vivo*. The C_1C_2B area has a large membrane binding interface that changes depending on the ligands present in the system and this enables Munc13 to modulate the distance between membranes. The ability of Munc13 to regulate the distance between membranes in response to ligands may underlie its role in synaptic plasticity.

TABLE OF CONTENTS

Prior Publications

Bradley Quade, Marcial Camacho, Xiaowei Zhao, Marta Orlando, Thorsten Trimbuch, Junjie Xu, Daniela Nicastro, Christian Rosenmund. Membrane Bridging by Munc13-1 is Crucial for Neurotransmitter Release. Under revision with eLife.

Lijing Su, **Bradley Quade**, Huayi Wang, Liming Sun, Xiaodong Wang, and Josep Rizo, A Plug Release Mechanism for Membrane Permeation by MLKL. *Structure*. 2014, 22(10): 1489-1500.

Xiaoxia Liu, Alpay Burak Seven, Marcial Camacho, Victoria Esser, Junjie Xu, Thorsten Trimbuch, **Bradley Quade**, Lijing Su, Cong Ma, Christian Rosenmund, and Josep Rizo. Functional synergy between the Munc13 C-terminal C1 and C2 domains. *eLife*. 2016, 5: e13696.

Yun-Zu Pan, **Bradley Quade**, Kyle D. Brewer, Monika Szabo, James D. Swarbrick, Bim Graham, and Josep Rizo. Sequence-specific assignment of methyl groups from the neuronal SNARE complex using lanthanide-induced pseudocontact shifts. *Journal of Biomolecular NMR*. 2016, 66(4): 281-293.

Ewa Sitarska, Junjie Xu, Seungmee Park, Xiaoxia Liu, **Bradley Quade**, Karolina Stepien, Kyoko Sugita, Chad A. Brautigam, Shuzo Sugita, and Josep Rizo. Autoinhibition of Munc18-1 modulates synaptobrevin binding and helps to enable Munc13-dependent regulation of membrane fusion. *eLife*. 2017, 6: e24278.

List of Figures

List of Tables

LIST OF ABBREVIATIONS

AP – Action potential

ATP – Adenosine triphosphate

C. elegans - *Caenorhabditis elegans*

Camb – Calmodulin-binding

DAG- Diacylglycerol

DC2 – Dysprosium-1,4,7,10-Tetraazacyclododecane-tetraacetic acid

DiD – 1,1-Dioctadecyl-3,3,3,3-tetramethylindodicarbocyanine

DKO – Double knockout

DLS – Dynamic light scattering

DNA – Deoxyribonucleic acid

DOPS - 1,2- dioleoyl-sn-glycero-3-phospho-L-serine

DOTA – 1,4,7,10-Tetraazacyclododecane-1,4,7-Tris-acetic acid-10-maleimidoethylacetamide

DPC – n-Dodecylphosphocholine

DTT – Dithiothreitol

E. coli – Escherichia coli

EC50 – Half maximal effective concentration

EGTA – Ethylene glycol-bis(β-aminoethyl ether)-N,N,N’,N’-tetraacetic acid

FRET – Fluorescence resonance energy transfer

GST – Glutathione S-transferase

HMQC – Heteronuclear multiple quantum coherence

HSQC – Heteronuclear single quantum coherence

IPTG – Isopropyl β-D-1-thiogalactopyranoside

ISI – Interstimulus interval

LB – Lysogeny broth

Marina blue DHPE – Marine Blue 1,2-Dihexadecanoyl-*sn*-glycero-3-phosphoethanolamine

MBP – Maltose-binding protein

Munc13 – Mammalian uncoordinated 13

Munc18 - Mammalian uncoordinated 18

NBD-PE – 1,2-Dipalmitoyl-*sn*-glycero-3-phosphoethanolamino-N-(7-nitro-2-1,3-benzoxadiazol-4-yl)

Ni-NTA – Nickel-nitrilotriacetic acid

NMR – Nuclear magnetic resonance

NSF - N-ethylmaleimide sensitive fusion protein

OD600 – Optical density at 600 nanometers

PBS – Phosphate buffered saline

PCR – Polymerase chain reaction

PCS – Pseudocontact shift

PDBu – Phorbol 12,13-dibutyrate

PIP - Phosphoinositol

PIP_2 – L--Phosphatidylinositol-4,5-bisphosphate

PKC – Protein kinase C

PLC – Phospholipase C

POPC - 1-palmitoyl-2-oleoyl-sn-glycero-3-phosphocholine

POPE - 1-palmitoyl-2-oleoyl-sn-glycero-3-phosphoethanolamine

PRE – Paramagnetic relaxation enhancement

Pvr – Probability of release

RIM – Rab3 interacting molecule

RRP – Readily releasable pool

SDS-PAGE – Sodium dodecyl sulfate polyacrylamide gel electrophoresis

SEM – Scanning electron micrscopy

SNAP receptor - Soluble NSF attachment protein receptor

SNAP-25 - Synaptosomal nerve associated protein 25

SNARE - SNAP receptor

TCEP – Tris(2-carboxytheyl)phosphine

TEV - Tobacco etch virus

TROSY – Transverse relaxation optimized spectroscopy

UV- Ultraviolet

CHAPTER 1-General Introduction

1.1 The brain, neurons, and synapses

Of all the biological systems in nature, one could argue that the nervous system is the most complex. The nervous system controls the information processing that allows the human body to consciously and subconsciously respond to environmental stimuli. The brain is the main control unit of the nervous system that integrates the signals produced by these environmental stimuli to dictate what needs to happen to maintain homeostasis. The minimal functional unit of the nervous system that propagates these signals is the neuron. Neuron doctrine, the idea that the nervous system is composed of individual neurons, was popularized by Santiago Ramón y Cajal in the late 1800s (Ramón y Cajal, 1909). His highly detailed neurohistological work clearly showed that neurons were individual cells composed of a branching network of dendrites, a cell body, and an axon (Figure 1.1A) and that signals are propagated unidirectionally through a neuron, starting in the dendrite and ending at the axon terminal (Ramón y Cajal, 1909) (Figure 1.1B). Following the seminal work of Ramón y Cajal, Sir Charles Sherrington suggested that signal propagation in the nervous system is regulated at the gap between the axon of one neuron and the dendrite of another neuron, at a structure he called the synapse (Sherrington, 1906). Within the human brain there are an estimated 85 billion neurons with thousands of individual synapses per neuron (Williams and Herrup, 1988). Understanding how signal propagation in neurons is regulated at the synaptic level is a daunting, but necessary, task in figuring out how the human brain functions.

1.2 The synaptic vesicle cycle

Synaptic vesicles are small, protein-rich, 40 nm diameter trafficking organelles containing various neurotransmitters (Takamori et al., 2006). Fusion of synaptic vesicles with the plasma membrane releases the neurotransmitters into the synaptic cleft where they act as the chemical signal that connects neurons. Neurotransmitter binding to the postsynaptic cell converts the chemical signal released by the presynapse into an electrical signal that is propagated through the neuron. The synaptic vesicle cycle is a very tightly regulated process that generally describes the steps that a synaptic vesicle goes through from their genesis to fusion (Figure 1.2) (Sudhof, 2004).

Throughout the years, many mechanisms have been proposed for the formation of synaptic vesicles and they happen over a variety of timescales. Synaptic vesicles can form directly through clathrin-mediated endocytosis at the plasma membrane to serve as a method to quickly create new synaptic vesicles (Gad et al., 1998) or they can be slowly processed through endosomes before budding off into mature vesicles in a clathrin-dependent manner (Hoopmann et al., 2010). Early electron microscopy data suggested that bulk endocytosis and subsequent fission of cisternae can produce synaptic vesicles (Heuser and Reese, 1973). There is also the kiss-and-run hypothesis where synaptic vesicles transiently meet the plasma membrane to release neurotransmitters before being locally recycled independent of endocytosis (Ceccarelli et al., 1973). Regardless of their origin, synaptic vesicles are rapidly acidified by the vesicular H+-ATPase and loaded with neurotransmitters via a proton antiport mechanism (Wang and Hiesinger, 2013). At this point the mature synaptic vesicles are moved near the active zone where they can be processed for neurotransmitter exocytosis. The synaptic vesicles near the

active zone are first brought within ~2 nanometers of the plasma membrane in a step known as docking (Imig et al., 2014). Proteins interact with the docked vesicles to prime them for fast, synchronous neurotransmitter release. This fast release is triggered by a calcium signal that is delivered to the interior of the presynaptic cell by an electrical impulse, also known as an action potential, opening voltage-gated calcium channels and there is less than 400 microseconds between the influx of the calcium and the release of neurotransmitters (Sudhof, 2004). The fast response to calcium is necessary for the nervous system to send signals at high speeds and underlies the fast information processing ability of the human brain.

1.3 The protein machinery

Understanding how calcium influx triggers microsecond scale synaptic vesicle fusion requires an intimate understanding of the protein machinery at the axon terminal. This is not a simple task though. Proteomics data suggest that there are hundreds of different protein species in the presynapse with at least 300,000 individual protein molecules (Abul-Husn et al., 2009, Wilhelm et al., 2014). Genetic studies have identified a core set of proteins that enable synaptic vesicle fusion to occur quickly and efficiently. The genetics studies coupled with a bottom-up biochemical approach has made it possible to understand the interactions between these core components and begin dissecting how they work together to enable fast, synchronous membrane fusion.

1.3.1 The SNAREs and SNARE complex

SNARE proteins are a general family that is involved in all forms of intracellular membrane traffic. The defining characteristic of SNARE proteins is a short, unstructured sequence, known as a SNARE motif, that forms into a highly stable protein complex, known as

the SNARE complex, that mediates fusion (Ungar and Hughson, 2003). The presynaptic SNAREs involved in synaptic vesicle fusion are synaptobrevin-2, syntaxin-1, and SNAP-25 (Sudhof and Rothman, 2009). Synaptobrevin-2 is an integral membrane protein that contains a single SNARE motif with a C-terminal transmembrane region that anchors it to the synaptic vesicle (Figure 1.3) (Hong and Lev, 2014). SNAP-25 contains two SNARE motifs, one N-terminal and one C-terminal, that are separated by a cysteine-rich linker sequence that is palmitoylated to anchor the protein to the plasma membrane (Hong and Lev, 2014). Syntaxin-1 has the most complex architecture, containing a highly conserved helical bundle referred to as the H_{abc} domain as well as a small peptide known as the N-peptide (Fernandez et al., 1998, Khvotchev et al., 2007), a C-terminal transmembrane domain that anchors it to the plasma membrane, and an adjacent SNARE motif.

The necessity of the SNARE proteins for synaptic vesicle fusion was first demonstrated when it was discovered that botulinum-B and tetanus toxin inhibit fusion by cleaving the vesicle associated synaptobrevin-2 (Link et al., 1992, Schiavo et al., 1992). Shortly after, it was shown that synaptobrevin-2 forms a highly stable SNARE complex with syntaxin-1 and SNAP-25 (Sollner et al., 1993a). It was hypothesized that the trans-SNARE complex bridging the synaptic vesicle and plasma membrane provides specificity for the vesicle and target membranes to come together (Hanson et al., 1997), and a widely accepted model suggests that the synaptobrevin-2 and syntaxin-1 SNARE motifs, linkers, and transmembrane segments form continuous helices that can mechanically disrupt the lipid bilayer to promote membrane fusion during SNARE complex formation (Weber et al., 1998). More recently, it was shown that lipid-anchored

SNAREs lacking a transmembrane region can catalyze neurotransmitter release (Zhou et al., 2013), suggesting the previous model is incorrect.

When the structure of the neuronal SNARE complex was solved, it showed that it was a parallel four-helix bundle consisting of one SNARE motif from syntaxin-1 and synaptobrevin-2 and two SNARE motifs from SNAP-25 (Figure 1.3) (Poirier et al., 1998, Sutton et al., 1998). At the core of the SNARE complex there are many hydrophobic residues that contribute to the overall stability of the complex, but in the center there is a highly conserved hydrophilic layer with one polar amino acid from each SNARE motif (Fasshauer et al., 1998). This observation gave rise to the designations Q-SNARE, for SNAREs contributing a glutamine to the polar layer, and R-SNARE, for SNAREs contributing an arginine to the polar layer. In the case of the neuronal SNARE complex syntaxin-1 and SNAP-25 are Q-SNAREs, while synaptobrevin-2 is an R-SNARE.

At this point reconstitution systems were developed for monitoring SNARE-mediated membrane fusion *in vitro*. The most common was a fluorescence assay where dequenching of fluorescently-labeled lipid headgrounds could be monitored as a readout for membrane fusion. When performing these assays with membrane-anchored SNAREs there was lipid mixing over time as SNARE complex formed (Weber et al., 1998). These studies were very exciting at the time because they suggested that the SNAREs alone can indeed catalyze membrane fusion, but the slow speed of lipid mixing, lack of calcium-dependence, and no readout for content mixing meant that there were missing pieces that required further investigation. With time it became clear that many proteins were cooperating to stimulate synaptic vesicle fusion and more needed

to be done to understand how the SNAREs act within the context of the fusion machinery as a whole.

1.3.2 Synaptotagmin-1

Early on it was suggested that calcium stimulates neurotransmitter exocytosis (Katz and Miledi, 1967), but the molecular mechanisms coupling calcium sensing with fast, synchronous release were not clear. Synaptotagmin-1 was originally identified as a 65 kDa protein found on synaptic vesicles with an N-terminal transmembrane domain and two domains with homology to the calcium-sensing C_2 domain of protein kinase C (Figure 1.4) (Matthew et al., 1981, Perin et al., 1990). Shortly after, synaptotagmin-1 was shown to bind phospholipid-membranes in a calcium-dependent manner (Brose et al., 1992). While these observations supported the notion that synaptotagmin-1 is the calcium sensor for neurotransmitter release, this hypothesis was not expanded upon until it was shown that mouse hippocampal cultures exhibited a loss of synchronous release when synaptotagmin-1 is mutated (Geppert et al., 1994). It was fianlly concluded that synaptotagmin-1 is the calcium sensor for synchronous neurotransmitter release when it was demonstrated that mutations that decrease the calcium affinity of synaptotagmin-1 result in a corresponding decrease in the calcium sensitivity of neurotransmitter release in hippocampal cultures (Fernandez-Chacon et al., 2001).

Structural characterization of the C_2A domain of synaptotagmin-1 provided key insights into how synaptotagmins, and other C_2 domain containing proteins, bind calcium (Sutton et al., 1995). The C_2 key fold is a β-sandwich with 8 individual β-strands. In the case of synaptotagmin-1 there are five individual aspartic acids in a set of unstructured loops that coordinate calcium ions. Binding of calcium to these loops increases the overall positive charge

of the loop region to enhance binding to the negatively charged phospholipid headgrounds (Rizo and Sudhof, 1998). Within these calcium binding loops there are also hydrophobic residues that insert into membranes to stabilize the membrane bound state (Fernandez et al., 2001). In many C_2 domains, synaptotagmin included, there are other clusters of basic residues like the RR-motif and polybasic motif that may enable the clustering of membranes (Arac et al., 2006) or mediate protein-protein interactions (Brewer et al., 2015, Zhou et al., 2017). With the wealth of genetic, structural, and biochemical data purporting the role of synaptotagmin-1 as the calcium sensor for neurotransmitter exocytosis, it was an obvious step to see if synaptotagmin-1 enhanced SNARE-mediated fusion *in vitro*. Reconstitution experiments involving the SNAREs and synaptotagmin-1 showed calcium-dependent lipid mixing that was much more efficient than the SNAREs alone (Tucker et al., 2004), but the reactions remained slower than physiological fusion and lacked any regulatory machinery involved with docking and priming.

1.3.3 NSF and α-SNAP

NSF was first identified as a cytosolic and membrane-bound protein that can mediate fusion between transport vesicles and the golgi apparatus (Wilson et al., 1989). Its homology to the yeast Sec18, which was known to be necessary for vesicle-mediated transport between organelles, lead to the idea that this evolutionarily conserved protein may play a role in all forms of intracellular membrane trafficking. Shortly after, the SNAP receptors, α-, β-, and γ-SNAP, were recognized as components of the NSF complex that enabled NSF function (Clary et al., 1990). The NSF/α-SNAP complex was then used as bait in pulldown experiments to determine what proteins it may act upon and it was found to interact with the neuronal syntaxin-1, SNAP-25, and synaptobrevin-2 (Sollner et al., 1993b). The purpose for these interactions became clear

when it was shown that α-SNAP binds to the SNARE complex and that this binding enables NSF to disassemble the SNARE complex (Sollner et al., 1993a).

The recent structure of the 20S complex consisting of NSF, α-SNAP, and the SNARE complex provided further insights into NSF-mediated SNARE complex disassembly (Figure 1.5) (Zhao et al., 2015). Four α-SNAPs bind directly to the SNARE complex with hydrophobic, membrane binding loops near the end of the SNARE complex facing towards where the membrane would be in a cis-SNARE complex. The binding of these hydrophobic loops to the membrane will stabilize the interaction of α-SNAP with the cis-SNARE complex, enabling binding of an NSF hexamer to α-SNAP (Winter et al., 2009). ATP hydrolysis by NSF induces a conformational change that twists the SNARE complex and promotes disassembly. While this is interesting and helps explain NSF-mediated SNARE recycling, it does not provide any insights into the ability of NSF to stimulate fusion. Since it was shown that syntaxin-1 and SNAP-25 can form into a 2:1 SNARE complex that excludes synaptobrevin-2 and serves as a kinetic trap that will stall fusion, there needs to be some component that can break these improperly formed complexes. NSF and α-SNAP can disassemble these 2:1 complexes to help usher the SNAREs through the correct pathway to fusion (Misura et al., 2001) resulting in much more efficient fusion (Ma et al., 2013).

1.3.4 Munc-18-1

In early *C. elegans* genetic screens, it was shown that mutations in the Unc-18 gene, which is primarily found in motor neurons (Gengyo-Ando et al., 1993), results in paralysis, slow growth, and elevated acetylcholine levels (Hosono et al., 1987). Deletion of the mammalian homolog, Munc-18-1, completely abolishes evoked neurotransmitter release, suggesting an

essential role in the fusion machinery (Verhage et al., 2000). This role is validated by the fact that Munc-18-1 forms a stable, high affinity heterodimer with syntaxin-1 (Hata et al., 1993) and binds to the SNARE complex with submicromolar affinity (Dulubova et al., 2007). Interestingly, binding of Munc-18-1 to syntaxin-1 prevents the formation of the SNARE complex (Yang et al., 2000, Dulubova et al., 1999), hinting at a regulatory role in priming. The structure of Munc18-1, bound to syntaxin-1a explained the high affinity interaction between the two proteins and showed how Munc-18 can inhibit the formation of the SNARE complex (Figure 1.6A) (Burkhardt et al., 2008, Misura et al., 2000). The highly acidic H_{abc} domain and H3 linker bind in a basic cavity between two lobes of Munc18-1, burying a large amount of accessible surface area. In the bound conformation, the H_{abc} domain of syntaxin-1 binds back on the SNARE motif, locking it into a closed confirmation that protects the syntaxin-1 SNARE motif from the other SNARE proteins to inhibit SNARE complex formation. In solution studies it was shown that the primary conformation of syntaxin-1 is closed, but there is an open/closed equilibrium that may enable SNARE complex to form at the wrong times (Chen et al., 2008), highlighting the necessity of Munc18-1 in regulating fusion.

Recent studies suggest that Munc18-1 al has the ability to bind to synaptobrevin-2 (Xu et al., 2010) and that this binding is necessary for the stimulation of liposome lipid mixing by Munc18-1 in reconstituted systems (Parisotto et al., 2014). The structures of the yeast homolog of Munc18 bound to the yeast homologs of synaptobrevin and syntaxin-1 suggest that SNARE complex formation is templated by Munc18 (Baker et al., 2015) and that a conformational change in the synaptobrevin-binding loop releases an autoinhibitory mechanism that initiates the formation of a syntaxin-1/synaptobrevin/Munc18 complex (Figure 1.6B)(Sitarska et al., 2017).

Mutations that release this autoinhibitory mechanism are gain-of-function due to accelerated SNARE complex assembly. Taken together these results suggest that Munc18 may enhance fusion by chaperoning the SNAREs through the correct pathway to creating active, fusogenic SNARE complex.

1.3.5 Munc13-1

In the *C. elegans* genetic screens that identified unc-18, another protein called unc-13 was shown to be essential for locomotion and proper acetylcholine release (Brenner, 1974, Hosono and Kamiya, 1991, Hosono et al., 1987). The unc-13 protein is highly conserved through evolution, with five isoforms found in mammals (Brose et al., 1995, Wojcik et al., 2013). Munc13-1 is the major brain-specific isoform in the Munc13 family and is a large, multidomain protein containing three C_2 domains, a C_1 domain, and a MUN domain (Figure 1.7A) (Brose et al., 1995, Basu et al., 2005). Munc13-1 is a plasma membrane-associated peripheral membrane protein localized to the active zone of synapses (Betz et al., 1998). Knockout of Munc13-1 severely impairs neurotransmission, resulting in mice dying shortly after birth (Augustin et al., 1999). The reason for this was not clear until it was shown that overexpression of a constitutively open syntaxin-1 can rescue unc-13 removal in *C. elegans* (Richmond et al., 2001). This fact, coupled with the observation that Munc13-1 interacts with syntaxin-1 (Betz et al., 1997), suggested that Munc13-1 may be involved in synaptic vesicle priming by promoting the opening of the closed conformation of syntaxin-1. To get deeper into the molecular mechanisms underlying the role of Munc13-1 in neurotransmitter exocytosis, many structural, biochemical, and *in vivo* experiments have been performed to understand the individual domains of Munc13-1.

Early on, it was discovered that the N-terminus of Munc13-1 interacts with the active zone protein RIM and this interaction is important for synaptic plasticity and priming (Betz et al., 2001). This interaction is primarily between the RIM2α zinc finger and a short N-terminal fragment of Munc13-1 containing the C_2A domain. Rab3, another synaptic vesicle-associated protein, can interact with a distinct portion of RIM, forming a Munc13-1/Rab3/RIM tripartite complex (Dulubova et al., 2005). This complex may play a role in localizing the synaptic vesicle to the plasma membrane to aid in docking (Camacho et al., 2017). Structural and biochemical characterization of the C_2A domain showed that C_2A can homodimerize and provided insights into how the RIM2α zinc finger binds (Figure 1.7F,G)(Lu et al., 2006). *In vivo* studies using mutant C_2A domains that cannot homodimerize suggested that C_2A homodimerization inhibits Munc13-1-dependent primingand showed that RIM2α zinc finger binding breaks the C_2A homodimer to promote priming (Deng et al., 2011).

DAG is an important lipid second messenger that can act on a variety of cellular pathways (Carrasco and Merida, 2007). In neurons, DAG is primarily found in the plasma membrane and stimulates neurotransmitter exocytosis through binding to the C_1 domain of Munc13-1 (Rhee et al., 2002). The structure of the C_1 domain of Munc13-1 demonstrates that it is a standard C_1 domain, but the orientation of a tryptophan near the DAG binding site may block DAG binding until the binding site undergoes a conformational change (Figure 1.7B) (Shen et al., 2005). More recent work suggests that the C_1 domain of unc-13 may play a role in stabilizing an inhibitory state that prevents priming (Michelassi et al., 2017).

The central C_2B domain of Munc13-1 is a standard C_2 domain that binds membranes in a calcium-dependent manner, but unexpectedly binds membranes independent of calcium as well

(Shin et al., 2010). The crystal structure of the C_2B domain showed that there is a highly charged helix in front of the calcium-binding loops that may enable the calcium-independent membrane binding (Figure 1.7C) (Shin et al., 2010). The large amount of positive charge in the membrane-binding region enhances the affinity of C_2B for liposomes containing negatively charged phospholipids such as phosphoserine, PIP, and PIP_2. Binding of C_2B to PIP_2, which is primarily found in the plasma membrane, and the C_1 domain to DAG may explain in part how Munc13-1 is localized to the plasma membrane. Since calcium stimulates neurotransmitter exocytosis through binding to the C_2 domains of synaptotagmin-1 (Fernandez et al., 2001), it is expected that loss of calcium-binding by Munc13-1 C_2B may decrease evoked neurotransmitter release *in vivo*. Interestingly, the evoked release signal by isolated action potentials is essentially unchanged in a calcium-binding deficient Munc13-1. There is an appreciable decrease in evoked release under repetitive stimulation, suggesting that binding of calcium to C_2B is important for synaptic plasticity (Shin et al., 2010).

The largest isolated domain of Munc13-1, and arguably the core of the protein, is the MUN domain (Basu et al., 2005). MUN-like domains are structurally conserved throughout evolution with low sequence similarity homologs found in a variety of membrane trafficking systems. These include the yeast exocyst complex and the golgi-associated retrograde protein complex (Pei et al., 2009). The MUN domain and its homologs share a long, rod-like architecture made of multiple helical subdomains. The individual subdomains consist of four independent helices and a single long, shared helix (Figure 1.7D) (Li et al., 2011, Yang et al., 2015, Xu et al., 2017). The MUN domain of Munc13-1 can bind to syntaxin-1 and the SNARE complex, suggesting that it may be important for catalyzing the opening of syntaxin-1 (Guan et

al., 2008). This was conclusively demonstrated when the isolated MUN domain was shown to allow SNARE complex formation from the inhibited Munc18-1/syntaxin-1 complex (Ma et al., 2011). More recently it was suggested that the MUN domain may play a role in putting the SNAREs in the correct orientations within the SNARE complex to promote the formation of fusion competent SNARE complex (Lai et al., 2017).

The C-terminal C_2 domain of Munc13-1, C_2C, is the most poorly understood of them all. From the primary sequence it is expected to be a C_2 domain that cannot bind calcium (Nalefski and Falke, 1996), but very little has been done experimentally. One study using yeast two-hybrid screens suggested that C_2C may be involved in syntaxin-1 interactions (Madison et al., 2005). Another suggested that C_2C coupled with the MUN domain is the minimal Munc13-1 fragment necessary for priming (Stevens et al., 2005). The clearest evidence of C_2C function comes from recent studies showing that the addition of the C_2C domain onto the C_1C_2BMUN fragment of Munc13-1 enhances evoked neurotransmitter release *in vivo* and reconstituted membrane fusion *in vitro*, presumably through bridging the synaptic vesicle and plasma membrane (Liu et al., 2016). The molecular mechanisms underlying the C_2C enhanced fusion are still unclear.

1.3.6 Integrating these distinct functions into a single model for neurotransmitter release

Throughout the years of studying these proteins, many interactions and individual functions have been identified. Integrating these functions and interactions into a single model for evoked neurotransmitter release has not been easy. Building up and reconstituting the system *in vitro* has provided some of the greatest conceptual advances in our understanding of how this core machinery regulates fusion. The reconstitutions integrating these eight components demonstrate the importance of these proteins in mediating fusion and suggest that they are core

components of the fusion machinery (Ma et al., 2013, Liu et al., 2016). From these studies a stepwise model that describes the fusion pathway can be proposed (Figure 1.8). First, NSF and α-SNAP disassemble syntaxin-1/SNAP-25 heterodimers, enabling Munc18-1 to rapidly bind to the closed conformation of syntaxin-1 and prevent syntaxin-1/SNAP-25 complex from forming again. From here, Munc13-1 can bridge the liposomes with synaptic vesicle and plasma membrane composition to promote the opening of syntaxin-1 and the templating of the SNARE complex on Munc18-1. At this point the fusion machinery is in a primed state ready for fusion where lipid mixing can occur without content mixing. As soon as calcium is introduced to the system Munc13-1 binds to it to enable fast fusion. After fusion the SNARE complex can be recycled by NSF and α-SNAP to allow this process to happen again. While the exact role of synaptotagmin-1 in this model is not clear, it is likely that synaptogamin-1 bridges membranes and promotes the folding of the C-terminus of the SNARE complex. While there are many refinements that can be made to this model such as the addition of other proteins, increasing time resolution of the measurements, and looking at single fusion events, this serves as an important starting point for integrating the core machinery into a single model of physiological membrane fusion.

1.4 Munc13-1 and Presynaptic Plasticity

While it is important to characterize the molecular mechanisms guiding neurotransmitter release, it is arguably more interesting from the perspective of neuroscience to understand how learning and memory are encoded in neuronal circuits. The ability of neurons to form neuronal circuits comes from tuning synaptic strength, a process known as synaptic plasticity. Short-term presynaptic plasticity, ranging from milliseconds to minutes, is thought to arise primarily from

changes in release probability at a given synapse (Citri and Malenka, 2008). This can result in an increase in neuronal strength, known as facilitation, or a decrease in neuronal strength, known as depression. It has been proposed that many mechanisms of short-term presynaptic plasticity arise from buildup of intracellular calcium when a neuron is stimulated and that direct sensing of intracellular calcium by various proteins plays a significant role in facilitation. It has also been shown that modulation of biochemical signaling due to phosphorylation can also impact synaptic plasticity (Rosahl et al., 1993). Short-term presynaptic depression, typically seen in very strong synapses like the frog neuromuscular junction, may result from depletion of the readily releasable pool of vesicles (Betz, 1970), but modulation can also occur from postsynaptic mechanisms such as desensitization of neurotransmitter receptors (Papke et al., 2011).

Munc13-1 was identified as a major regulator of short-term plasticity when it was shown that disrupting the C_1 domain with the H567K mutant significantly increases synaptic depression under stimulation even though single action potential evoked release is essentially unchanged (Rhee et al., 2002). Since presynaptic localization of H567K mutant Munc13-1 is the same as wild-type, it is likely that the DAG binding to Munc13-1 has a direct impact on biochemical signaling. More recently, the C_2B domain of Munc13-2 was implicated in synaptic plasticity when it was shown that mutating calcium binding significantly increases synaptic depression under stimulation relative to wild-type, while single action potential evoked release is unchanged (Shin et al., 2010). Binding of DAG and calcium to the Munc13 family may underlie its ability to regulate synaptic weight by influencing release probabilities at distinct release sites (Sakamoto et al., 2018). In addition to interacting with various ligands to influence plasticity, Munc13-1 has also been implicated in protein-protein interactions that may directly link it to long-term forms of

plasticity (Dulubova et al., 2005). RIMs and RABs, two protein families known to interact with Munc13-1, have been directly implicated in long-term potentiation (Castillo et al., 1997, Castillo et al., 2002, Schoch et al., 2002), providing a possible link between Munc13-1 and long-term plasticity. Despite the growing evidence of the involvement of Munc13-1 in presynaptic plasticity, little is understood about the molecular mechanisms by which Munc13-1 regulates plasticity.

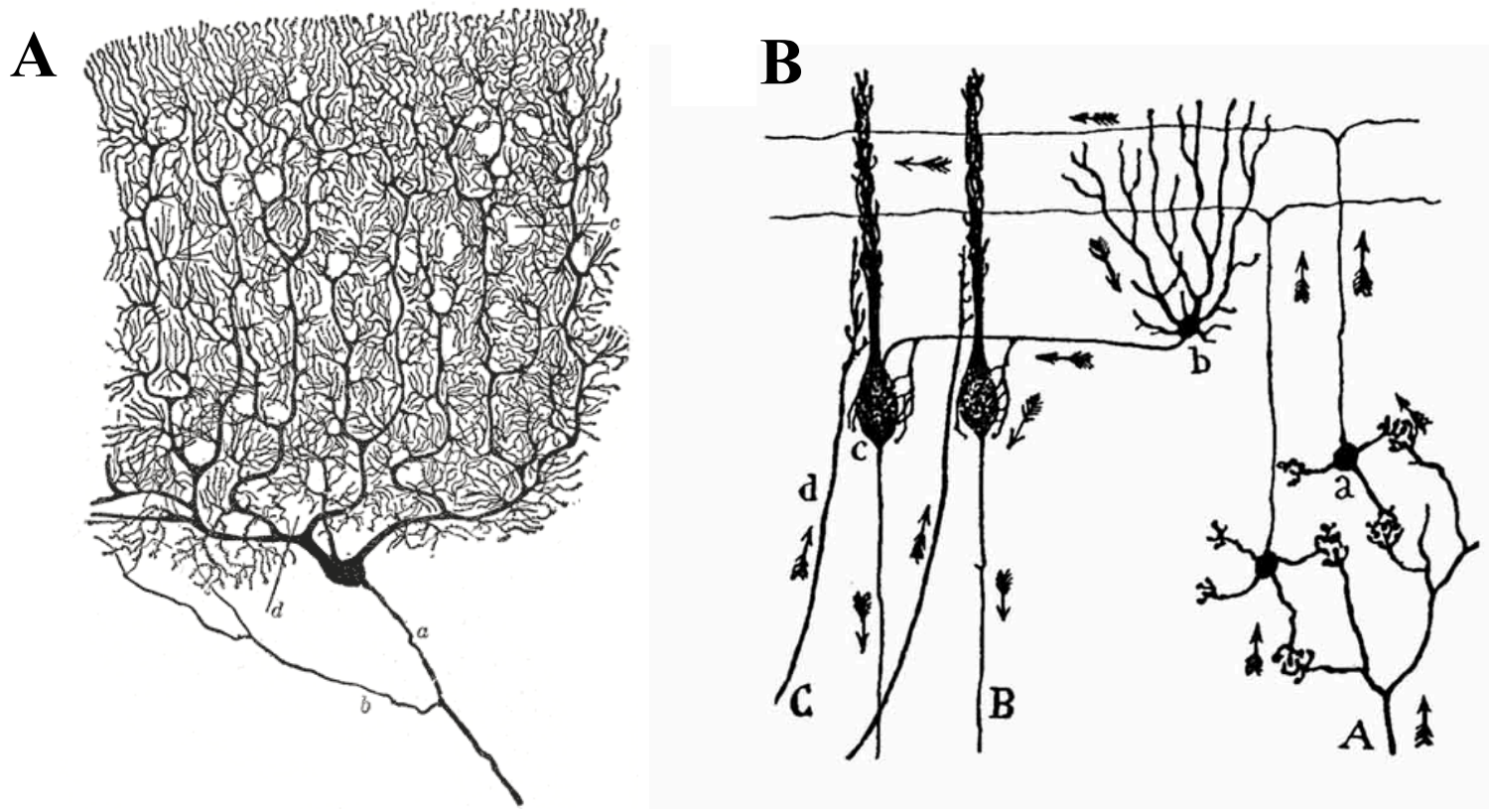

Figure 1.1 Illustrations of neurons and neural connections by Santiago Ramón y Cajal
Using a silver staining method developed by Camillo Golgi, Ramón y Cajal explored and illustrated the anatomy of Purkinje cells in the cerebellar cortex (A) and the connectivity of the cerebellar cortical circuit (B), among many other neuronal systems. The Purkinje cell illustration shows a dense array of dendrites, a cell body, and axons (labeled a and b), while the cerebellar cortical circuit demonstrates that dendrites receive information from the axonal projections of other cells (Ramón y Cajal, 1909).

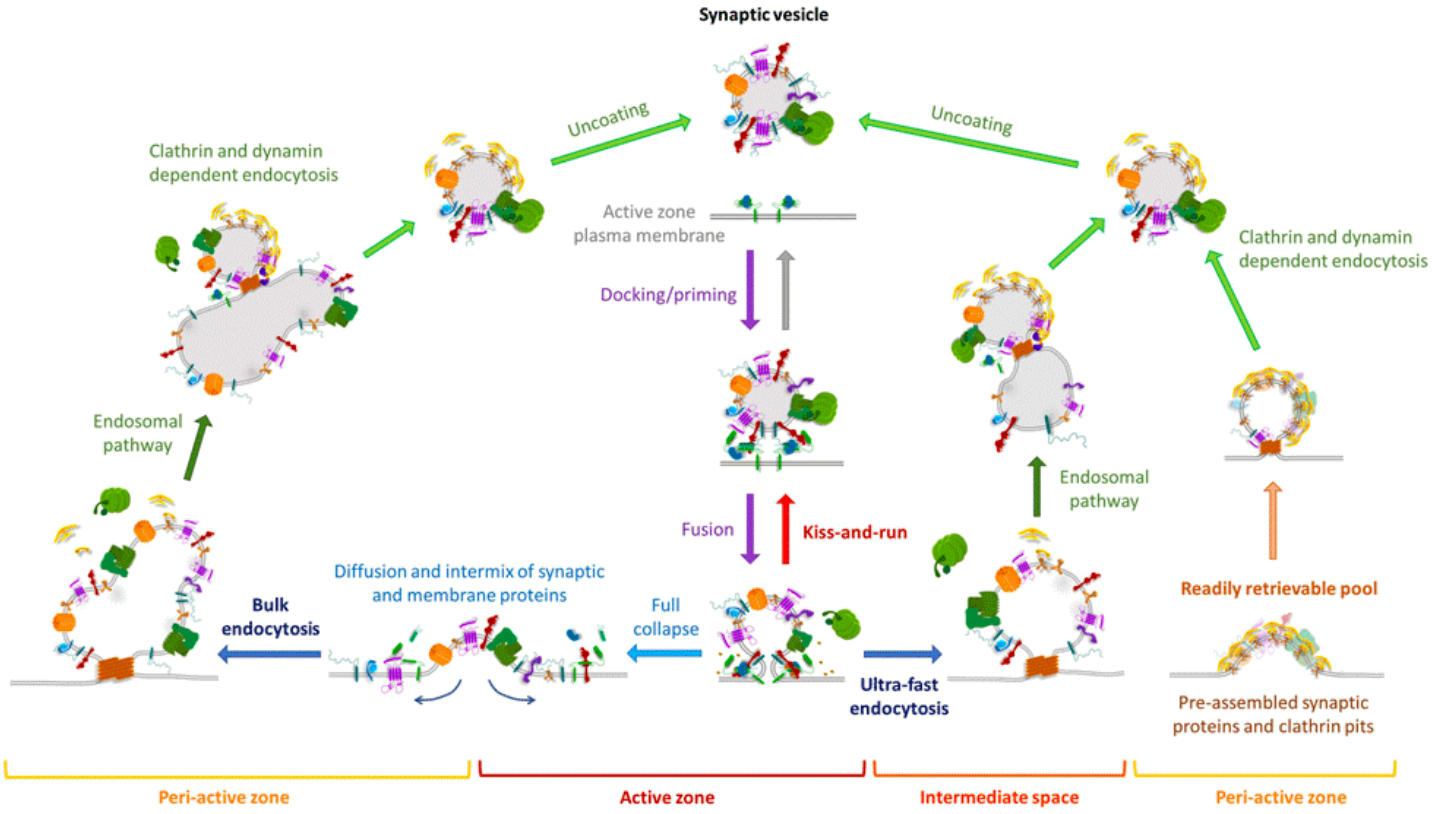

Figure 1.2 Summary of the synaptic vesicle cycle
After docking, priming, and fusion (purple arrows, center), synaptic vesicles are rapidly recycled by closing the fusion pore (kiss-and-run, central red arrow) or they can fully fuse and the components of the synaptic vesicle are integrated into the plasma membrane (light blue arrow, center). Endocytosis can occur through ultra-fast mechanisms (blue arrow, bottom right) or through slower bulk endocytosis (blue arrow, bottom left), both of which proceed through the endosomal pathway. Either way, clathrin-mediated mechanisms (green arrows, left and right) drive endosomal synaptic vesicle formation. Synaptic vesicles can also be rapidly formed directly from the plasma membrane using clathrin-mediated mechanisms (bottom right, orange arrow). Figure and text adapted from Chanaday and Kavalali, 2017.

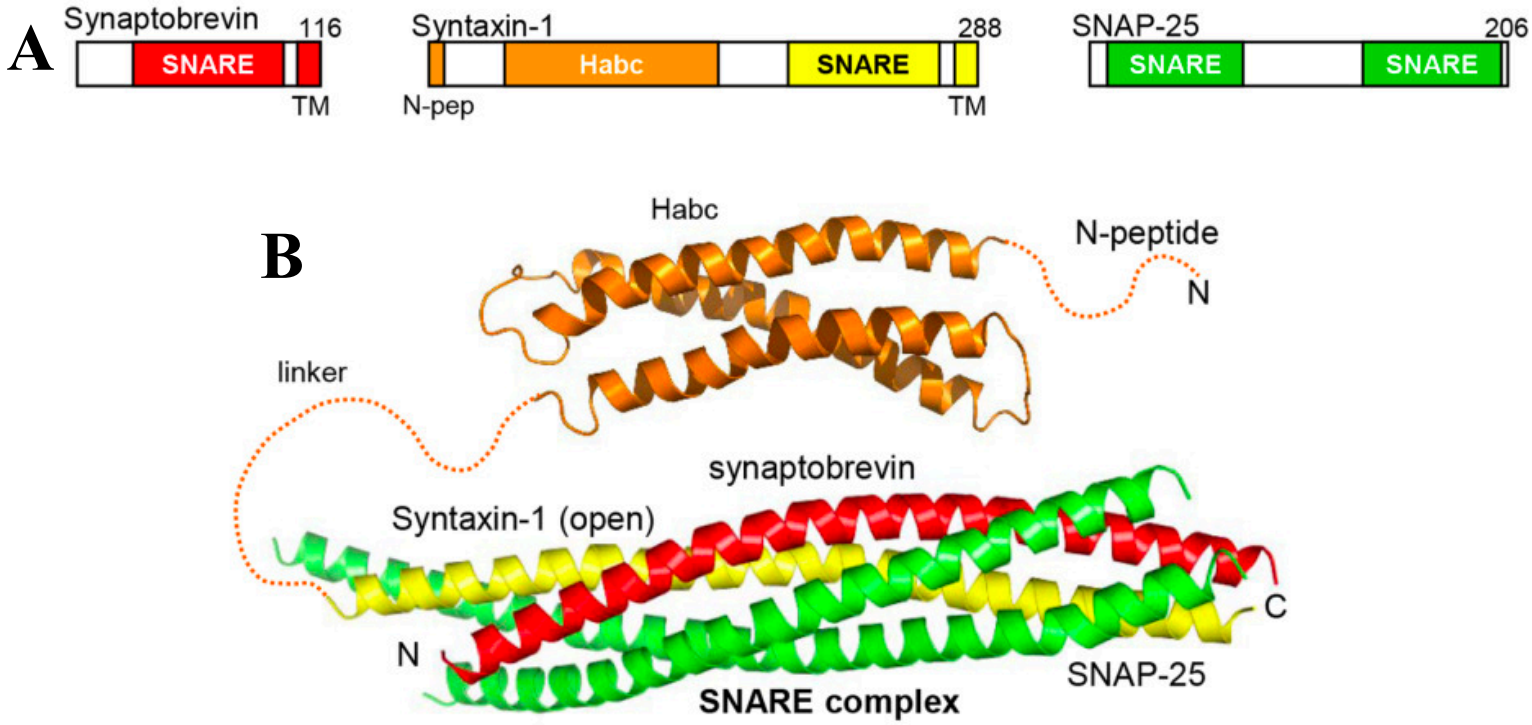

Figure 1.3 Domain architecture of the SNARE proteins and the structure of the SNARE complex and syntaxin H_{abc} domain

(A) The domain architecture of the three neuronal SNARE proteins synaptobrevin-2, syntaxin-1, and SNAP-25. The SNARE motifs are labeled SNARE while the synaptobrevin-2 and syntaxin-1 C-terminal transmembrane regions are labeled TM. Syntaxin-1 contains an N-terminal peptide implicated in Munc18-1-binding labeled N-pep and a regulatory H_{abc} domain represented by H_{abc}. (B) Ribbon diagrams of the neuronal SNARE complex (PDB ID 1SFC) and the structure of the syntaxin H_{abc} domain (PDB ID 1BR0) with N- and C-termini of the SNAREs labeled (Sutton et al., 1998. Fernandez et al., 1998). Dashed lines indicate flexible regions unresolved in the structures. Figure and text adapted from Rizo, 2018.

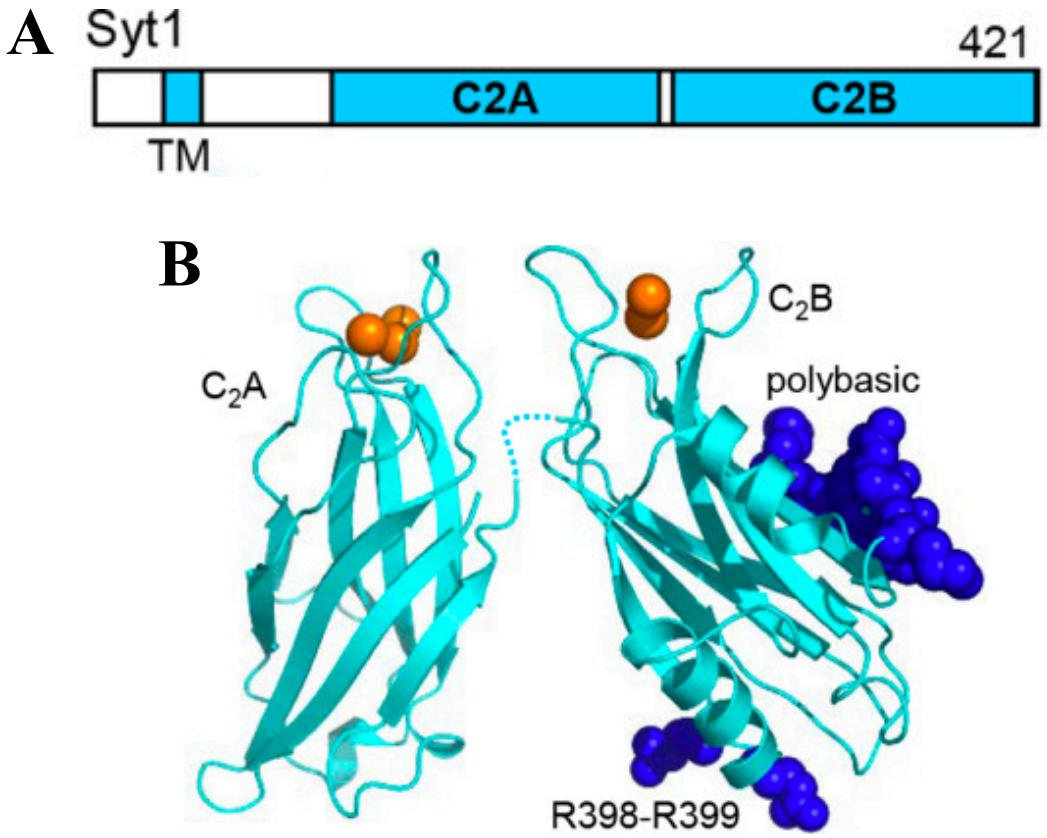

Figure 1.4 Domain architecture and structure of synaptotagmin-1
(A) Synaptotagmin-1 consists of an N-terminal transmembrane region anchoring it to the synaptic vesicle and tandem C2 domains labeled C2A and C2B. (B) Ribbon diagrams of calcium-bound C2A (PDB ID 1BYN) and C2B (PDB ID 1K5W) (Shao et al., 1998, Fernandez et al., 2001). Calcium ions are denoted by orange spheres. The RR motif and polybasic motif in C2B are labeled with blue spheres to highlight two distinct functionally relevant areas. Figure and text adapted from Rizo, 2018.

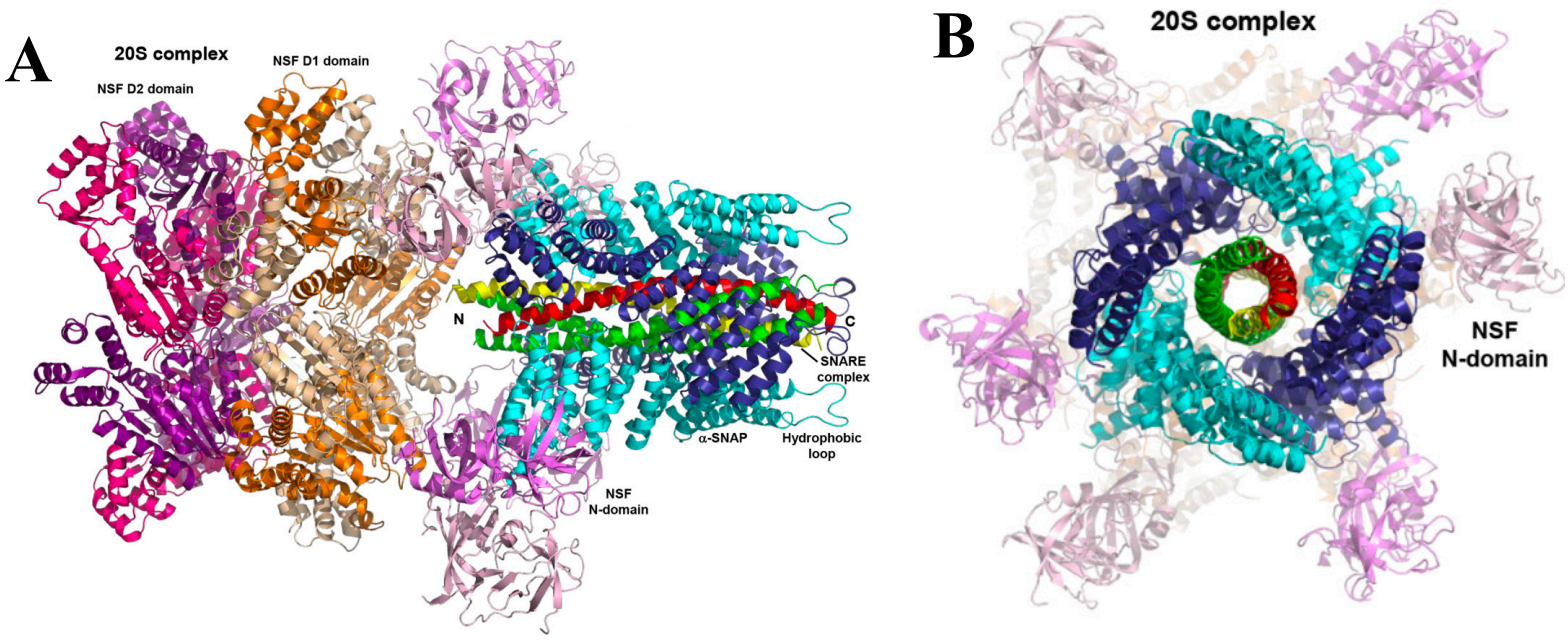

Figure 1.5 Structure of the 20S complex

Ribbon diagrams of the side view (A) and top view (B) of the 20S complex (PDB ID 3J96) consisting of an NSF hexamer, four α-SNAPs, and the SNARE complex (Zhao et al., 2015). The C-terminus of the SNARE complex is lined up with the membrane binding hydrophobic loops of α-SNAP, providing an attachment point for the disassembly of cis-SNARE complex. Figure and text adapted from Rizo, 2018.

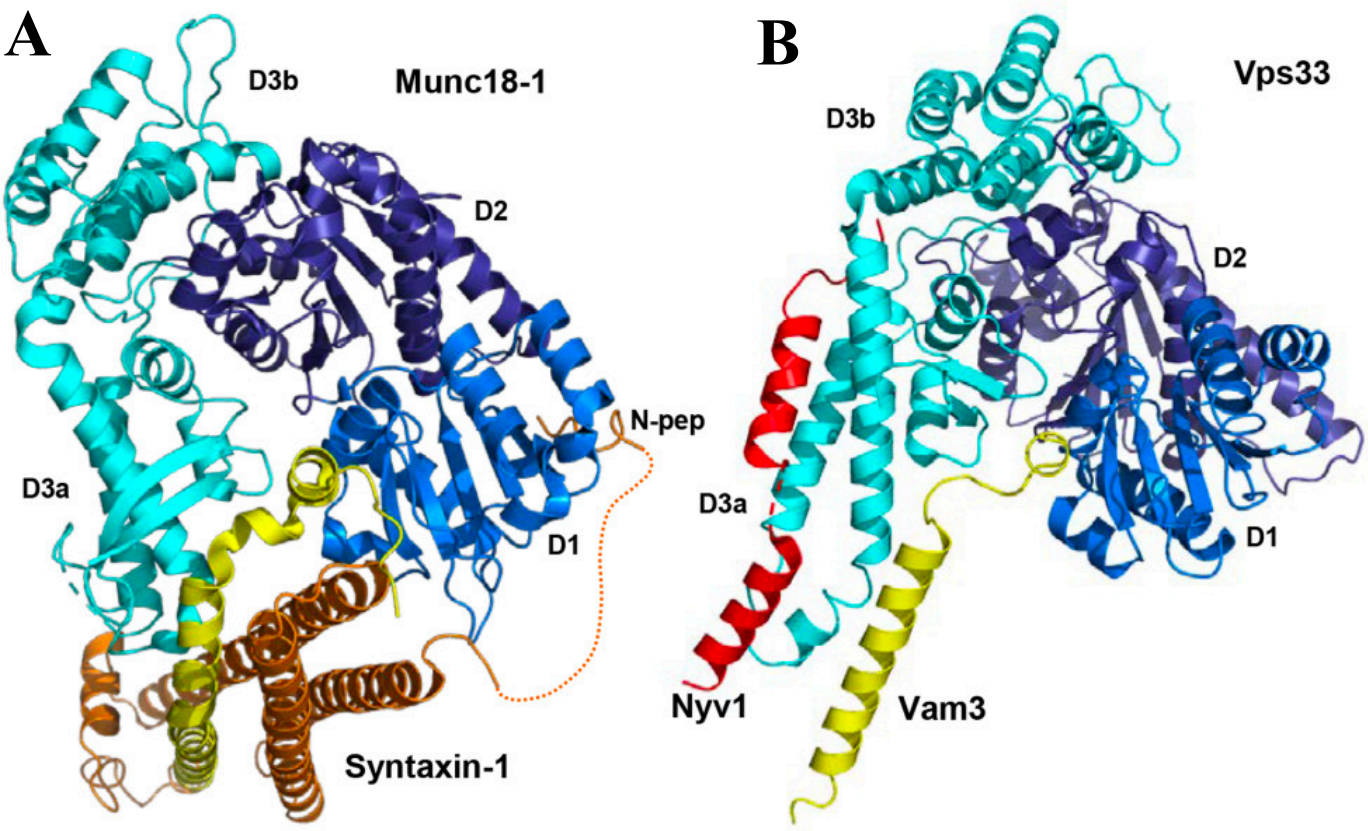

Figure 1.6 Structures of SM protein/SNARE complexes

(A) Ribbon diagram of the Munc18-1/syntaxin-1 complex (PDB ID 3C98) (Misura et al., 2000). Syntaxin-1 is nestled between the D1 and D3a domains of Munc18-1 with the syntaxin-1 SNARE motif (yellow) covered by the folded H_{abc} domain (orange), explaining the ability of Munc18-1 to inhibit SNARE complex formation. (B) Superposition of the structures of the yeast Munc18 homolog Vps33 bound to the yeast synaptobrevin homolog Nyv1 (PDB ID 5BUZ) and the yeast syntaxin homolog Vam3 (PDB ID 5BZ0) (Baker et al., 2015). The Nyv1 and Vam3 SNARE motifs bind to distinct areas on the D3a domain, providing a mechanism to template the formation of the SNARE complex. Figure and text adapted from Rizo, 2018.

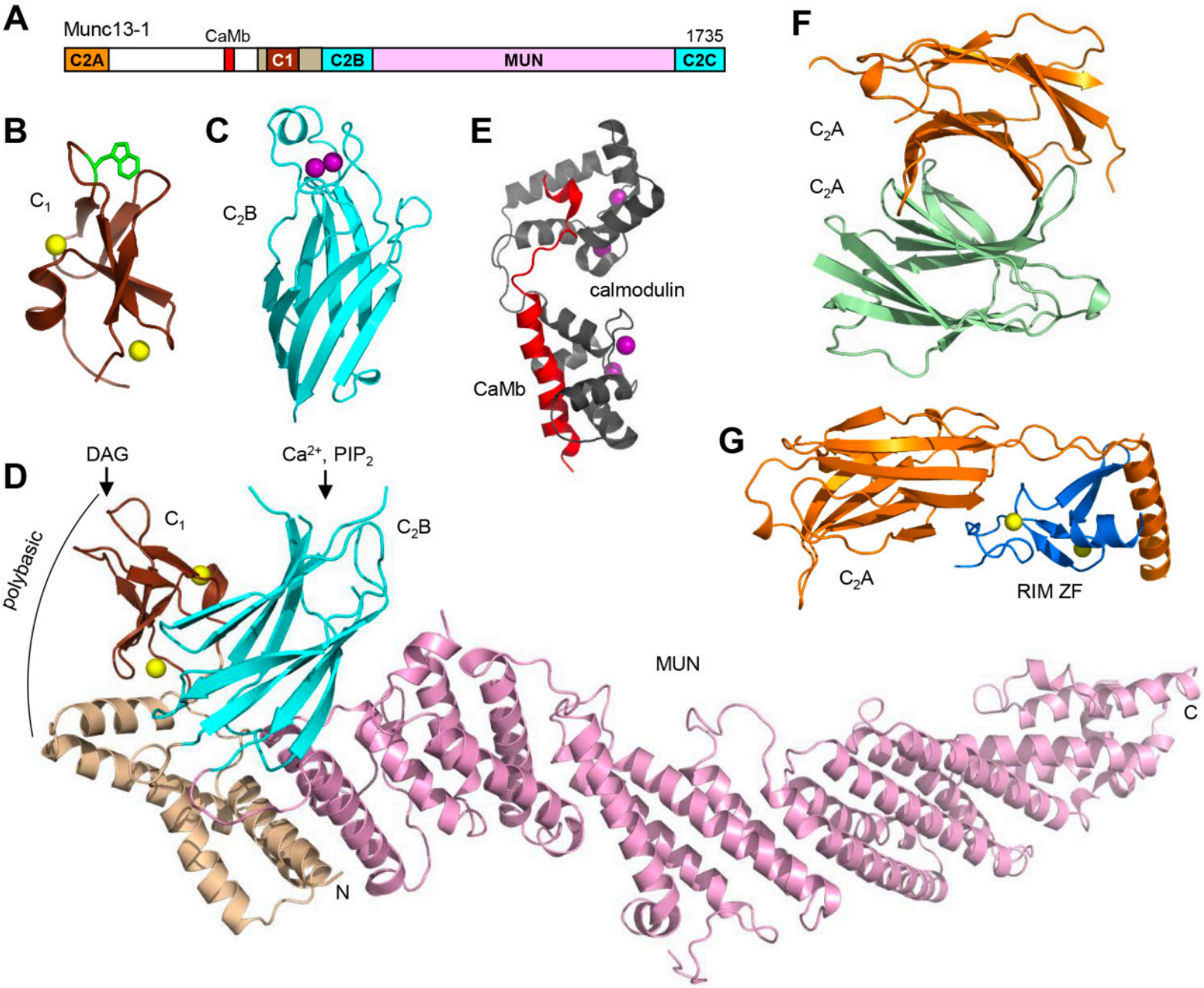

Figure 1.7 Domain architecture of Munc13-1 with structures of various fragments
(A) The domain architecture of Munc13-1 with the calmodulin-binding region labeled CaMb. (B) Ribbon diagram of the C_1 domain (PDB ID 1Y8F) with the DAG-sensing tryptophan labeled with green sticks (Shen et al., 2005). (C) Ribbon diagram of the calcium-bound C_2B domain (PDB ID 3KWU) (Shin et al., 2010). (D) Ribbon diagram of the C_1C_2BMUN fragment (PDB ID 5UE8) with arrows pointing to the calcium and PIP_2 binding region of C_2B and the DAG binding region of C_1. A highly basic patch on the sides of C1 and C2B is labeled polybasic (Xu et al., 2017). (E) Ribbon diagram of the calmodulin binding sequence of Munc13 and calmodulin (PDB ID 2KDU)(Rodriguez-Castaneda et al., 2010). (F,G) The ribbon diagrams of the C_2A homodimer (PDB ID 2JCT) and the C_2A/RIM zinc finger complex (PDB ID 2JCS) (Lu et al., 2006). Calcium ions are represented by purple spheres and zinc ions are represented by yellow spheres. Figure and text adapted from Rizo, 2018.

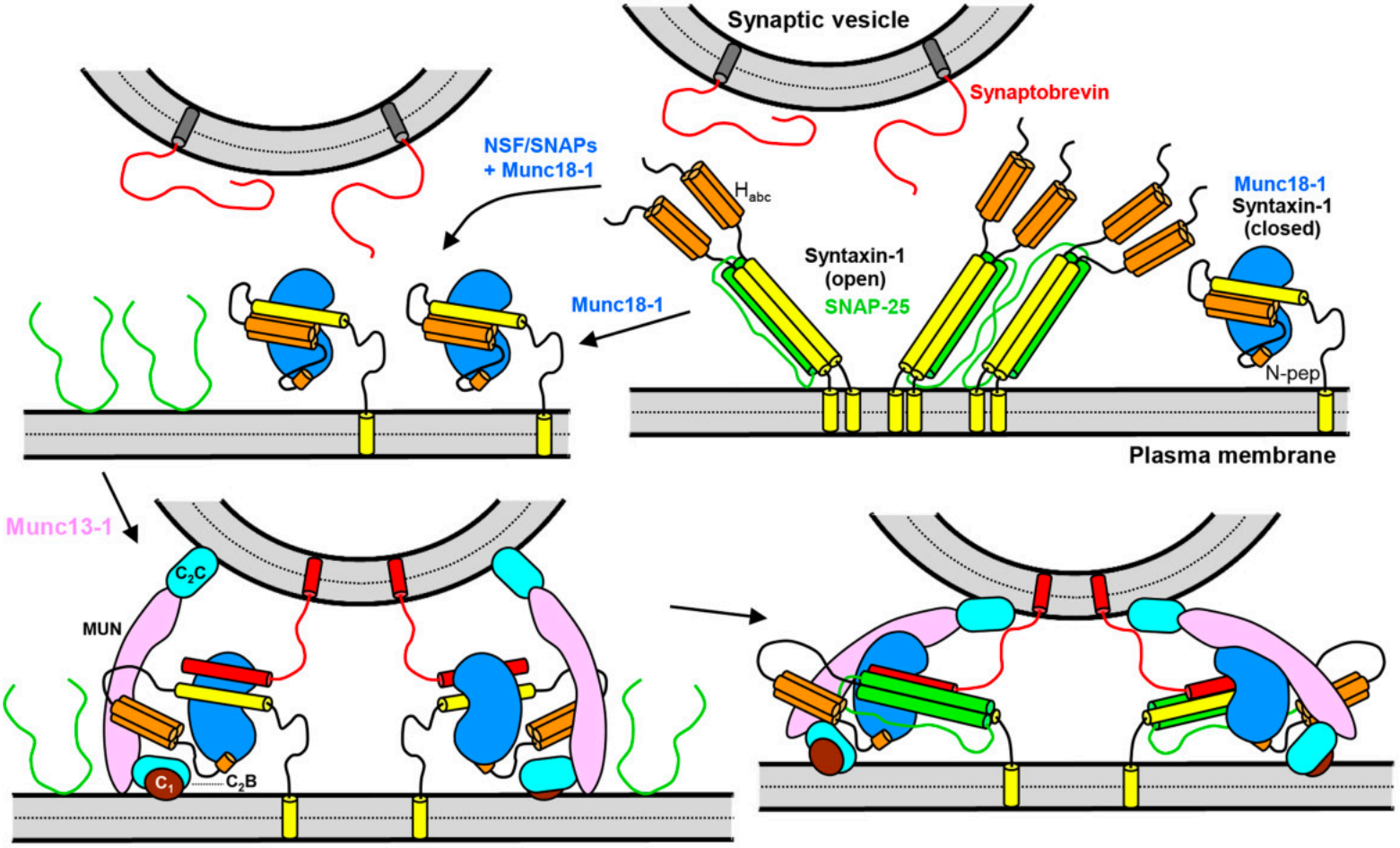

Figure 1.8 A basic model describing the role of the core machinery in fusion
Syntaxin and SNAP-25 in the plasma membrane exist as a 2:1 heterodimer that is broken by NSF and α-SNAP. This leaves syntaxin to form the Munc18/syntaxin complex that serves as the proper starting point for physiological fusion. Munc13 bridges the synaptic vesicle and plasma mebrane, bringing the two membranes close together and opening syntaxin from the Munc18-mediated closed conformation. Formation of the N-terminus of the SNARE complex occurs when synaptobrevin-2 and syntaxin-1 simultaneously bind Munc18-1 and template the formation of the SNARE complex. Upon calcium infux the membranes are brought closer together, the SNARE complex fully forms, and fusion occurs. Figure and text adapted from Rizo, 2018.

CHAPTER 2-NMR studies of the interaction between Munc13-1 and the SNAREs/SNARE complex

2.1 Introduction

At the heart of the intracellular membrane fusion machinery we have the SNARE proteins (Chen and Scheller, 2001, Sudhof and Rothman, 2009, Szule and Coorssen, 2003). While the SNAREs alone can catalyze some lipid mixing, they cannot perform full fusion with content mixing in the absence of other components of the core fusion machinery (Weber et al., 1998, Ma et al., 2013, Liu et al., 2016). Many of these core proteins have been shown to be critical for full fusion *in vivo* and *in vitro* and within this group there are a variety of factors that have been shown to interact with the SNAREs or with the SNARE complex(Rizo, 2018). These interactions can be critical for regulating the formation of the SNARE complex (Sakisaka et al., 2008, Ma et al., 2011) or localizing proteins to the fusion site to perform a specific function that enhances fusion (Wickner and Rizo, 2017). Understanding these interactions at the atomic level is essential for improving our understanding of how the fusion machinery cooperates to orchestrate and enable fast, calcium-dependent fusion.

Of the SNARE-interacting proteins, Munc13-1 and Munc18-1 are two of the most well characterized. Munc13-1 and Munc18-1 are essential for neurotransmitter exocytosis (Verhage et al., 2000, Augustin et al., 1999) and they play major roles in regulating the formation of the SNARE complex (Richmond et al., 2001, Ma et al., 2011). Munc18-1 interacts with the closed conformation of syntaxin-1 with high affinity to prevent SNARE complex formation (Hata et al., 1993, Misura et al., 2000). It has also been demonstrated that synaptobrevin-2 binds to a loop in Munc18-1 after it switches from the furled to unfurled conformation (Baker et al., 2015, Sitarska

et al., 2017, Park et al., 2017). The interactions between Munc18-1 and synaptobrevin-2 or syntaxin-1 are critical for accelerating the formation of the SNARE complex. Munc18-1 also binds to fully formed SNARE complexes with high affinity (Dulubova et al., 2007), but it is not clear if it remains bound during fusion or if it is displaced by other proteins.

The MUN domain of Munc13-1 has also been shown to weakly interact with syntaxin-1 and the membrane-anchored or soluble SNARE complex (Guan et al., 2008, Ma et al., 2011). It was proposed that this interaction underlies the ability of the MUN domain to stimulate the opening of syntaxin-1 to promote the formation of the SNARE complex. Mutations that disrupt this interaction between the SNARE motif and the MUN domain completely abolish MUN-stimulated SNARE complex formation. New evidence demonstrates that that binding of syntaxin-1 and synaptobrevin-2 to the MUN domain promotes the correct orientations between SNAREs in the fully formed SNARE complex and that the presence of Munc18-1 further enhances proper SNARE complex formation (Lai et al., 2017).

It is clear that the interactions between these core proteins and the SNAREs are important for regulating the formation of properly formed, fusogenic SNARE complexes, but the molecular mechanisms underlying these functions are unclear. How do the SNAREs/SNARE complex interact with the MUN domain and how do these interactions enhance calcium-dependent fusion? Structural characterization of these interactions would enable us to answer these questions, but X-ray crystallography, which is most suitable for structure determination of large proteins, is not usable for this particular system. X-ray crystallography requires very homogenous samples with little flexibility and high affinity, but the SNARE/SNARE complex and MUN domain interactions are very weak. In addition, the SNARE motif of syntaxin-1 is

flexible, making it even harder to successfully grow crystals of a MUN/syntaxin-1 complex. NMR spectroscopy, which provides a fingerprint of the protein, is the ideal method to study this system because you can derive structural constraints for weakly interacting and lowly populated species. In addition, flexibility does not hinder the analysis of the interaction. A common way to get structural information for protein-protein interactions using NMR is through analysis of PREs and PCSs. PREs manifest as weakened signals in the NMR spectra and only occur in protein residues that are near a paramagnetic tag. PCSs work in a similar manner, but instead of broadening there are shifts in the spectra that depend on the distance and orientation of the tag relative to the amino acids being monitored. Analysis of PREs or PCSs provide methods for getting distance and orientational restraints that enable structure characterization of weakly interacting complexes with well-resolved spectra (Gillespie and Shortle, 1997, Pintacuda et al., 2006).

2.2 Methods

2.2.1 Construct design and protein expression

All syntaxin constructs are derived from the *Rattus norvegicus* syntaxin-1a. All synaptobrevin constructs are derived from *Rattus norvegicus* synaptobrevin-2. All SNAP-25 constructs are derived from *Homo sapiens* SNAP25A and the SNAP-25 N- and C-terminal SNARE motifs, SN1 and SN3 respectively, contain an N-terminal tryptophan to facilitate UV detection. All Munc13 constructs are derived from *Rattus norvegicus* Munc13-1 and have a disordered loop from 1408-1452 removed to enhance solubility.

Syntaxin 191-236 and its cysteine mutants, syntaxin 191-253, SNAP-25a SN1 11-82, SNAP-25a SN3 141-203, and synpaptobrevin-1 29-93 were all in pETDuet-1 vector with an N-

terminal hexahistidine tag. All constructs were transformed into BL21 (DE3) *E. coli* and grown to an OD_{600} of ~0.8 in ampicillin containing LB media. Constructs uniformly labeled with ^{15}N were grown in M9 minimal media with $^{15}NH_4Cl$ as the sole nitrogen source. Induction was performed with IPTG to a final concentration of 1 mM and expression was allowed to proceed for four hours at 37°C. Cells were harvested by centrifugation, resuspended in cold PBS, and lysed. Cell lysate was clarified by centrifugation at 48,000 x g for 30 minutes and run through Ni-NTA resin 3 times. Bound protein was washed with PBS with 10 mM Imidazole, PBS with 1% Triton X-100, PBS with 1 M NaCl, and eluted with PBS with 0.5 M imidazole. Eluted protein was dialyzed overnight at 4°C in the presence of TEV protease and DTT to remove the His-tag. The next day the protein was run over Ni-NTA resin again to remove free His-tag and any uncleaved protein. Protein was concentrated and gel filtration was performed in a Superdex 75 16/60 with a suitable NMR buffer. Cysteine mutants were incubated with 5 mM DTT prior to gel filtration and the elution buffer was thoroughly degassed to prevent oxidation of cysteines.

MUN 859-1516Δ1408-1452 and $MUNC_2C$ 859-1735Δ1408-1452 in pGEX vector were transformed into BL21 (DE3) *E. coli* and grown in ampicillin containing LB media until induction at an OD_{600} of ~0.8. Induction was performed overnight at 16°C with 0.5 mM IPTG. After expression the cells were harvested by centrifugation, resuspended in cold PBS with 1 mM DTT, and lysed. Cell lysate was spun at 48,000 x g for 30 minutes to clarify the lysate and then incubated with Glutathione Sepharose 4B resin (GE) at room temperature for 1 hour or overnight at 4°C. Bound protein was washed using PBS and PBS with 1 M NaCl. To eliminate any bound DNA, nuclease treatment was performed on the beads for 1 hour at room temperature with 250 U of Pierce Universal Nuclease (Thermo Fisher Scientific) per liter of culture. Resin-bound protein

was washed again with PBS, PBS with 1 M NaCl, and thrombin cleavage buffer (50 mM Tris, pH 8, 250 mM NaCl, 1 mM TCEP, 2.5 mM $CaCl_2$, 10% glycerol (v/v)). Thrombin cleavage was performed on the beads overnight at 4°C and protein was eluted the following day by washing with thrombin cleavage buffer. Eluted protein was diluted twentyfold and subjected to anion exchange chromatography using a HiTrapQ HP column (GE Life Sciences). Protein was eluted in 20 mM Tris, pH 8, 1 mM TCEP, 10% glycerol (v/v) with a linear gradient from 1% to 50% of 1 M NaCl. The protein was concentrated at room temperature and subjected to gel filtration in a Superdex 200 16/60 column (GE Life Sciences). MUN and $MUNC_2C$ were eluted using 20 mM Tris, pH 8, 250 mM NaCl, 1 mM TCEP, 10% glycerol. After gel filtration the protein was concentrated at room temperature.

Expression of ^{2}H-$^{13}CH_3$-Ile, δ1-Leu, γ1-Val, Met- MUN 859-1516Δ1408-1452 was performed similar to previously described (Ma et al., 2011). Briefly, the designated Munc13 fragment was grown in 99.9% D_2O M9 media supplemented with ^{2}H D-glucose until an OD_{600} of ~0.8. Ethyl 2-hydroxy-2-methyl-D3-3-oxobutanoate-4-^{13}C was diluted to 0.2 M in 9 g/L Na_2HPO_4 and incubated with a 1.5 M excess of NaOH for 5 minutes to prepare the compound for stereospecific labeling of leucine and valine residues. Prior to induction the cultures were cooled to 16°C and the leucine and valine compound was added. After 30 minutes [3,3-$^{2}H_2$] ^{13}C-methyl α-ketobutyric acid and ^{13}C-methyl methionine were added and incubated for an additional 30 minutes. The cultures were induced with 0.5 mM IPTG overnight. The protein was harvested and purified by affinity chromatography using the protocol previously described.

Syntaxin-1 2-253, SNAP-25a SN1 11-82 D41C, and SNAP-25a SN3 141-203 D166C were in pGEX vector with an N-terminal GST tag. All constructs were transformed into BL21

(DE3) *E. coli* and grown to an OD_{600} of ~0.8 in ampicillin containing LB media. Constructs uniformly labeled with ^{15}N were grown in M9 minimal media with $^{15}NH_4Cl$ as the sole nitrogen source. Induction was performed with IPTG to a final concentration of 0.5 mM and expression was allowed to proceed overnight at 22°C. Cells were harvested by centrifugation, resuspended in cold PBS, and lysed. Cell lysate was clarified by centrifugation at 48,000 x g for 30 minutes and incubated with Glutathione Sepharose 4B resin (GE) overnight at 4°C in the presence of protease inhibitors. The next day bound protein was washed with PBS, PBS with 1% Triton X-100, and PBS with 1 M NaCl. Syntaxin-1 2-253 was treated with 250 U of Pierce Universal Nuclease on the beads before proceeding. Next, the proteins were washed with thrombin cleavage buffer (50 mM Tris, pH 8, 250 mM NaCl, 1 mM TCEP, 2.5 mM $CaCl_2$) and incubated for 1 hour at room temperature in the presence of thrombin protease. Protein was eluted and concentrated. Syntaxin-1 2-253 was subjected to ion exchange chromatography on a HiTrap Q HP column (GE Life Sciences) and gel filtration chromatography on a Superdex 75 16/60 (GE Life Sciences) while SNAP-25 SN1 and SN3 were purified by gel filtration on a Superdex 75 16/60 (GE Life Sciences) only. Prior to gel filtration the gel filtration buffer was thoroughly degassed while the SN1 and SN3 constructs were incubated with 5 mM DTT.

2.2.2 Protein labeling

1,4,7,10-tetraazacyclododecane-1,4,7-tris-acetic acid-10-maleimidoethylacetamide (DOTA) (Macrocyclics) was dissolved in 50 mM Tris, pH 8, 150 mM NaCl and the pH was adjusted to 7.0. $GdCl_3$ or $LaCl_3$ was added to match the final concentration of DOTA to minimize free gadolinium or lanthanum ions in the sample. Tag was added to the designated cysteine mutant at a ten times molar ratio in the presence of 300 μM TCEP, the pH was adjusted

to 7.2, and the reaction was allowed to proceed for 1 hour at room temperature. Unreacted tag was removed by five rounds of concentration and dilution.

Purified SN1 D41C and SN3 D166C in 20 mM Tris, pH 7.4, 125 mM NaCl were mixed with 1,4,7,10 tetraazacyclododecane-tetraacetic acid loaded with Dy^{3+} (DC2) at room temperature for 30 minutes. Throughout the course of the reaction the UV absorbance of the DC2 leaving group was measured at 345 nm to validate that the concentration of reacted tag is similar to the protein concentration. The DC2 leaving group has an extinction coefficient of 8600 M^{-1} cm^{-1} at 345 nanometers.

2.2.3 SNARE Complex Formation

Mini core SNARE complexes with ^{15}N-syntaxin-1 191-253 were formed by mixing SN1, SN3, and synaptobrevin at a 1.5 fold molar excess over the labeled syntaxin-1 in 20 mM Tris, pH 7.4, 125 mM NaCl overnight at 4°C. The same process was followed for ^{15}N-synaptobrevin SNARE complexes with DC2-labeled SN1 and SN3. The following day the SNARE complex was concentrated and diluted five times to remove free SNAREs and any free DC2 tag.

SNARE complexes with ^{15}N-syntaxin-1 2-253 were prepared by mixing the SNAREs at a 1.5 fold molar excess over the labeled Syntaxin-1 in 20 mM Tris, pH 7.4, 1 M NaCl overnight at 4°C. The following day the SNARE complex was concentrated and diluted five times to remove free SNAREs.

2.2.4 NMR Spectroscopy

All NMR spectra were acquired on Agilent DD2 spectrometers operating at 800 or 600 mHz. All data were processed with NMRpipe (Delaglio et al., 1995) and analyzed in NMRView (Johnson and Blevins, 1994).

2.2.5 Monitoring SNARE complex assembly using native gels

SNARE complex formation assays were performed essentially as described previously (Yang et al., 2015, Sitarska et al., 2017). Briefly, WT Munc18-1 (6 μM) was incubated with syntaxin-1 (2–253) (5 μM) for 20 min at room temperature. Synaptobrevin (29–93) (10 μM), SNAP-25 (10 μM), and the specified Munc13-1 fragment (5 μM) were then added and samples were incubated at room temperature for 3 hr in 25 mM Hepes, pH 7.4, 150 mM KCl, 10% glycerol (v/v). Samples were loaded onto 15% tris-glycine native gels and run at 80 V, 4°C for 6 hr. Gels were stained with Coomassie blue and imaged on a ChemiDoc MP Imaging System (Bio-Rad Laboratories, Hercules, California).

2.3 Results

2.3.1 Syntaxin-1 SNARE motif and MUN interactions

Previously it was shown that the MUN domain and SNARE motif of syntaxin-1 from 191-253 interact with weak affinity and this interaction is crucial for the promoting the formation of the SNARE complex from the syntaxin-1/Munc18-1 complex (Ma et al., 2011). To understand how the MUN domain/syntaxin-1 interactions enable SNARE opening I used NMR spectroscopy to study this interaction. The ^{1}H-^{15}N HSQC of ^{15}N-syntaxin-1 191-236 showed significant broadening in a subset of peaks in the presence of the MUN domain (Figure 2.1 A), suggesting that this truncated fragment of the SNARE motif is sufficient for the MUN/syntaxin-1 interaction. Identifying a minimal fragment for structural characterization is necessary to eliminate potential nonspecific interactions and increase peak dispersion in the NMR spectra.

From here I created single cysteine mutants of syntaxin-1 that can be tagged with DOTA-lanthanide complex using maleimide chemistry. Gadolinium is a frequently used lanthanide that

is highly paramagnetic due to its 7 unpaired electrons, enabling it to enhance T1 and T2 relaxation in nearby residues. This manifests as broadened resonances in the HSQC spectrum. Within 30 minutes of incubation with DOTA-Gd^{3+}, there was considerably broadening in the HSQC spectrum of ^{15}N-syntaxin-1 191-236 with a single cysteine (Figure 2.2), indicating that the protein is tagged. Since addition of a large, bulky tag like DOTA can interfere with protein interactions, I created five syntaxin-1 cysteine mutants and tested their ability to interact with the MUN domain when tagged and untagged. The ^{15}N-HSQCs of untagged S200C, S208C, I209C, and V223C syntaxin-1 mutants with the MUN domain showed binding comparable to wild-type syntaxin-1 (Figure 2.1 B-D,F), while the R210C mutation significantly weakens the interaction (Figure 2.1 E). In previous studies the R210E mutant syntaxin-1 was unable to interact with MUN (Ma et al., 2011), so the fact that the R210C mutation weakens the MUN domain interaction is not surprising.

At this point I tagged each of the syntaxin-1 mutants with DOTA-La^{3+} and tested if they could still interact with the MUN domain with the addition of the large, bulky tag. In these experiments I used the nonparamagnetic lanthanum to reduce tag-induced PREs and enable us to see broadening due to MUN domain interactions. The S200C, S208C, I209C, and V223C DOTA-La^{3+} tagged syntaxin-1 mutants were still able to interact with the MUN domain (Figure 2.1 B-D,F), making it possible to move forward and see if there is tag-induced broadening in the ^{1}H-^{13}C HMQC spectra of ^{2}H-$^{13}CH_3$-Ile, δ1-Leu, γ1-Val, Met-MUN domain. The ~70 kDa MUN domain is very large by traditional NMR standards and would have broad, poorly resolved peaks when labeled with ^{15}N, which is why we chose to increase sensitivity and resolution by specifically labeling the methyl groups of isoleucine, leucine, valine, and methionine with $^{13}CH_3$

in a deuterated background. Labeling specific residues reduces the total number of peaks and increases peak dispersion, while deuteration reduces proton-induced relaxation. I also used an approach that stereospecifically labels leucine and valine residues to reduce the leucine and valine peaks to half and increase the signal from the remaining peaks by two. All of this, coupled with the added sensitivity from ^{1}H-^{13}C HMQC spectra, makes it possible to observe NMR signals from the MUN domain (Figure 2.3).

The DOTA-Gd^{3+} tagged S200C and I209C syntaxin-1 191-236 were titrated into ^{2}H-$^{13}CH_3$-Ile, δ1-Leu, γ1-Val, Met-MUN and broadening in MUN domain resonances was monitored using HMQC spectra. Broadening was seen in a concentration-dependent manner in all MUN domain cross-peaks (Figure 2.4), which is a common feature of promiscuous interactions. It seems unlikely that this interaction is promiscuous though given the dramatic loss of binding and SNARE complex assembly from the R210E syntaxin-1 mutant. One of the benefits of PREs is that they enable study of weakly populated species, but it is likely that this benefit is detrimental in this particular context and the broadening throughout the entire MUN domain is coming from lowly populated, nonspecific binding events. To test if this nonspecific binding is coming from the DOTA tag, I used another DOTA-based tag called DC2 that was successfully applied to other systems in the lab (Brewer et al., 2015). The HMQC of labeled MUN domain in the presence of DC2-tagged I209C mutant syntaxin-1 shows specific broadening in a subset of resonances with some minor shifts that may arise from DC2 proximity (Figure 2.5A). It is likely that broadening is seen rather than PCSs because the interaction is dynamic and this averages out PCSs. Adding DC2 to the MUN domain in the presence of reducing agent results in a similar pattern of broadening and shifts (Figure 2.5B), indicating that

the DC2 interacts nonspecifically with the MUN domain and that this nonspecific interaction was producing the broadening.

2.3.2 MUN domain and SNARE complex interactions

A similar approach that was described in the previous section was used to evaluate the binding of the SNARE complex to the MUN domain. First, the SNARE complex made using the SNARE motifs of syntaxin-1, SNAP25, and synaptobrevin-2, known as the mini-core complex, was tagged with DC2 in the N- and C-terminal SNAP25 SNARE motifs (referred to as SN1 and SN3 respectively) and the interaction between MUN and the tagged complexes was evaluated. The D41C and D166C positions of SN1 and SN3 were selected because DC2 binds rigidly in these sites and gives strong PCSs within the SNARE complex, they are near the center of the SNARE complex, and they were successfully used in previous structural studies (Figure 2.6A)(Brewer et al., 2015). By monitoring the peak intensities of the first traces of HSQC spectra of ^{15}N-synaptobrevin mini core complex, I was able to assess binding of the MUN domain to SNARE complex. With untagged SNARE complex there is a significant drop in peak intensity when the MUN domain is added, indicating that there is an interaction similar to what was seen previously with soluble and membrane-anchored SNARE complexes (Figure 2.6 B,C) (Guan et al., 2008, Ma et al., 2011). The same experiment was performed with mini core complexes tagged with DC2 at position D41C in SN1 and D166C in SN3 and there was significant broadening induced by the MUN domain in both cases (Figure 2.6 D-G).

Since DC2-tagging does not impair MUN domain interactions, I monitored MUN domain resonances in the presence of DC2-tagged SNARE complex using ^{1}H-^{13}C HMQCs of ^{2}H-^{13}CH$_3$-Ile, δ1-Leu, γ1-Val, Met-MUN domain. The SN1-D41C and SN3-D166C tagged SNARE

complexes caused significant broadening in MUN domain resonances (Figure 2.7 A,C), suggesting there may be a specific, but dynamic, interaction. Removing the tag with reducing agent resulted in signal recovery in a number of peaks as well as broadening and shifts from nonspecific tag interactions similar to what was previously seen (Figure 2.7 B,D). While there was clearly some amount of specific binding, it is difficult to move forward with identifying the binding interface because there is binding coming from the SNARE complex and the DC2 tag itself.

2.3.3 C_2C domain and SNARE interactions.

While a lot is known about MUN domain and SNARE interactions, the contribution of adjacent domains to these interactions has not been characterized. Previously it was shown that the C_2C domain of Munc13 significantly enhances calcium-dependent lipid and content mixing (Liu et al., 2016), but it is not clear if a part of this stimulation comes from C_2C/SNARE or C_2C/SNARE complex interactions. Using ^{1}H-^{15}N HSCQs of various ^{15}N-SNAREs or SNARE complex in the presence of MUN and MUNC_2C I evaluated these interactions. Since we know that MUN interacts with the SNARE motif of syntaxin-1 from 191-236, I first tested if C_2C changes this interaction. While there is broadening in the presence of MUN and MUNC_2C (Figure 2.8), it is clear that the majority of the broadening is coming from the MUN domain and C_2C does not add anything additional to the interaction. The same was seen for the soluble cytoplasmic fragment of syntaxin-1 from 2-253 (Figure 2.9), the SNARE complex containing syntaxin-1 2-253 (Figure 2.10), and the cytoplasmic fragment of synaptobrevin-2 (Figure 2.11). While C_2C does not appear to change any of these binary interactions, it is possible that it is involved in a multicomponent interaction in the process of SNARE complex assembly. To test

this hypothesis, I performed native gel analysis of SNARE complex assembly in the presence of MUN, $MUNC_2C$, C_1C_2BMUN, and $C_1C_2BMUNC_2C$. In this assay I can monitor the efficiency of SNARE complex formation by comparing the total SNARE complex formed in various reaction conditions. While there is overlap between the MUN domain and fully formed SNARE complex on the gel that prevents analysis of this particular lane, we can see that the $MUNC_2C$, C_1C_2BMUN, and $C_1C_2BMUNC_2C$ fragments all enhance SNARE complex formation to a similar extent (Figure 2.12). If an analogous experiment were performed to monitor the formation of membrane anchored SNARE complex, it is likely that there would be enhancement from C_1, C_2B, and C_2C localizing the MUN domain to the membranes and increasing the local concentration near the syntaxin-1/Munc18 complex. This membrane localization and clustering from $C_1C_2BMUNC_2C$, as outlined in previous studies, is likely to underlie the enhancement in lipid mixing seen upon the addition of C_2C (Ma et al., 2013, Xu et al., 2017, Liu et al., 2016).

2.4 *Conclusions*

While the necessity of SNARE protein and SNARE complex binding to members of the core machinery is well established (Rizo, 2018), the underlying molecular mechanisms are not. Since Munc13-1 is directly involved in the formation of the SNARE complex, structural insights into the interactions between Munc13-1 and SNAREs or SNARE complex would provide valuable mechanistic insights into regulation of SNARE complex formation. The major difficulty in deriving structural constraints for these interactions comes from promiscuous binding or large motions in the bound state that hinder data analysis. In order to overcome these issues, one could continue building up the system so it has more components that weakly interact to stabilize a specific bound conformation, similar to what was done when analyzing the differences between

MUN and $MUNC_2C$ interactions with SNAREs or SNARE complexes. Adding more members of the machinery would be useful, but it is possible that the system gets too large for NMR analysis. In addition, synaptobrevin-2 and syntaxin-1 are membrane-anchored proteins and membranes may play a role in these interactions. To overcome these potential problems one could use another technique such as crosslinking coupled with mass spectrometry. This technique makes it possible to analyze all of the possible binding regions between two proteins that have interacting residues capable of being crosslinked. Using a variety of crosslinkers, it is possible to derive restraints that provide structural insights into multicomponent interactions (Leitner et al., 2016).

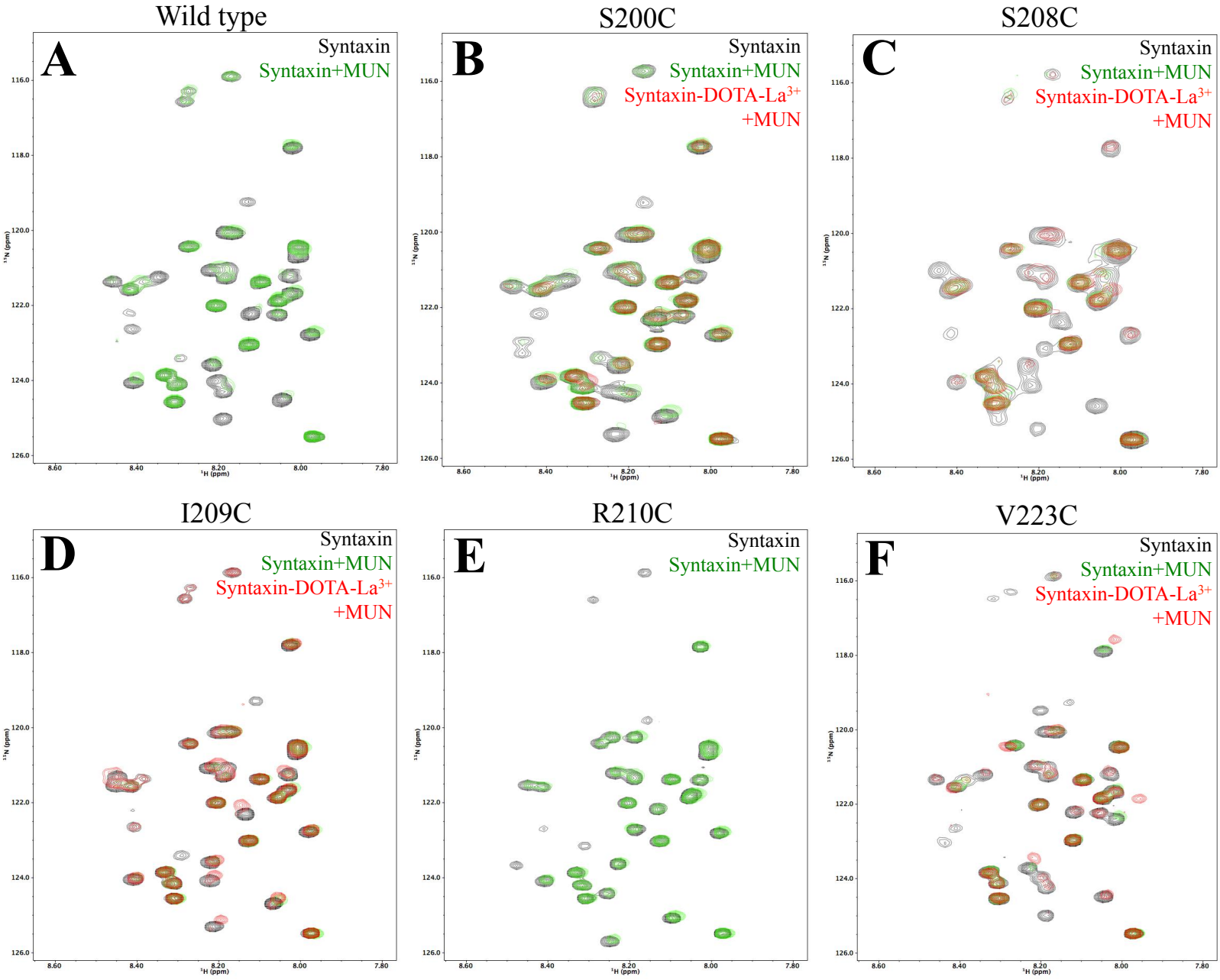

Figure 2.1 NMR analysis of the interaction between Syntaxin 191-236 wild-type and DOTA-Gd^{3+} tagged cysteine mutants with the MUN domain

Overlays of ^{1}H-^{15}N HSQC spectra of ^{15}N-syntaxin 191-236 wild type or mutants (30 μM) in the presence (green spectra) or absence (black spectra) of 30 μM MUN domain. The wild type and all mutants except the R210C show broadening due to interactions with the MUN domain. The interaction between syntaxin and MUN is maintained even when the cysteine is labeled with DOTA-La^{3+} (red spectra).

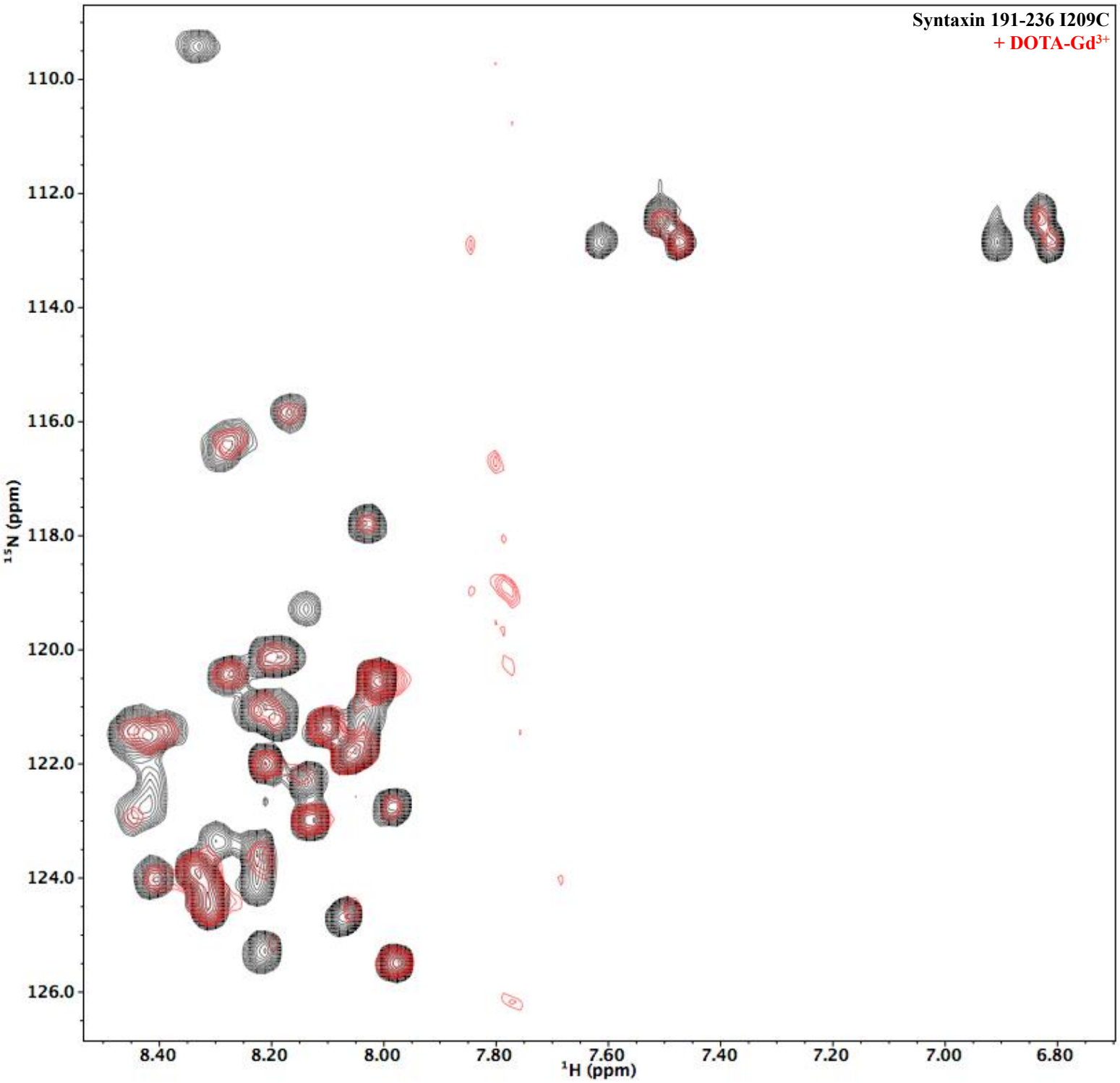

Figure 2.2 Syntaxin 191-236 I209C can be tagged with DOTA-Gd^{3+}
^{1}H-^{15}N HSQC spectra of 65 µM Syntaxin 191-236 collected at 600 mHz.. Addition of 5 mM DOTA-Gd^{3+} results in broadening within a subset of residues, likely near the tag site, within 30 minutes. No increase in broadening was seen with longer incubation times.

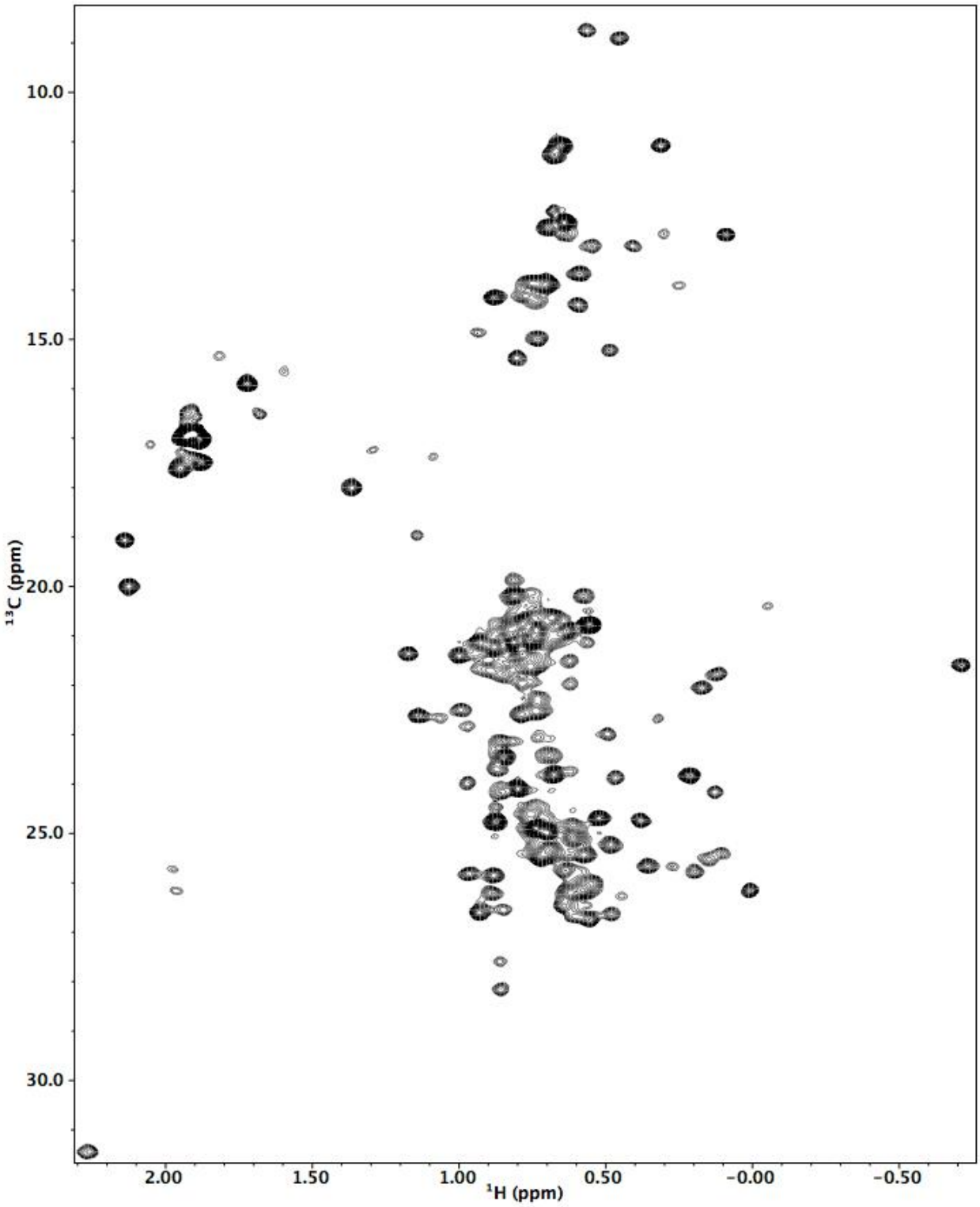

Figure 2.3 ^{1}H-^{13}C HMQC spectrum of the 70 kDa MUN domain
^{1}H-^{13}C HMQC spectrum of 20 μM ^{2}H-$^{13}CH_3$-Ile, δ1-Leu, γ1-Val, Met- MUN 859-1516ΔEF collected at 600 mHz for 6.6 hours.

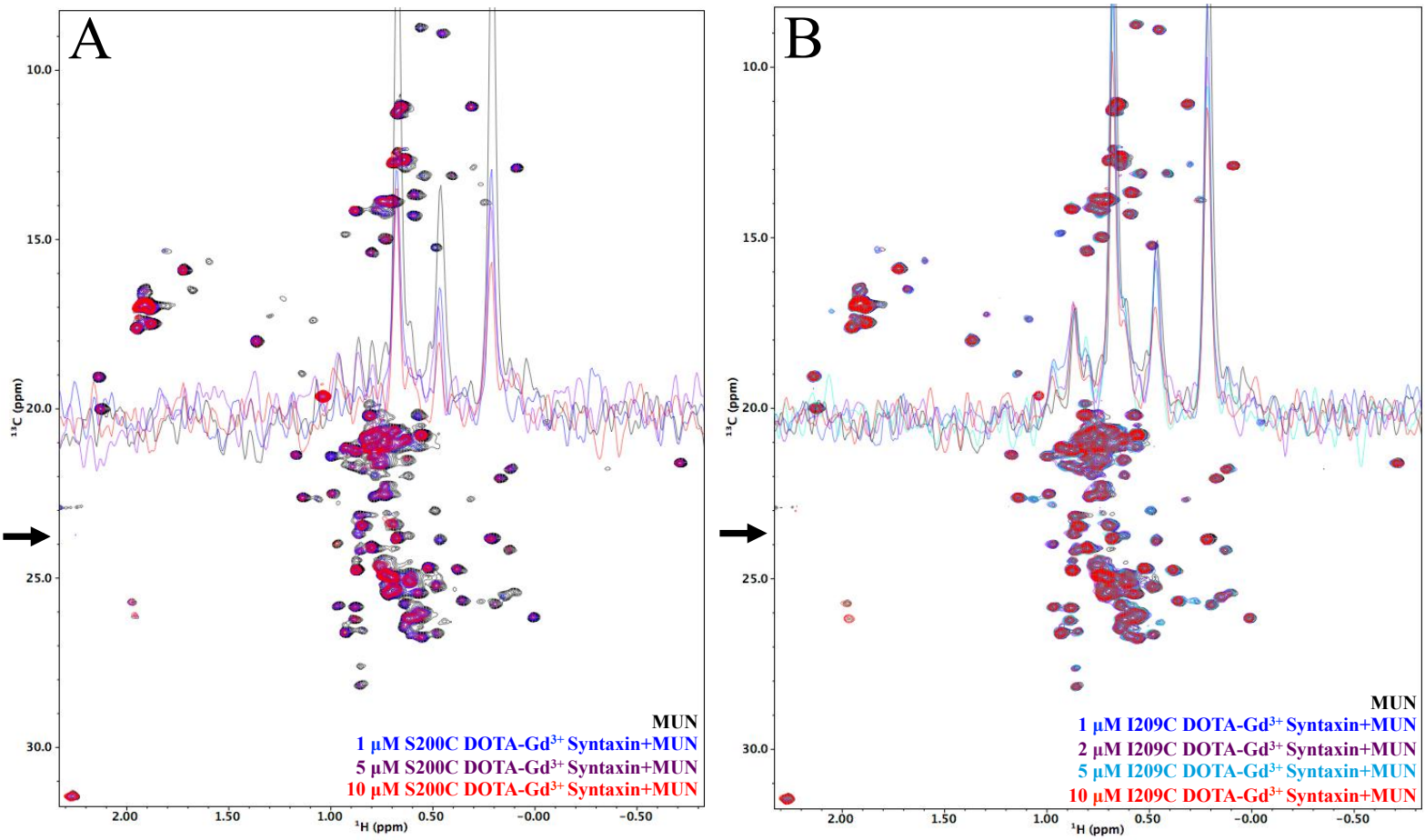

Figure 2.4 DOTA-Gd^{3+} tagged syntaxin 191-236 constructs induce nonspecific broadening in MUN domain resonances

Overlays of ^{1}H-^{13}C HMQC spectra of 20 µM ^{2}H-^{13}CH$_3$-Ile, δ1-Leu, γ1-Val, Met- MUN 859-1516ΔEF (black spectra) with increasing quantities of S200C DOTA-Gd^{3+} syntaxin 191-236 (A) or I209C DOTA Gd^{3+} syntaxin 191-236 (B). One-dimensional traces were generated from the ^{13}C slice marked with a black arrow and show broadening in all peaks in a concentration-dependent manner.

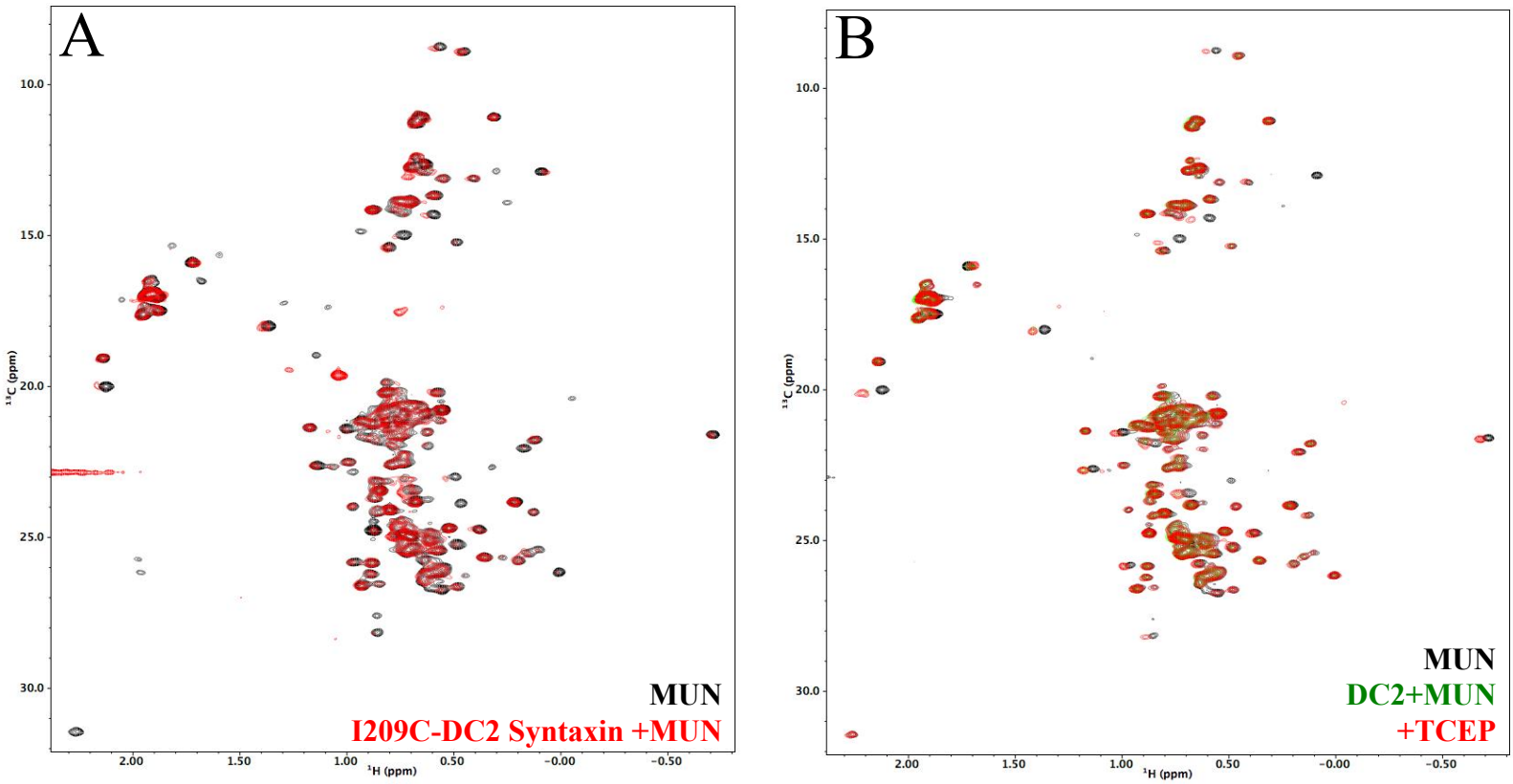

Figure 2.5 DC2 tagged syntaxin 191-236 induces broadening and minor pseudocontact shifts in MUN domain resonances

Overlays of ^{1}H-^{13}C HMQC spectra of 20 μM ^{2}H-^{13}CH$_3$-Ile, δ1-Leu, γ1-Val, Met- MUN 859-1516ΔEF (black spectra) with 20 μM DC2-tagged syntaxin 191-236 I209C (A, red spectrum) or in the presence of DC2 alone (B, green spectrum). Similar shifts and broadening were seen in both conditions, suggesting that the changes in the MUN domain spectra are from tag alone. Addition of reducing agent (B, red spectrum) results in no changes, so the shifts and broadening are from nonspecific interactions between MUN and DC2.

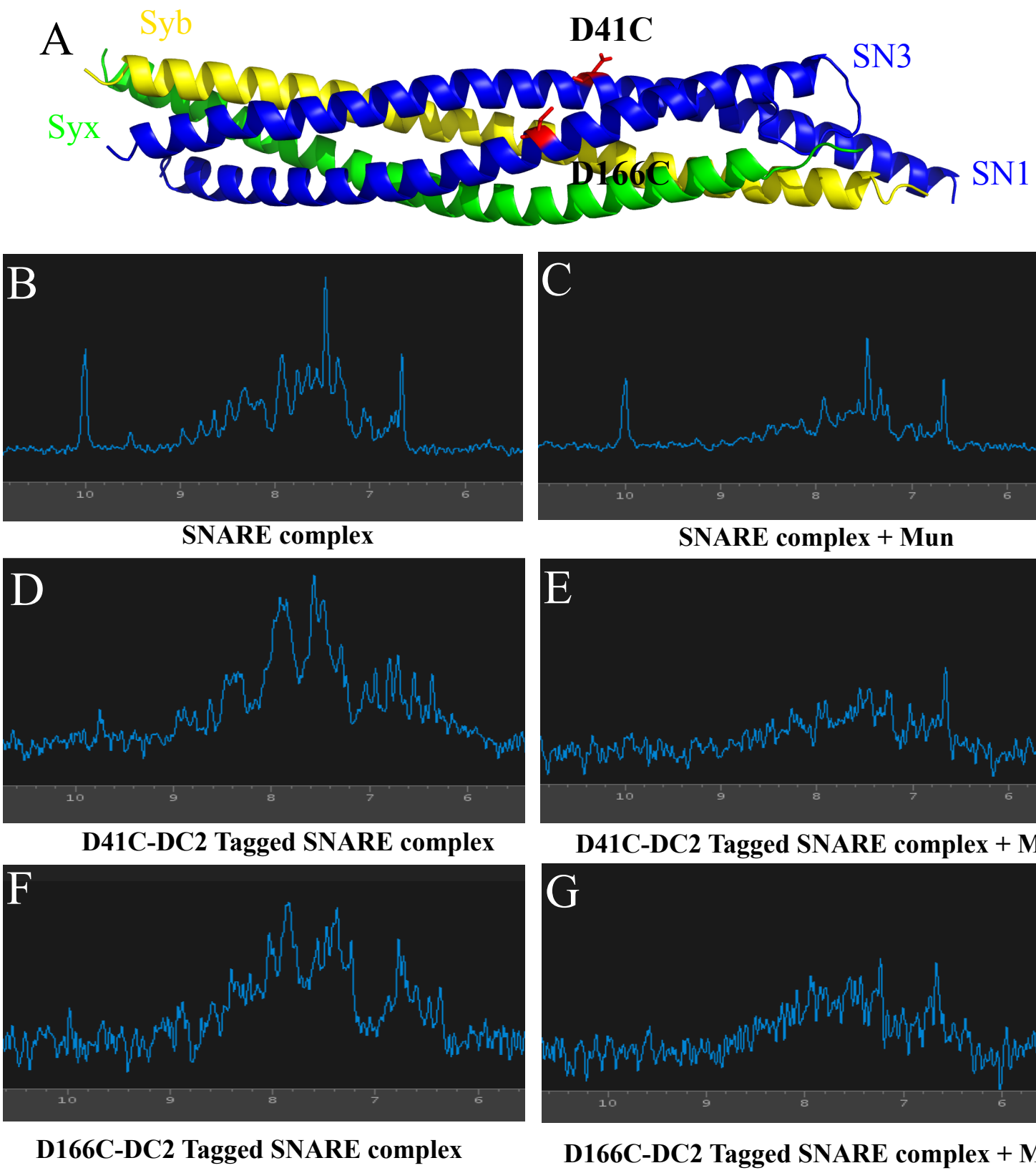

Figure 2.6 DC2 tag locations on the SNARE complex and NMR analysis of the interaction between wild-type and DC2-tagged SNARE complex and the MUN domain

(A) Ribbon diagram of the neuronal SNARE complex (PDB ID 1SFC) with mutated residues for DC2 tagging as red sticks. Comparisons of peak intensity from ^{1}H-^{15}N TROSY-HSQCs of 30 μM ^{15}N-synaptobrevin incorporated SNARE complex wild type (B), D41C-DC2 (D), or D166C-DC2 (F) alone or in the presence of 30 μM MUN domain (C,E,G). SNARE complex signal decreases upon MUN domain binding, indicating that there is an interaction even when the SNARE complex is tagged with DC2.

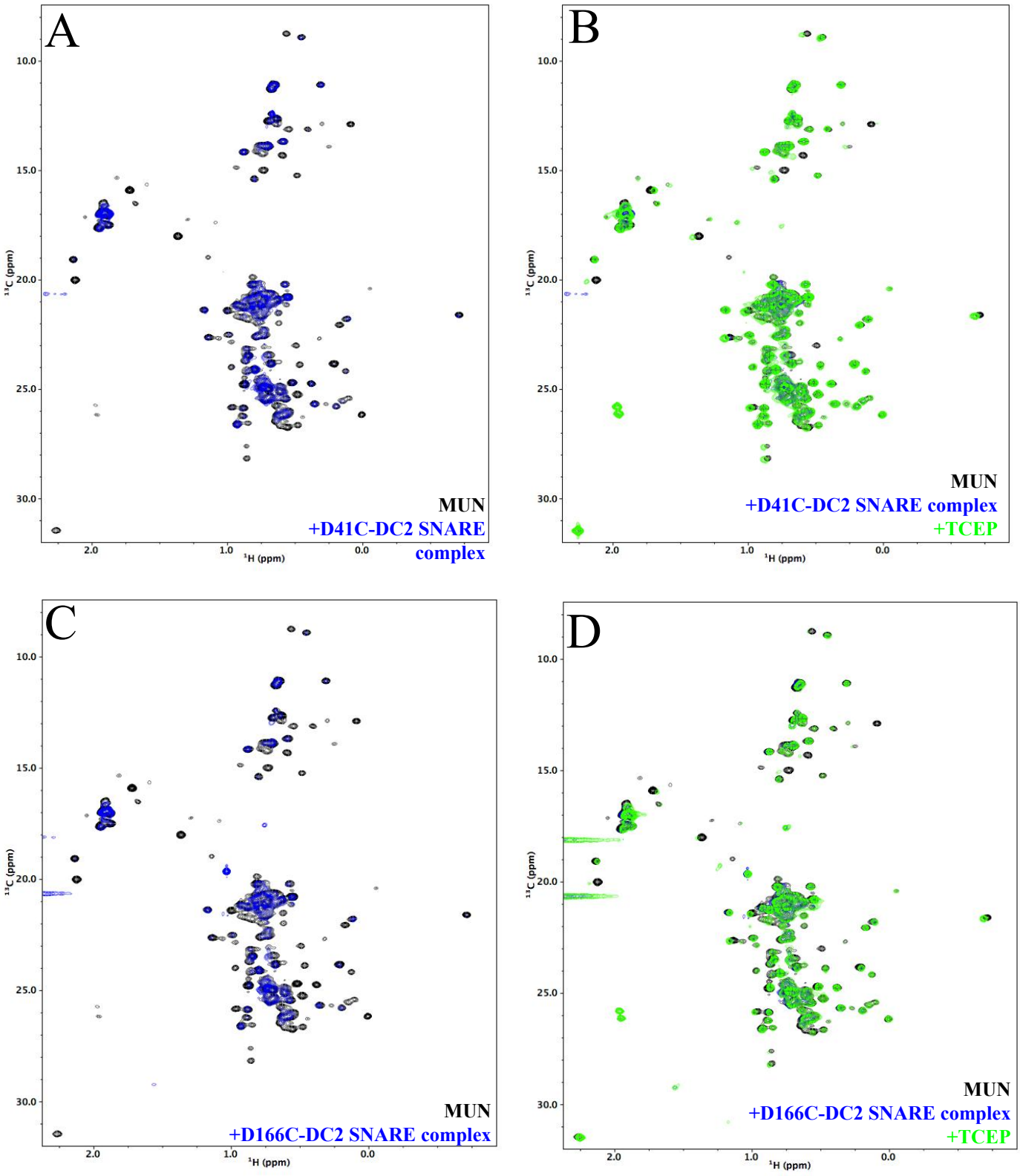

Figure 2.7 DC2 tagged SNARE complex induces specific broadening in MUN domain resonances
Overlays of ^{1}H-^{13}C HMQC spectra of 20 μM ^{2}H-$^{13}CH_3$-Ile, δ1-Leu, γ1-Val, Met- MUN 859-1516ΔEF (black spectra) with 20 μM D41C-DC2 SNARE complex (A, blue spectrum) or 20 uM D166C-DC2 SNARE complex (C, blue spectrum). Both induce broadening and minor shifts in MUN domain resonances, indicating an interaction. Removing the DC2 tag by introducing reducing agent (B,D) results in shifts and broadening due to the nonspecific interaction between the DC2 tag and MUN.

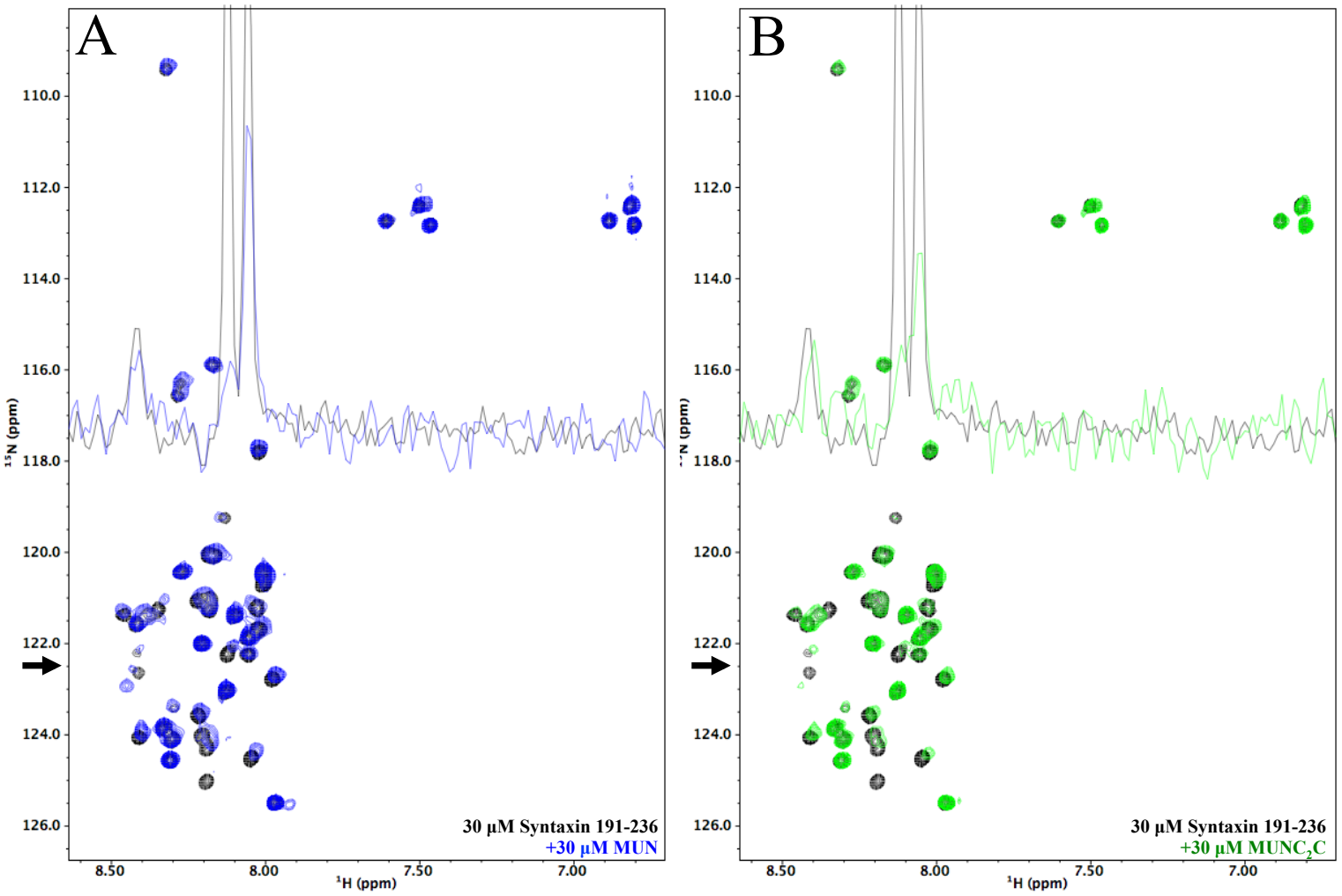

Figure 2.8 The C_2C domain does not enhance interactions with syntaxin-1 191-236
Overlays of ^{1}H-^{15}N HSQC spectra of ^{15}N-syntaxin-1 191-236 (black spectra) with MUN (A, blue spectra) or $MUNC_2C$ (B, green spectra). Bold arrows indicate the ^{15}N slice used for one dimensional analysis. The C_2C domain of Munc13 doesn't appear to enhance binding to this fragment

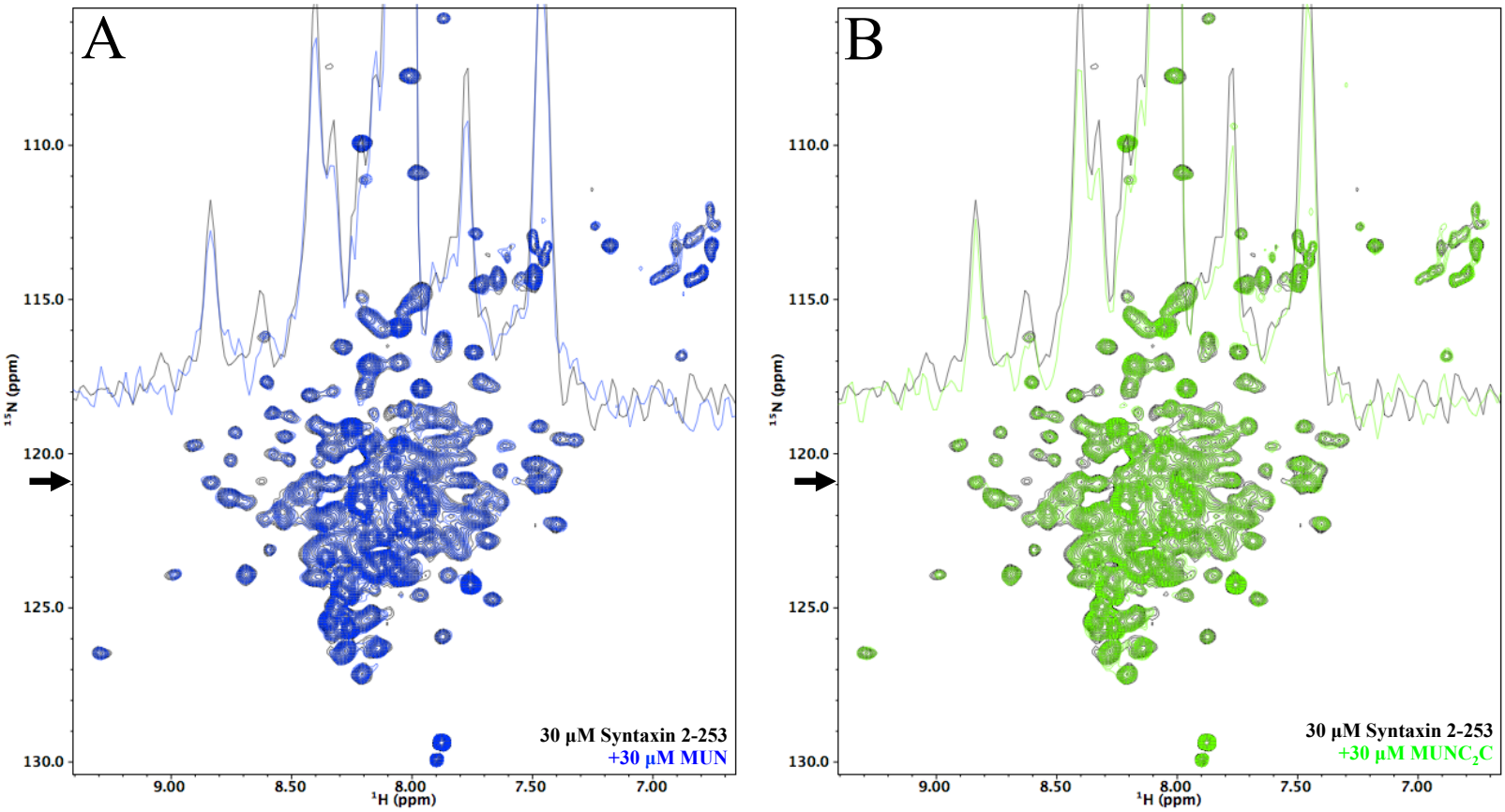

Figure 2.9 The C_2C domain does not enhance interactions with syntaxin-1 2-253
Overlays of ^{1}H-^{15}N HSQC spectra of ^{15}N-syntaxin-1 2-253 (black spectra) with MUN (A, blue spectra) or $MUNC_2C$ (B, green spectra). Bold arrows indicate the ^{15}N slice used for one dimensional analysis. The C_2C domain of Munc13 doesn't appear to enhance binding to this fragment

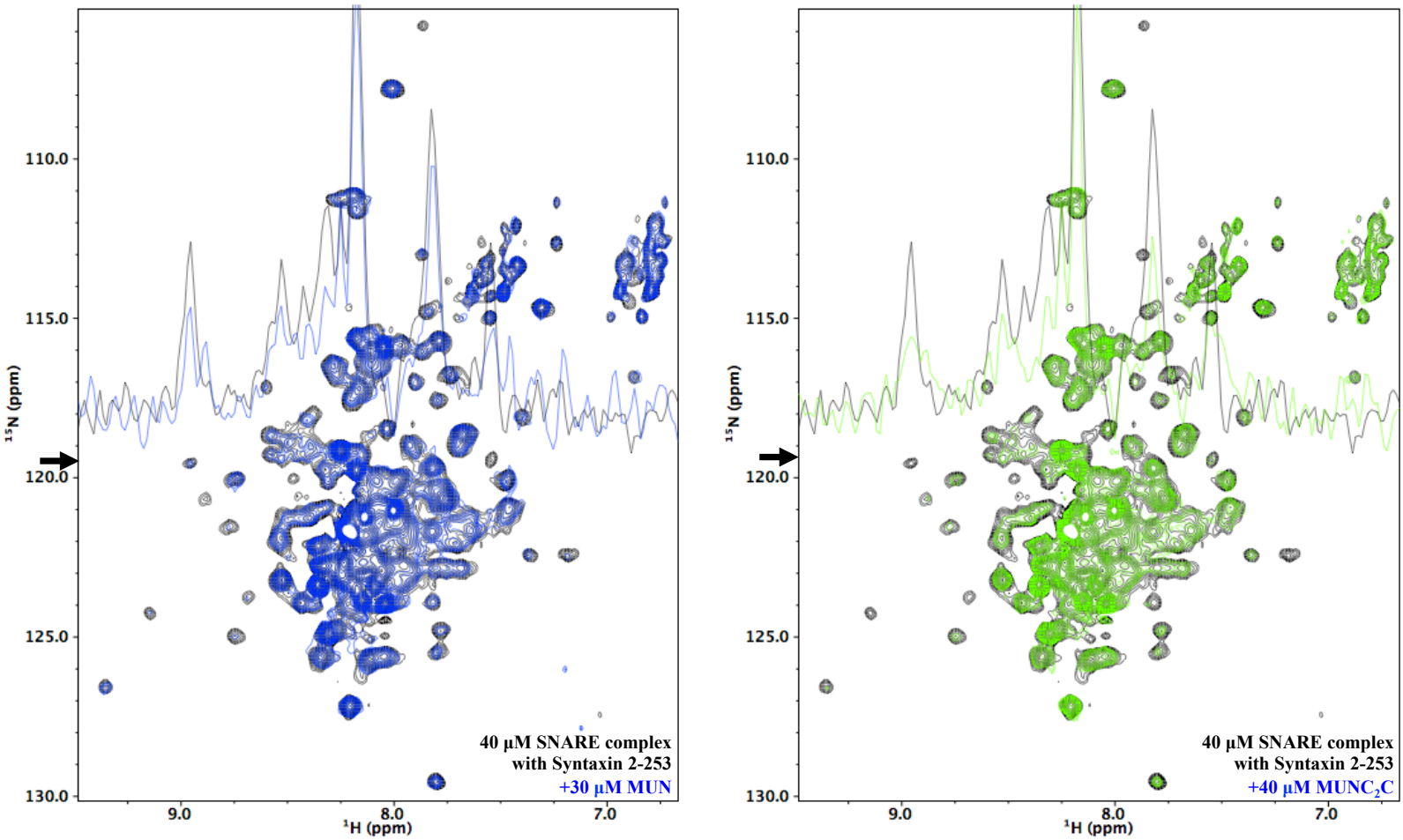

Figure 2.10 The C_2C domain does not enhance interactions with SNARE complex containing syntaxin 2-253
Overlays of ^{1}H-^{15}N HSQC spectra of SNARE complex containing ^{15}N-syntaxin-1 2-253 (black spectra) with MUN (A, blue spectra) or $MUNC_2C$ (B, green spectra). Bold arrows indicate the ^{15}N slice used for one dimensional analysis. The C_2C domain of Munc13 doesn't appear to enhance binding to this fragment

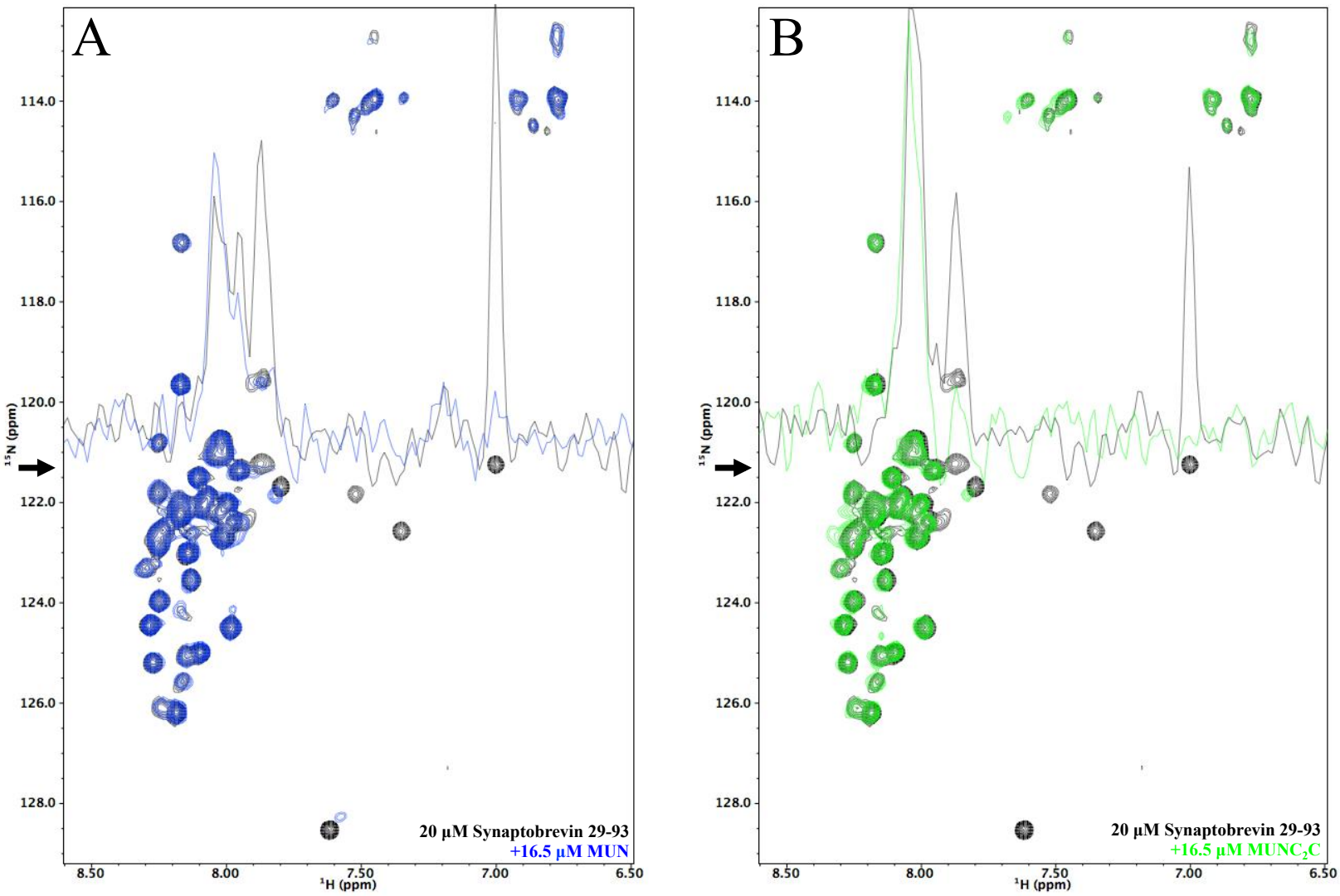

Figure 2.11 The C_2C domain does not enhance interactions with synaptobrevin-2 29-93
Overlays of ^{1}H-^{15}N HSQC spectra of ^{15}N-synaptobrevin-2 29-93 (black spectra) with MUN (A, blue spectra) or MUNC_2C (B, green spectra). Bold arrows indicate the ^{15}N slice used for one dimensional analysis. The C_2C domain of Munc13 doesn't appear to enhance binding to this fragment

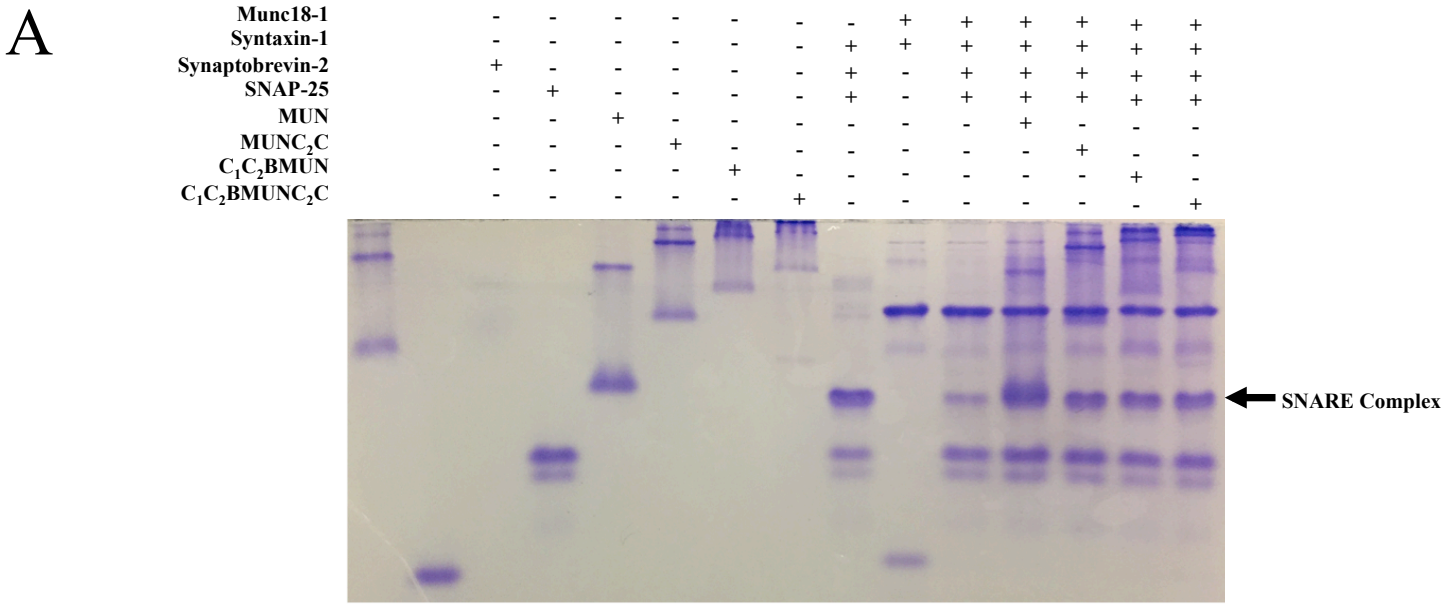

Figure 2.12 Native gel analysis of SNARE complex formation starting from Munc18-1/syntaxin-1 complex
Native gel analysis of the ability of various Munc13 fragments to stimulate SNARE complex formation starting with Munc18/syntaxin complex. C_2C doesn't enhance soluble SNARE complex formation.

CHAPTER 3-Structural characterization of the C2C domain of Munc13

3.1 Introduction

The presynaptic fusion machinery is made up of a key set of components including syntaxin-1, SNAP25, synaptobrevin-2, Munc18-1, Munc13-1, NSF, α-SNAP, and synaptotagmin-1 (Rizo, 2018). The SNARE proteins are the heart of the fusion machinery and are conserved throughout intracellular fusion systems. The other components are key drivers of fusion that also provide an additional layer of regulation that underlies the specificity of interneuronal communication. Munc13-1 plays a pivotal role in this process by regulating the formation of the SNARE complex to dictate when priming occurs and it has also been implicated in bridging the synaptic vesicle and plasma membrane (Richmond et al., 2001, Liu et al., 2016). Structural characterization of the various domains of Munc13-1 has provided key insights in how these domains function to enable Munc13-1 to regulate fusion.

At this point structures have been solved for four of the five domains of Munc13-1. The C_2A domain structure showed that it formed a stable homodimer and enabled the development of mutants that break the homodimer (Lu et al., 2006). From this it became clear that when C_2A homodimerizes it inhibits the activity of Munc13-1 and that binding of the RIM2α zinc finger activates Munc13-1 by breaking the C_2A homodimerization (Deng et al., 2011). The NMR structure of the C_1 domain showed that it was a standard C_1 domain, but the tryptophan that serves as the binding site for DAG is buried in between two loops rather than exposed to solvent like in PKCs C_1 domains, suggesting a possible mechanism for regulating DAG binding (Shen et al., 2005). The crystal structure of the C_2B domain showed that it was a standard β-sandwich structure with a unique helix in the membrane binding loops. This helix has a large number of

solvent exposed positive charges, explaining the biochemical data that C_2B can bind to membranes independent of calcium. It also enabled the creation of mutants that helped explain the role that C_2B plays in synaptic plasticity (Shin et al., 2010). The structures of the MUN domain and the C-terminal half of the MUN domain conclusively proved its structural homology to other tethering factors and made it possible to screen for highly conserved, solvent exposed residues that allow the MUN domain to catalyze the opening of syntaxin-1 (Yang et al., 2015, Li et al., 2011). The recent structure of C_1C_2BMUN showed that it forms a relatively rigid structure with defined orientations between its membrane binding domains, suggesting that there may be multiple ways for Munc13-1 to bind membranes (Xu et al., 2017). The C_2C domain of Munc13 is critical for Munc13 function (Liu et al., 2016), but has not been characterized biochemically or structurally. Structural characterization of this domain would make it possible to study the key role that C_2C has in Munc13 function.

3.2 Methods

3.2.1 Recombinant Protein Expression and Purification

All recombinant Munc13 fragments were prepared using standard molecular biology techniques from the *Rattus norvegicus* Munc13-1 and have a disordered loop from 1408-1452 removed. A flexible loop from 1040-1053, referred to as the AB loop, was also removed in some constructs to aid in crystallization. The various constructs of C_2C alone were prepared as GST-fusions in pGEX vector or as an N-terminal MBP-fusion with a C-terminal hexahistidine tag in pMBP vector. The various constructs containing $MUNC_2C$ and $MUNCDC_2C$ were prepared as N-terminal GST-fusion proteins in pGEX vector. Constructs containing $C_1C_2BMUNC_2C$ were

prepared with an N-terminal hexahistidine tag in pET28a vector. A full list of constructs can be found in table I and II.

All GST-C_2C constructs were transformed into BL21 (DE3) *E. coli* and grown in ampicillin containing LB media until induction at an OD_{600} of ~0.8. Induction was tested at a range of IPTG concentrations from 0.1 to 1.0 mM, temperatures of 16°C, 24°C, or 37°C, and induction times ranging from 3 hours to overnight. Expression with 0.5 mM IPTG overnight at 16°C was optimal. After expression was complete the cells were harvested by centrifugation, resuspended in cold PBS with 1 mM DTT, and lysed. Cell lysate was spun at 48,000 x g for 30 minutes to clarify the lysate and then incubated with Glutathione Sepharose 4B resin (GE), amylose resin (New England Biolabs), or Ni-NTA resin (Thermo Fisher Scientific) for 1 hour at room temperature or overnight at 4°C. For GST-fusion and MBP-fusion constructs the resin-bound protein was washed with PBS, PBS with 1M NaCl, and thrombin cleaveage buffer. Thrombin cleavage was performed overnight at 4°C. Attempts were made to elute cleaved protein using high salt and detergents. Hexahistidine tagged proteins were washed with PBS and PBS with 1 M NaCl prior to elution with 500 mM imidazole.

All MUNC_2C and MUNCDC_2C constructs were transformed into BL21 (DE3) *E. coli* and grown in ampicillin containing LB media until induction at an OD_{600} of ~0.8. Induction was performed overnight at 16°C with 0.5 mM IPTG. After expression the cells were harvested by centrifugation, resuspended in cold PBS with 1 mM DTT, and lysed. Cell lysate was spun at 48,000 x g for 30 minutes to clarify the lysate and then incubated with Glutathione Sepharose 4B resin (GE) at room temperature for 1 hour or overnight at 4°C. Bound protein was washed using PBS and PBS with 1 M NaCl. To eliminate any bound DNA, nuclease treatment was performed

on the beads for 1 hour at room temperature with 250 U of Pierce Universal Nuclease (Thermo Fisher Scientific) per liter of culture. Resin-bound protein was washed again with PBS, PBS with 1 M NaCl, and 50 mM Tris, pH 8, 250 mM NaCl, 1 mM TCEP, 2.5 mM $CaCl_2$, 10% glycerol (v/v). Thrombin cleavage was performed overnight at 4°C and protein was eluted the following day by washing with thrombin cleavage buffer. Eluted protein was diluted twentyfold and subjected to anion exchange chromatography using a HiTrapQ HP column (GE Life Sciences). Protein was eluted in 20 mM Tris, pH 8, 1 mM TCEP, 10% glycerol (v/v) with a linear gradient from 1% to 50% of 1 M NaCl. The protein was concentrated at room temperature and subjected to gel filtration in an Superdex 200 16/60 column (GE Life Sciences). $MUNC_2C$ was eluted using 20 mM Tris, pH 8, 250 mM NaCl, 1 mM TCEP, 10% glycerol. $MUNCDC_2C$ was eluted using 20 mM Tris, pH 8.5, 250 mM NaCl, 1 mM TCEP, 10% glycerol (v/v). After gel filtration the protein was concentrated at room temperature. If aggregation was observed doing concentration the protein was heated at 42°C in a water bath until the aggregation disappeared.

All $C_1C_2BMUNC_2C$ constructs were transformed into BL21 (DE3) *E. coli* and grown in kanamycin containing LB media until induction at an OD_{600} of ~0.8. Induction was performed overnight at 16°C with 0.5 mM IPTG. After expression the cells were harvested by centrifugation, resuspended in 20 mM Tris, pH 8, 250 mM NaCl, 1 mM TCEP, 10% glycerol (v/v), and lysed. Cell lysate was spun at 48,000 x g for 30 minutes to clarify the lysate and then incubated with Ni-NTA resin at room temperature for 30 minutes. Bound protein was washed using resuspension buffer with 1 M NaCl to remove contaminants. To eliminate any bound DNA, nuclease treatment was performed on the beads for 1 hour at room temperature with 250 U of Pierce Universal Nuclease (Thermo Fisher Scientific) per liter of culture. Protein was eluted

from the column using resuspension buffer with 500 mM imidazole and dialyzed against 50 mM Tris, pH 8, 250 mM NaCl, 1 mM TCEP, 2.5 mM $CaCl_2$, 10% glycerol (v/v) overnight at 4°C in the presence of thrombin. The solution was re-applied to Ni-NTA resin to remove any uncleaved protein and diluted twentyfold in 20 mM Tris, pH 8, 1 mM TCEP, 10% glycerol (v/v). Diluted protein was subjected to anion exchange chromatography using a HiTrapQ HP column (GE Life Sciences) and eluted in 20 mM Tris, pH 8, 1 mM TCEP, 10% glycerol (v/v) with a linear gradient from 1% to 50% of 1 M NaCl. If necessary, the protein was concentrated and subjected to gel filtration chromatography on a Superdex 200 16/60 column (GE Life Sciences) and eluted in 20 mM Tris, pH 8, 250 mM NaCl, 1 mM TCEP, 10% glycerol (v/v). If aggregation was observed doing concentration the protein was heated at 42°C in a water bath until the aggregation disappeared.

3.2.2 Crystallization of Recombinant Munc13 Fragments and X-ray Data Collection

Initial sparse matrix crystallization screening was performed in 96-well sitting drop plates using an Art Robbins Crystal Phoenix and various commercial crystallization kits including Pact premier (Molecular Dimensions), ProPlex (Molecular Dimensions), PEG/Ion (Hampton Research), SaltRx (Hampton Research), The ComPAS Suite (Qiagen), Index (Hampton Research), PEGRx (Hamptom Research), Clear Strategy (Hamptom Research), JCSG+ (Molecular Dimensions), and Structure Screen 1 + 2 (Molecular Dimensions). Screens were checked daily for one month to monitor crystal growth. Conditions with large, single, birefringent crystals were optimized by grid screening pH, precipitant concentration, and additives in hanging drop vapor diffusion plates. Large, birefringent, single crystals were cryoprotected prior to X-ray data collection to decrease radiation damage. Cryoprotected crystals

were mounted in a Rigaku R-Axis IV x-ray detector and diffraction was measured or they were sent to APS Beamline 19-ID at the Advanced Photo Source (Argonne National Laboratory, Argonne, IL) for diffraction.

3.2.3 Negative stain electron microscopy

Purified $C_1C_2BMUNC_2C$ was diluted to 0.01 mg/ml and 3 µl was applied to negatively glow discharged carbon square 200 mesh grids (Electron Microscopy Sciences). After 30 seconds the protein was blotted off and the grid was briefly washed with 3 µl of 1% uranyl acetate. After the wash step, 3 µl of 1% uranyl acetate was added again and the grid was incubated for 30 seconds before all liquid was blotted away. After a brief drying period the grids were imaged on a Technai Spirit G2 BioTWIN Transmission Electron Microscope (FEI).

3.2.4 Cryo-electron microscopy

Purified $C_1C_2BMUNC_2C$ was dialyzed overnight in 25 mM Hepes, pH 7.4, 150 mM KCl, 1 mM TCEP to remove glycerol. Protein stocks were diluted to a concentration of 0.2 mg/ml and in certain samples Nonidet P-40 and Tween-20 were added at 0.05% and 0.075% respectively. A total of 3 µl was applied to negatively glow discharged Quantifoil 200 mesh gold grids and blotted in a humidity-controlled Vitrobot Mark IV with a blot force of 18 and a blot time of 5 seconds. Samples were imaged on an FEI Talos Arctica with a K2 direct electron detector.

3.3 Results

3.3.1 Crystallographic studies of the C2C domain of Munc13-1

At this moment there is a wealth of structural data for various fragments of Munc13 (Shen et al., 2005, Shin et al., 2010, Lu et al., 2006, Yang et al., 2015, Xu et al., 2017, Li et al., 2011), but little is known about the C-terminal C_2 domain known as C_2C. Based on the protein

sequence it is expected to have the standard C_2 domain fold consisting of eight β-strands folding into a β-sandwich and it lacks the aspartic acid residues that typically coordinate calcium in other calcium-binding C_2 domains (Nalefski and Falke, 1996). While this information, along with the available structures of various C_2 domains, makes it possible to get structural insights from homology modeling, an experimentally derived structure may have some unexpected features that provide fundamental insights into how the domain functions. Both the C_2A and C_2B domains of Munc13 appeared to have standard C_2 topology like C_2C, but C_2A contains an additional β-hairpin loop that aids in homodimerization and C_2B contains an additional charged helix that promotes calcium-independent membrane binding (Lu et al., 2006, Shin et al., 2010)

Attempts to express a soluble fragment of C_2C alone were met with failure as all constructs failed to elute from affinity columns (Figure 3.1A). Varying the N- and C-terminus, changing affinity tags, and changing the expression system did not help with solubility (Table 1), leading us to believe that C_2C requires the adjacent MUN domain for stability. This was validated by creating a construct of MUNC_2C with a TEV cleavage site in between the MUN and C_2C domains. After cleavage with TEV, gel filtration was run on the mixture and the small amount of cleaved, soluble C_2C coeluted with the main MUN domain peak (Figure 3.1B). It is possible that C_2C requires the MUN domain because they form a stable structure similar to what was seen with C_1 and C_2B in the C_1C_2BMUN structure (Xu et al., 2017).

Since the structure of the C-terminal half of the MUN domain, called MUN-CD, was previously solved, it seemed obvious to see if constructs of MUNCDC_2C are stable (Li et al., 2011). MUNCDC_2C constructs expressed quite well, but had low solubility (Table II). The solubility issues were overcome by using higher concentrations of sodium chloride, typically

around 250 mM, and purifying the protein at room temperature. If large amounts of precipitation were observed the protein was heated briefly at 42°C until aggregation disappeared. Using these optimizations I was able to produce large quantities of pure, homogenous MUNCDC$_2$C (Figure 3.2 A). It readily crystallized in a variety of conditions and optimization yielded a large, rod-like crystal form and a cubic crystal form (Figure 3.2 B,D). The crystals were typically fragile and were difficult to retrieve from the drop for cryoprotection. The diffraction of both crystal forms was tested and very few diffraction spots were observed (Figure 3.2 C,E). The lack of diffraction, coupled with the fragility of the crystals, suggests that the protein was not packing well into crystals.

In an attempt to form better crystals, the construct was extended to include the entire MUN domain and C$_2$C. Attempts to crystallize the full MUNC$_2$C construct yielded no crystals, likely due to some flexibility in the MUN domain that hinders crystal packing. Disorder predictions suggest that there is a small, disordered loop in the AB domain of MUN that may be reducing crystallizability, so the loop was removed and replaced with glycine-serine-glycine. Removing the loop, referred to as the AB loop, increased the expression, homogeneity, and solubility of the MUN domain alone (Figure 3.3A,B), so this loop was removed from MUNC$_2$C. In another construct the N-terminal portion of the MUN domain was truncated at residue 933 to match the structure of the MUN domain that was previously solved (Yang et al., 2015). The MUNC$_2$CΔABΔEF from 859-1735 and MUNC2CΔEF from 933-1735 readily crystallized (Figure 3.3 C,E), with the MUNC$_2$CΔABΔEF construct yielding larger, single crystals. Optimizing crystal growth and cryoprotection yielded diffraction to ~7 Å under ideal conditions (Figure 3.3 D). Finally, I attempted to crystallize the full C$_1$C$_2$BMUNC$_2$CΔEF from 529-1735.

While it readily crystallized (Figure 3.3 F), it was plagued with poor crystal growth and weak diffraction (data not shown).

3.3.2 Electron microscopy analysis of $C_1C_2BMUNC_2C$

Due to the recent advances in cryo-electron microscopy, it was an obvious technique to try and solve the structure of $C_1C_2BMUNC_2C$. To monitor particle homogeneity and dispersion I performed negative stain transmission electron microscopy. From the images collected it is clear that there is some minor aggregation (Figure 3.4 A), but in general there are clear particles that match what we expect from the C_1C_2BMUN structure (Figure 3.4 B,C)(Xu et al., 2017). From here I froze samples of $C_1C_2BMUNC_2C$ and visualized them using cryo-electron microscopy, but there were very few particles that matched the expected shape from the crystal structure (Data not shown). It appeared that the $C_1C_2BMUNC_2C$ fragment was breaking during blotting, likely from interacting with the water-air interface. To prevent this, grids were prepared with a low concentration of detergent (0.075% Tween-20 or 0.05% Nonidet P-40) and imaged. Particles of $C_1C_2BMUNC_2C$ were much more stable, but the concentration observed on the grid was very low. The protein also appeared to have an orientation preference with very few particles being observed in certain dimensions. In order to solve the structure of $C_1C_2BMUNC_2C$ by cryo-electron microscopy one would need to solve the orientation preference issue and increase the concentration on the grids containing detergent. The orientation preference issue could potentially be resolved by raising antibodies against $C_1C_2BMUNC_2C$ and making stable $C_1C_2BMUNC_2C$/Fab complex. This may also help with the problems that arise from blotting.

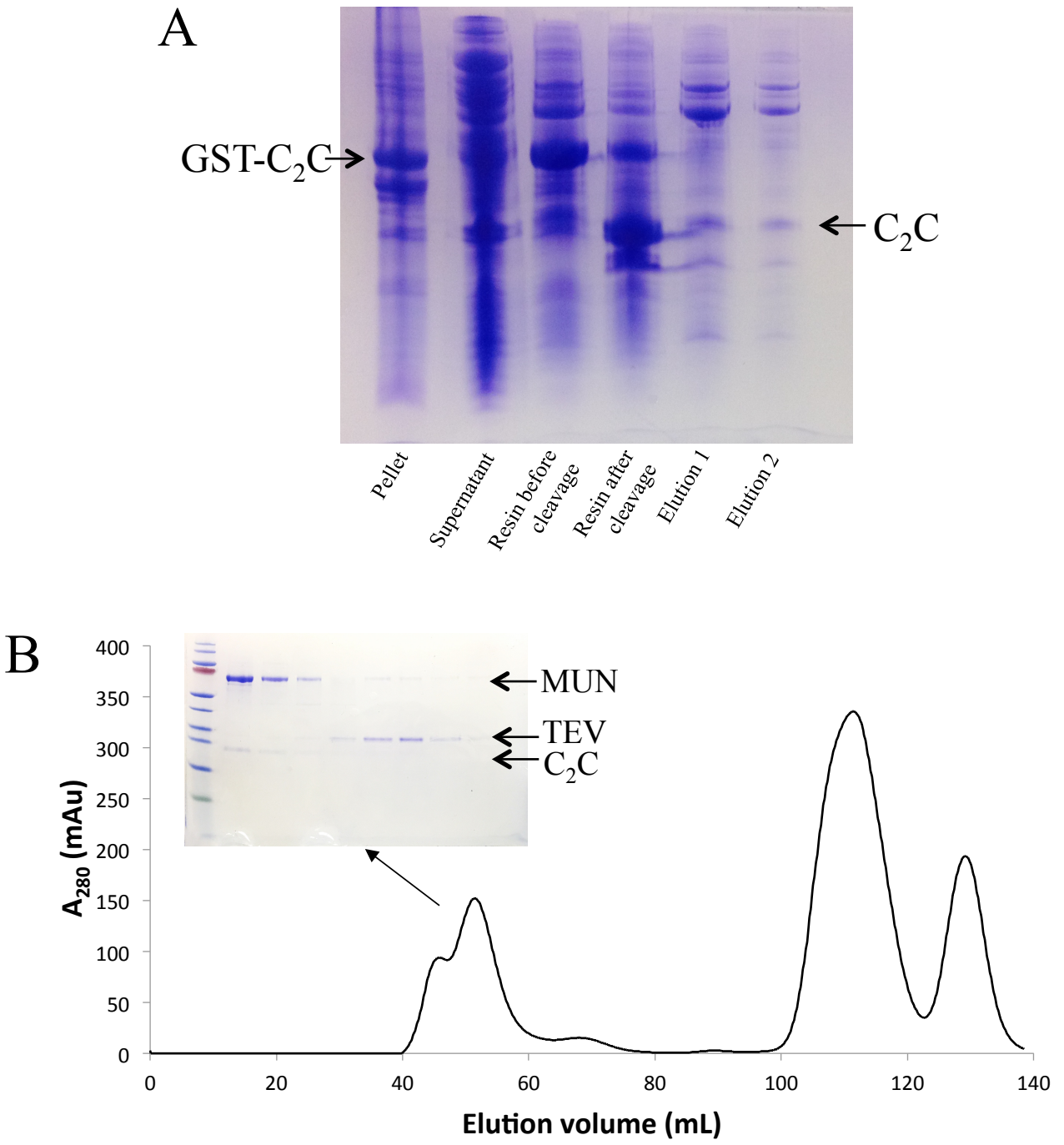

Figure 3.1 Munc13-1 C_2C alone is insoluble and coelutes with the MUN domain when separated with TEV
(A) Example affinity purification of C_2C fragments, indicating that they aggregate on the beads after cleavage of the affinity tag. (B) Introducing a TEV cleavage site between MUN and C_2C allows the separation of MUN and C_2C. The small quantity of C_2C that remains soluble coelutes with MUN by gel filtration.

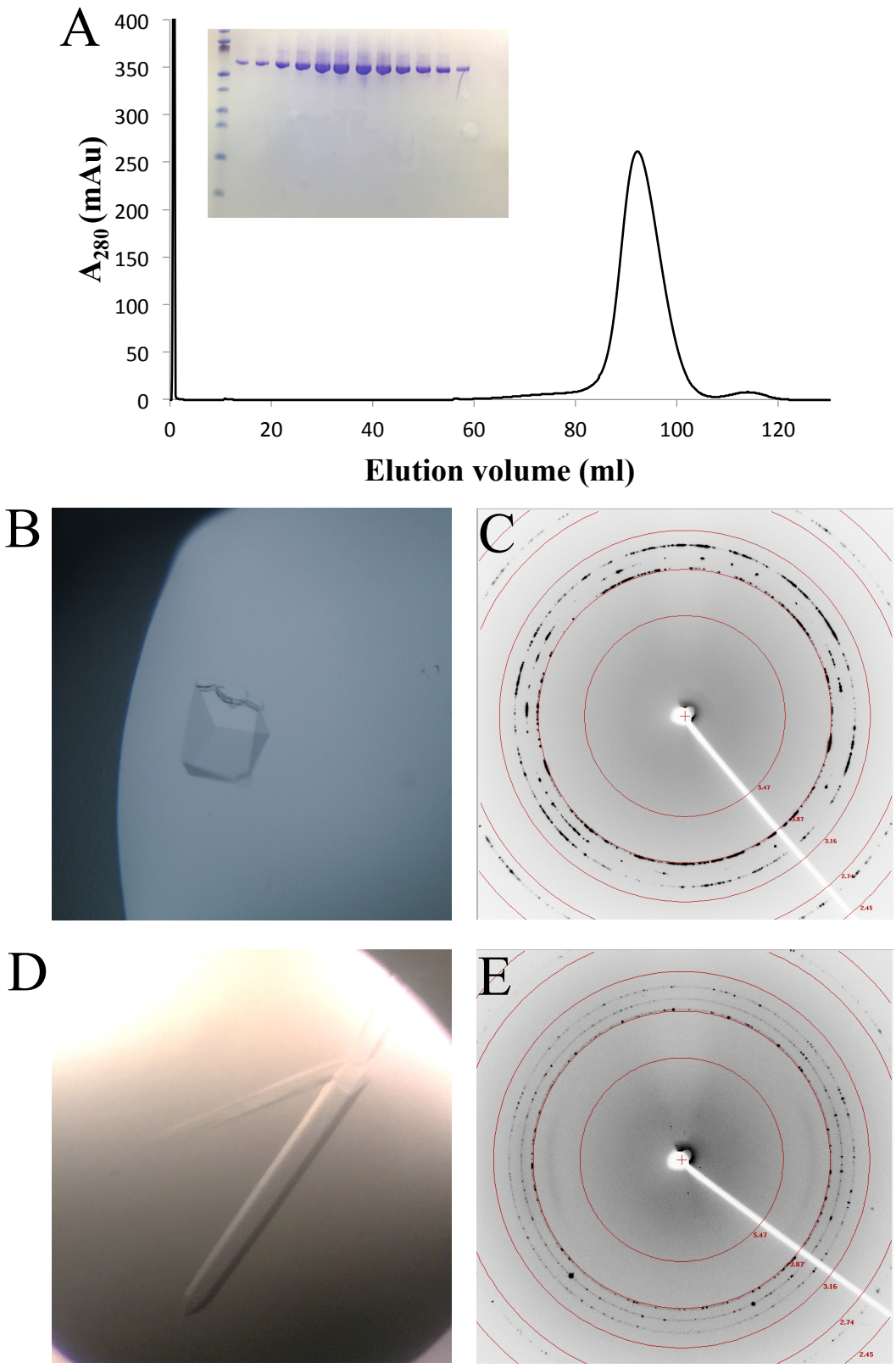

Figure 3.2 MUNCDC$_2$C purifies with high yield and readily forms single crystals with weak diffraction
(A) Example run of MUNCDC$_2$C on an S200 16/60 gel filtration column. The inset is an SDS-PAGE gel of the individual protein fractions. (B) Example of the cubic crystal form of MUNCDC$_2$C from hanging drop vapor diffusion with a well solution containing 1.6 M lithium sulfate, 0.1 M Tris, pH 8.0 and it's diffraction (C). (D) Example of the rod-like crystal form of MUNCDC$_2$C from hanging drop vapor diffusion with a well solution containing 2.4 M sodium formate, 0.1 M Tris, pH 8.5 and it's diffraction (E)

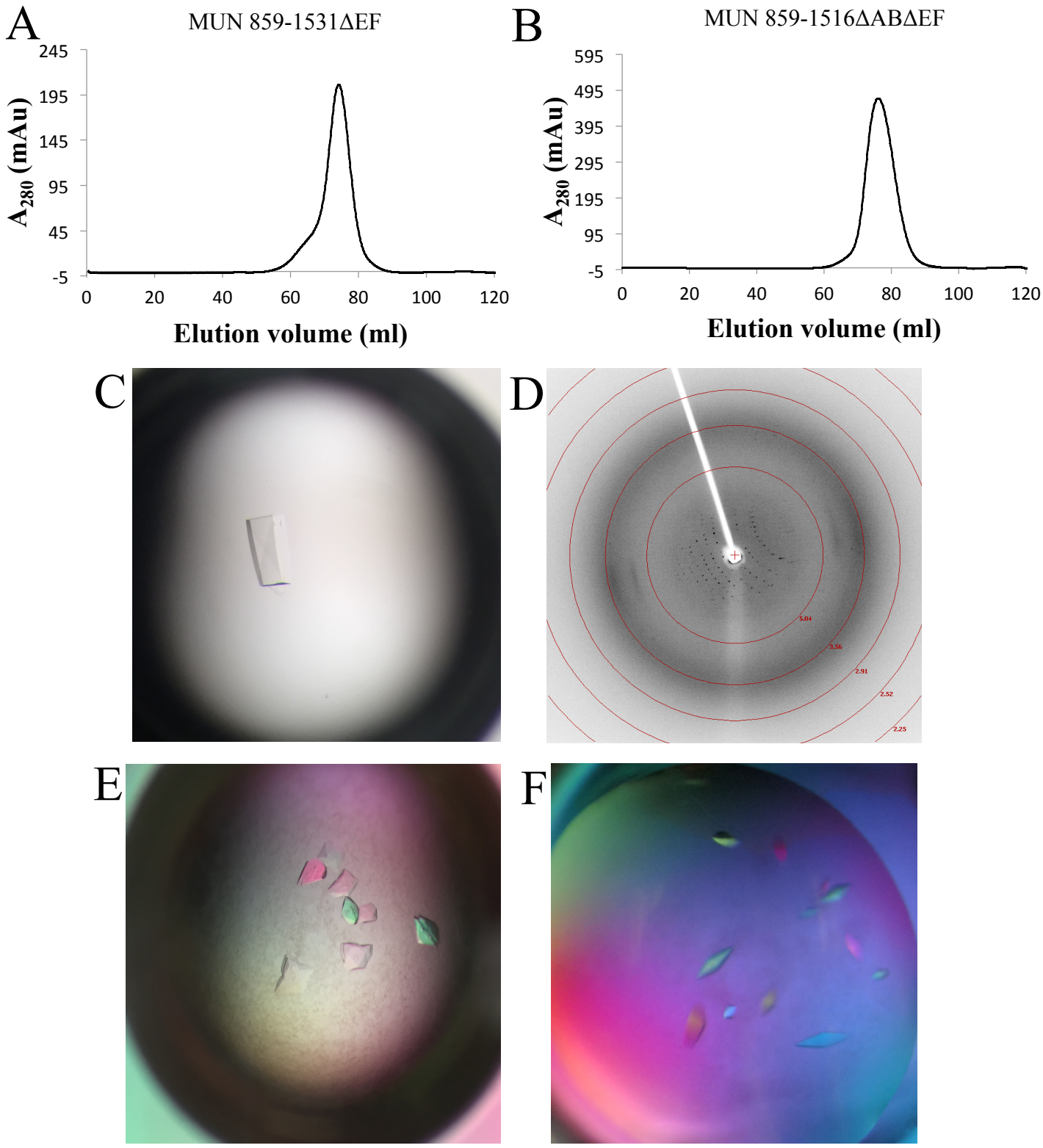

Figure 3.3 Various constructs with the Munc13-1 C_2C domain form birefringent crystals that diffract weakly
Comparison gel filtration runs for MUN domain 859-1531ΔEF (A) and MUN domain 859-1516ΔABΔEF (B) showing that truncating the MUN domain and removing the AB loop increases homogeneity and yield. (C) Crystals grown with $MUNC_2C$ 859-1735ΔEF by hanging drop vapor diffusion using 0.5 M ammonium phosphate, 0.1 M sodium acetate, pH 4.5 as the well solution and (D) an example of the poor diffraction from these crystals. (E) Crystals of $MUNC_2C$ 933-1735ΔEF grown by hanging drop vapor diffusion using 0.15 M ammonium sulfate, 15% PEG-4000, 0.1 M MES, pH 6.0 as a well solution. (F) Crystals of $C_1C_2BMUNC_2C$ 529-1735ΔEF grown by sitting drop vapor diffusion using 0.05 ammonium sulfate, 0.1 sodium citrate, 15% (w/v) PEG 8000 as the well solution. E and F were taken with a polarizing filter on the microscope to show that the crystals are birefringent and well ordered.

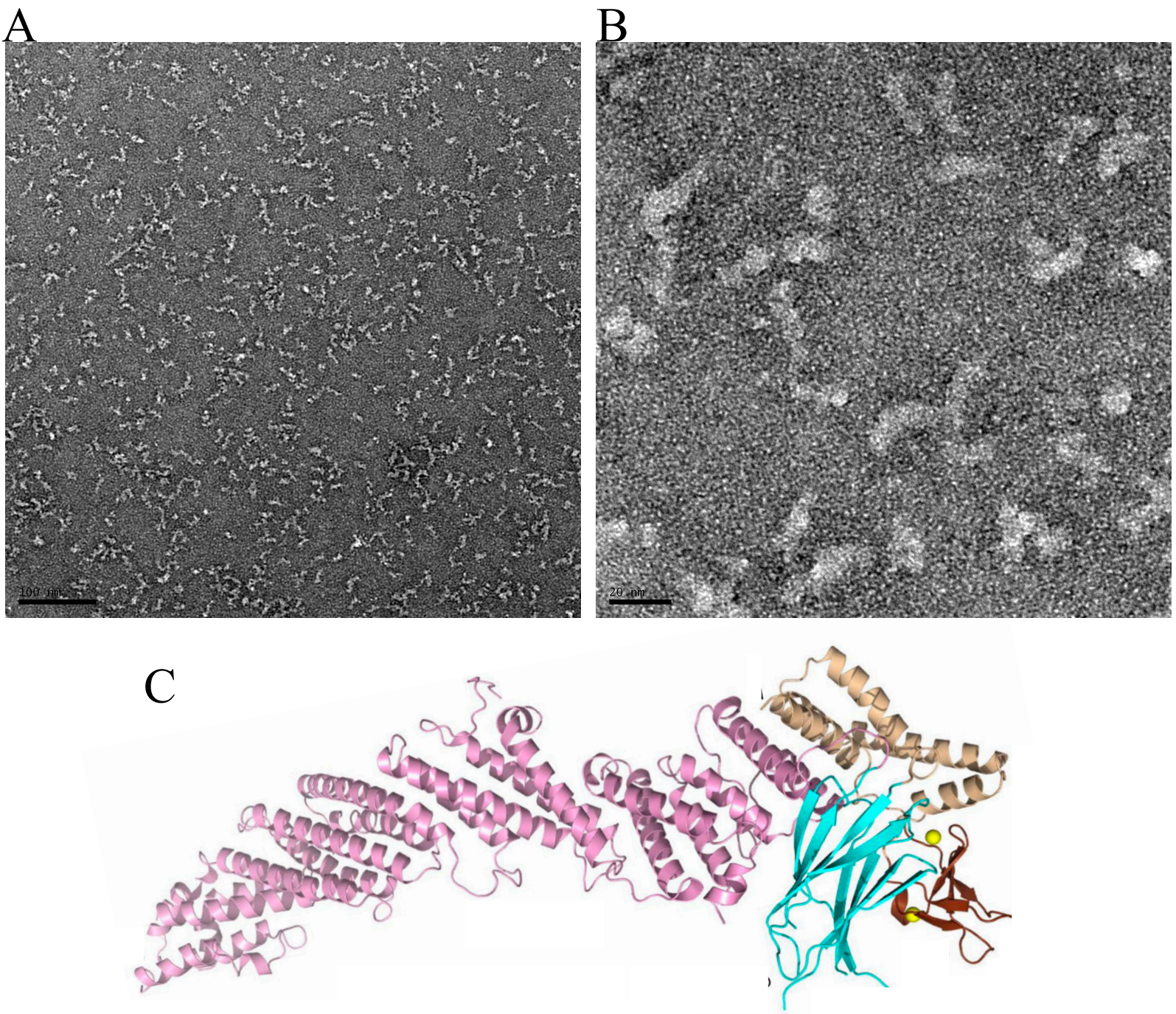

Figure 3.4 $C_1C_2BMUNC_2C$ is relatively homogenous when visualized by negative stain electron microscopy and the protein density matches the structure of C_1C_2BMUN

(A) A low magnification image of 0.01 mg/ml $C_1C_2BMUNC_2C$ showing particle homogeneity and dispersion. (B) Higher magnification images show that particles form a crescent moon shape, similar to the shape seen in the previously solved C_1C_2BMUN structure. Panel C was adapted from Rizo, 2018.

Construct	Expression	Solubility
GST-C_2C (1552-1735)	High	Insoluble
GST-C_2C (1564-1735)	High	Insoluble
GST-C_2C (1552-1720)	High	Insoluble
GST-C_2C (1564-1720)	High	Insoluble
GST-C_2C (1552-1706)	High	Insoluble
GST-C_2C (1564-1706)	High	Insoluble
MBP-C_2C (1552-1735)	High	Insoluble
C_2C-His (1552-1735) in insect cells	High	Insoluble

Table 3.1 List of C_2C constructs that were tested for expression and solubility

Fragment	Expression	Solubility	Crystallizability
MUNCD-C2C 1148-1735 ΔEF	High	Low	Yes
MUNCD-C2C 1148-1725 ΔEF	Little	Low	n/a
MUNCD-C2C 1148-1702 ΔEF	None	Low	n/a
MUNC2C 859-1735 ΔEF	High	High	No
MUNC2C 859-1735 ΔABΔEF	Little	Low	Yes
MUNC2C 933-1735 ΔEF	High	Low	Yes
C1C2BMUNC2C 529-1735	Medium	Medium	Yes

Table 3.2 List of C_2C containing fragments that were tested for expression, solubility, and crystallizability

CHAPTER 4-Membrane Bridging by Munc13 is Crucial for Neurotransmitter release

4.1 Introduction

The release of neurotransmitters by Ca^{2+}-triggered synaptic vesicle exocytosis is crucial for interneuronal communication. Exocytosis occurs in several steps that include tethering of synaptic vesicles to specialized sites of the presynaptic plasma membrane known as active zones, priming of the vesicles to a release-ready state(s) and Ca^{2+}-triggered fusion of the vesicles with the plasma membrane when an action potential causes Ca^{2+} influx into the presynaptic terminal (Sudhof, 2013). Release is exquisitely regulated by a sophisticated protein machinery that has been extensively characterized (Rizo, 2018, Brunger et al., 2018). Central components of this machinery are the SNAP receptors (SNAREs) synaptobrevin, syntaxin-1 and SNAP-25, which form a tight four-helix bundle called the SNARE complex that brings the vesicle and plasma membranes together and is critical for membrane fusion (Hanson et al., 1997, Poirier et al., 1998, Sollner et al., 1993a, Sutton et al., 1998). The SNARE complex is disassembled by N-ethylmaleimide sensitive factor (NSF) and soluble NSF attachment proteins (SNAPs) (Sollner et al., 1993a), whereas its assembly is orchestrated in an NSF-SNAP-resistant manner by Munc18-1 and Munc13s (Ma et al., 2013). The assembly pathway involves binding of Munc18-1 to a self-inhibited 'closed' conformation of syntaxin-1 (Dulubova et al., 1999, Misura et al., 2000) and to synaptobrevin to template SNARE complex formation (Baker et al., 2015, Parisotto et al., 2014, Sitarska et al., 2017) with the help of Munc13s, which facilitate opening of syntaxin-1 to form the SNARE complex (Ma et al., 2011, Richmond et al., 2001, Wang et al., 2017, Yang et al., 2015). Synaptotagmin-1 acts as the major Ca^{2+} sensor that triggers release through a combination

of interactions with membranes and the SNARE complex (Brewer et al., 2015, Chang et al., 2018, Fernandez-Chacon et al., 2001, Zhou et al., 2015).

Even with these and other advances, there are still fundamental questions that remain to be answered in order to understand the mechanisms of neurotransmitter release and its regulation. Particularly important is to elucidate the functions of mammalian Munc13s and their invertebrate homologues, Unc13s, because these large (ca. 200 kDa) proteins are essential for release (Richmond et al., 1999, Varoqueaux et al., 2002) and modulate exocytosis in multiple presynaptic plasticity processes through the various domains in its architecture (Rizo and Sudhof, 2012). Munc13-1, the most abundant isoform in the mammalian brain, contains a variable N-terminal region with a C_2A domain and a calmodulin-binding region (CaMb), as well as a conserved C-terminal region that includes the C_1, C_2B domain, MUN and C_2C domains (Figure 4.1A). The C_2A domain forms a homodimer and alternatively a heterodimer with the Rab3 effectors called RIMs (Betz et al., 2001, Dulubova et al., 2005, Lu et al., 2006), thus providing a switch that controls neurotransmitter release and couples exocytosis to diverse forms of Rab3- and RIM-dependent presynaptic plasticity (Camacho et al., 2017, Deng et al., 2011, Rizo and Sudhof, 2012); the CaMb region mediates some forms of Ca^{2+}-dependent short-term plasticity (Junge et al., 2004); the C_1 domain mediates diacylglycerol- and phorbol ester-dependent potentiation of release (Basu et al., 2007, Rhee et al., 2002); and the C_2B domain acts as a Ca^{2+}- and PIP_2- dependent modulator of short-term plasticity (Shin et al., 2010). The MUN domain is a highly elongated module that is homologous to factors involved in tethering in diverse membrane compartments and is critical for opening syntaxin-1 (Basu et al., 2005, Ma et al., 2011, Pei et al., 2009, Yu and Hughson, 2010).

The Munc13 module that has remained more enigmatic is the C_2C domain. Multiple evidence suggests that this domain is critical for Munc13 function (Liu et al., 2016, Madison et al., 2005, Stevens et al., 2005), but its biochemical properties and mechanism of action are not well understood. Based on sequence alignments, the Munc13-1 C_2C domain is not predicted to bind Ca^{2+} because it lacks some of the canonical aspartate residues that typically bind Ca^{2+} in C_2 domains (Rizo and Sudhof, 1998). Reconstitution studies of synaptic vesicle fusion and vesicle clustering assays suggested that the C_2C domain binds to membranes, leading to a model whereby the conserved Munc13-1 C-terminal region bridges the synaptic vesicle and plasma membranes through respective interactions with the C_2C domain and the C_1-C_2B region on opposite ends of the MUN domain (Liu et al., 2016) (Figure 4.2). This model is consistent with the notion that the C_2 and C_2B domains cooperate in binding to the plasma membrane through interactions with DAG and PIP_2, respectively (Basu et al., 2007, Rhee et al., 2002, Shin et al., 2010, Xu et al., 2017), and a role for Munc13-1 in bridging membranes seems natural given the homology of the MUN domain with tethering factors. However, no structure-function analysis of the C_2C domain has been described, and the physiological relevance of the membrane bridging model has not been investigated. The study presented here was designed to test this model and elucidate the function of the Munc13-1 C_2C domain, which is critical to understand the mechanism of action of Munc13s. We show that the Munc13-1 C-terminal region can bridge two membranes through the ends of its elongated structure and that the C_2C domain is essential for this ability. Moreover, impairment of the bridging activity by mutations in putative membrane-binding residues within the C_2C domain correlates with disruption of synaptic vesicle docking, priming and neurotransmitter release. Our results show that, remarkably, a single point mutation

in a 200 kDa protein such as Munc13-1 practically abolishes evoked neurotransmitter release, demonstrating the crucial importance of the membrane bridging activity for Munc13-1 function and for the sequence of events that lead to synaptic vesicle fusion.

4.2 Methods

4.2.1 Plasmids and Recombinant Proteins

Expression and purification of full-length *Homo sapiens* SNAP-25A (with its four cysteines mutated to serine), full-length *Rattus norvegicus* synaptobrevin-2, full-length *Rattus norvegicus* Munc18-1, full- length *Cricetulus griseus* NSF V155M mutant, full-length *Bos taurus* α-SNAP and *Rattus Norvegicus* syntaxin-1 (2-253) in *E. coli* were described previously (Chen et al., 2006, Dulubova et al., 2007, Dulubova et al., 1999, Ma et al., 2013). All recombinant *Rattus Norvegicus* Munc13-1 fragments contained a deletion in a large variable loop (residues 1408-1452) that improves the solubility (Ma et al., 2011). Expression and purification of Munc13-1 $C_1C_2BMUNC_2C$ (residues 529-1735, Δ1408-1452) in Sf9 cells was described earlier (Liu et al., 2016). Standard PCR-based recombinant DNA techniques with custom-designed primers were used to derive vectors to express other Munc13-1 fragments, including vectors to express Munc13-1 $C_1C_2BMUNC_2C$ (residues 529-1516, Δ1408-1452) in Sf9 insect cells and in *E. coli*, and vectors to express the MUN domain (residues 859-1516, Δ1408-1452), $MUNC_2C$ (residues 859-1735, Δ1408-1452) and $C_1C_2BMUNC_2C$ (residues 529-1735, Δ1408-1452) (WT and K1613A/K1616A, R1598E, F1658E and R1598E/F1658E mutants) in *E. coli*. The constructs to express the Munc13-1 C_1C_2BMUN1516 and $C_1C_2BMUNC_2C$ in *E. coli* were prepared by copying the corresponding Munc13-1 sequences from the vector used for Sf9

cell expression into a pET28a vector kindly provided by Reinhard Jahn (Kreutzberger et al., 2017). Expression and purification of C_1C_2BMUN1516 in Sf9 insect cells was performed as described earlier for the C_1C_2BMUNC_2C fragment (Liu et al., 2016). Expression and purification of the MUN domain and the MUNC_2C fragment in *E. coli* was performed as described previously for a slightly longer fragment spanning the MUN domain (residues 859-1531, Δ1408-1452) (Ma et al., 2011). Uniform ^{15}N-labeling and ^{2}H,^{13}CH$_3$-ILV-labeling were accomplished as described previously (Dulubova et al., 1999, Tugarinov et al., 2004).

Expression and purification of His$_6$-Munc13-1 C_1C_2BMUN1516 and C_1C_2BMUNC_2C (WT and mutants) encoded in a pET28a vector was performed in *E. coli* BL21 (DE3) cells. Transformed cells were grown in the presence of 50 μg/ml kanamycin to an OD600 of ~0.8 and induced overnight at 16°C with 500 μM IPTG. Cells were harvested by centrifugation and re-suspended in 50 mM Tris, pH 8, 250 mM NaCl, 1 mM TCEP, 10% glycerol (v/v) prior to lysis. Cell lysates were centrifuged for 30 minutes at 48,000 x g to clarify the lysate and then incubated with Ni-NTA resin for 30 minutes at room temperature. The resin was washed with re-suspension buffer and re-suspension buffer with 750 mM NaCl to remove contaminants. Nuclease treatment was performed on the beads for 1 hour at room temperature using 250 U of Pierce Universal Nuclease (Thermo Fisher Scientific) per liter of cells. Protein was eluted using re-suspension buffer with 500 mM imidazole and dialyzed against 50 mM Tris, pH 8, 250 mM NaCl, 1 mM TCEP, 2.5 mM $CaCl_2$, 10% glycerol (v/v), overnight at 4°C in the presence of thrombin. The solution was re-applied to Ni-NTA resin to remove any uncleaved protein and diluted twentyfold with 20 mM Tris, pH 8, 1 mM TCEP, 10% glycerol (v/v). Diluted protein was subjected to anion exchange chromatography using a HiTrapQ HP column (GE Life Sciences)

and eluted in 20 mM Tris, pH 8, 1 mM TCEP, 10% glycerol (v/v) with a linear gradient from 1% to 50% of 1 M NaCl.

His-full-length *s*yntaxin-1A encoded in a pET28a was expressed in BL21 (DE3) *E. coli*. Transformed cells were grown in the presence of 50 μg/ml kanamycin to an OD600 of ~0.8 and induced overnight at 20°C with 400 μM IPTG. Cells were harvested by centrifugation and re-suspended in extraction buffer (20 mM Hepes, pH 7.4, 500 mM NaCl, 8 mM imidazole) prior to lysis. Cell lysates were centrifuged at 14,500 x g for 20 minutes. The supernatant was discarded and the pellet containing the protein was re-suspended and pelleted again. The pellet was re-suspended in extraction buffer with 2% Triton-X 100 (Sigma-Aldrich) and 6 M urea and incubated for 1 hour at 4°C to solubilize the protein. Cell debris was pelleted by centrifugation at 48,000 x g for 1 hour and the supernatant was applied to Ni- NTA resin. The resin was washed sequentially with wash buffer (20 mM Hepes, pH 7.4, 500 mM NaCl, 20 mM imidazole) containing 6 M urea, 10% glycerol (v/v), 1% Triton-X 100 and then 20% glycerol (v/v), 1% Triton-X 100 and then 1% Triton-X 100 and finally 0.1% n-Dodecylphosphocholine (DPC; Anatrace). The protein was eluted in elution buffer (20 mM Hepes, pH 7.4, 500 mM NaCl, 400 mM imidazole, 0.1 DPC) and the Hisremoved by thrombin cleavage overnight at 4°C. Gel filtration was performed on a Superdex 200 10/300 GL column (GE Life Science) in 20 mM Tris, pH 7.4, 150 mM NaCl, 1 mM TCEP, 0.2% DPC.

4.2.2 NMR Spectroscopy

NMR spectra were acquired at 25°C on Agilent DD2 spectrometers operating at 600 or 800 MHz and equipped with cold probes. ^{1}H-^{13}C HMQC spectra (Tugarinov et al., 2004) were

obtained on samples containing 10-15 μM $^{2}H,^{13}CH_3$-ILV-labeled Munc13-1 MUN or $MUNC_2C$ dissolved in 20 mM Tris (pH 8.0), 150 mM NaCl, 2 mM TCEP, using D_2O as the solvent. ^{1}H-^{15}N HSQC spectra (Zhang et al., 1994) were obtained with samples containing 30 μM ^{15}N-labeled syntaxin-1(2-253) alone or with 30 μM Munc13-1 MUN or $MUNC_2C$ in 20 mM Tris, pH 7.4, 125 mM NaCl, 2 mM TCEP, 6% D_2O. Total acquisition times were 10 hr and 6.6 hr for ^{1}H-$^{13}C_3$ HMQC and ^{1}H-^{15}N HSQC spectra, respectively. All NMR data were processed using NMRPipe (Delaglio et al., 1995) and analyzed with NMR View (Johnson and Blevins, 1994).

4.2.3 Dynamic Light Scattering

To prepare phospholipid vesicles, 1-palmitoyl-2-oleoyl-sn-glycero-3-phosphocholine (POPC), 1,2- dioleoyl-sn-glycero-3-phospho-L-serine (DOPS), 1-palmitoyl-2-oleoyl-sn-glycero-3-phosphoethanolamine (POPE), L-a-Phosphatidylinositol-4,5-bisphosphate (PIP_2), 1-palmitoyl-2-oleoyl-*sn*-glycerol (DAG), and cholesterol dissolved in chloroform were mixed at the desired ratios and then dried under a stream of nitrogen gas. The dried vesicles were left overnight in a vacuum chamber to remove the organic solvent. The next day the lipid films were hydrated with 25 mM HEPES, pH 7.4, 150 mM KCl, 10% glycerol (v/v) and vortexed for 5 minutes followed by five freeze-thaw cycles. Large unilamellar vesicles were prepared by extruding the hydrated lipid solution through a 100 nm polycarbonate filter 31 times with an Avanti Mini-Extruder. T-type liposomes contained 38% POPC, 18% DOPS, 20% POPE, 2% PIP2, 2% DAG, and 20% Cholesterol, and V-type liposomes contained 39% POPC, 19% DOPS, 22% POPE, and 20% Cholesterol. Liposome clustering induced by Munc13 fragments was analyzed using a Wyatt Dynapro Nanostar (Wyatt Technology) dynamic light scattering instrument equipped with a

temperature controlled microsampler as previously described (Liu et al., 2016). Briefly, the specified Munc13-1 fragment (500 nM) was incubated at room temperature for 2 minutes with T-liposomes (250 μM total lipid) and V-liposomes (125 μM total lipid) in 25 mM HEPES, pH 7.4, 150 mM KCl, 100 μM EGTA, 10% glycerol (v/v) prior to measuring the particle size. After the addition of 600 μM Ca^{2+} (to achieve a 500 μM free Ca^{2+} concentration) the sample was incubated for an additional 3 minutes before measurement.

4.2.4 Liposome fusion assays

Liposome lipid and content mixing assays were performed basically as previously described (Liu et al., 2017, Liu et al., 2016). To prepare the phospholipid vesicles, POPC, DOPS, POPE, PIP2, DAG, 1,2- dipalmitoyl-*sn*-glycero-3-phosphoethanolamine-N-(7-nitro-2-1,3-benzoxadiazol-4-yl) (ammonium salt) (NBD-PE), 1,2-Dihexadecanoyl-*sn*-glycero-3-phosphoethanolamine (Marina Blue DHPE), and cholesterol in chloroform were mixed at the desired ratio and dried under a stream of nitrogen gas. T-liposomes contained 38% POPC, 18% DOPS, 20% POPE, 2% PIP2, 2% DAG, and 20% Cholesterol, and V-liposomes contained 39% POPC, 19% DOPS, 19% POPE, 20% Cholesterol, 1.5% NBD PE, and 1.5% Marina Blue DHPE. The dried lipids were left overnight in a vacuum chamber to remove the organic solvent. The next day the lipid films were hydrated with 25 mM Hepes, pH 7.4, 150 mM KCl, 1 mM TCEP, 2% n-Octyl-β-D- glucoside (β-OG) and 10% glycerol (v/v) by vortexing for 5 minutes. Rehydrated lipids for T-liposomes were mixed with protein and dye to get a final concentration of 4 mM lipid, 5 μM full-length syntaxin-1, 25 μM full-length SNAP-25, and 4 μM R-phycoerythrin biotin-XX conjugate (Invitrogen). Rehydrated lipids for V-liposomes were mixed

with protein and dye to get a final concentration of 4 mM lipid, 8 μM full-length synaptobrevin, and 8 μM Cy5-streptavidin conjugate (Seracare Life Sciences Inc.). Lipid mixtures were dialyzed 1 hr, 2 hr and overnight at 4°C in 25 mM Hepes, pH 7.4, 150 mM KCl, 1 mM TCEP, 10% glycerol (v/v) in the presence of Amberlyte XAD-2 beads (Sigma) to remove the detergent and promote the formation of proteoliposomes. The next day the proteoliposomes were harvested and mixed with Histodenz (Sigma) to a final concentration of 35%. Proteoliposome mixtures were added to a centrifuge tube with 25% Histodenz and 25 mM Hepes, pH 7.4, 150 mM KCl, 1 mM TCEP, 10% glycerol layered on top. The proteoliposomes were spun at 4°C for 1.5 hours at 55,000 RPM in an SW-60 TI rotor and the top layer was collected. Concentrations of the final T-proteoliposomes were measured by the Stewart method (Stewart, 1980). V-proteoliposome concentrations were estimated from the UV-vis absorption using a standard curve made using known quantities of liposomes containing 1.5% NBD-PE.

To perform the fusion assays, T-liposomes (250 μM total lipid) were first incubated with 1 μM Munc18, 0.8 μM NSF, 2 μM α-SNAP, 2 mM ATP, 2.5 mM Mg^{2+}, 5 μM streptavidin, and 100 μM EGTA for 15-25 minutes at 37°C, and then were mixed with V-liposomes (125 μM total lipid), 1 μM SNAP-25, and wild type Munc13-1 fragments at the specified concentration. After 5 minutes 0.6 mM Ca^{2+} was added to stimulate fusion, and 1% β-OG was added after 25 minutes to solubilize the liposomes. The fluorescence signals from Marina Blue (excitation at 370 nm, emission at 465 nm) and Cy5 (excitation at 565 nm, emission at 670 nm) were recorded to monitor lipid and content mixing, respectively. The lipid mixing data were normalized to the maximum fluorescence signal observed upon detergent addition. The content mixing data were

normalized to the maximum Cy5 fluorescence observed after detergent addition in control experiments without external streptavidin.

4.2.5 Liposome co-sedimentation assays

Liposome co-sedimentation assays were performed as described with some modifications (Shin et al., 2010). Briefly, lipid mixtures containing 38% POPC, 18% DOPS, 19% POPE, 2% PIP2, 2% DAG, 20% cholesterol, and 1% Rhodamine-PE were dried under a stream of nitrogen gas and kept under vacuum overnight. The next day the lipid film was re-suspended in buffer (25 mM Hepes, pH 7.4, 150 mM KCl, 1 mM TCEP, 500 mM sucrose), frozen and thawed 5 times, and then extruded through a 100 nm polycarbonate filter 31 times. Liposomes were diluted in sucrose-free buffer and spun at 160,000 g for 30 minutes to pellet heavy liposomes. The supernatant was removed and liposomes were re-suspended in sucrose-free buffer. Liposomes were then pelleted at 17,000 g and re-suspended in sucrose free buffer two more times. The final liposome concentration was estimated based on the absorbance of Rhodamine-PE in a known liposome sample. Liposome solutions containing 2 mM liposome and 2 μM protein were incubated for 30 minutes at room temperature. The liposomes and bound protein were pelleted by centrifugation at 17,000 g for 20 minutes. The supernatant was removed and the liposomes were re-suspended in buffer. Re-suspended samples were boiled for 5 minutes and analyzed by SDS- PAGE and coomassie blue staining.

4.2.6 Cryo-Electron Tomography

Specimens were prepared following our standard protocol for lipid and content mixing assays (see above), mixing V-liposomes with T-liposomes that had been pre-incubated with Munc18-1, NSF and α-SNAP in the presence of Munc13-1 C1C2BMUNC2C fragment and 0.1 μM EGTA. 3 μL of the solution were added to a Lacey carbon grid (200-mesh; Electron Microscopy Sciences) that was negatively glow- discharged for 30 s at 30 mA. 1 μL of 10-fold concentrated solution of 10-nm BSA colloidal gold (Sigma- Aldrich, St. Louis, MO) was quickly mixed into the vesicle solution (Iancu et al., 2006), before blotting excess liquid away for ~1.5 s using Whatman filter paper and plunge-freezing the grid in liquid ethane using a CP3 plunge-freezing machine (Gatan, Pleasanton CA). The process from mixing V- and T- liposomes to cryo-immobilization took ~40 s.

The vitrified vesicle samples were imaged using a Titan Krios 300 kV transmission electron microscope (FEI, Hillsboro, OR) equipped with a post-column Gatan imaging filter (Gatan, Pleasanton CA), and a Volta Phase Plate (FEI). The SerialEM software was used to collect tilt series under low-dose mode (Mastronarde, 2005). Tilt series were recorded using a dose-symmetric tilting scheme (Hagen et al., 2017) and a tilting range from −60° to +60° with an increment of 2°. Images were recorded at 26,000 magnification on a K2 Summit direct electron detector (Gatan, Pleasanton CA) with an effective pixel size of 5.5 Å, and 16 frames were recorded over 5.6 s exposure at a dose rate of 7.8 electrons/pixel/s for each tilt image. The cumulative dose was ~100 $e^-/Å^2$ per tilt series. The defocus was set to -0.5 μm (with phase plate) and the energy filter was in zero-loss mode with a slit width of 20eV. The tilt series images were

aligned and reconstructed in the IMOD software package (Kremer et al., 1996) using fiducial alignment and weighted back-projection. To reduce noise, the cryo-tomograms were either binned or slightly filtered using a weighted median filter. For 3D representation, selected areas of the cryo-tomograms were graphically modeled using the modeling tools in IMOD.

4.2.7 Homology modeling

The SWISS-MODEL server was used to perform homology modeling (Waterhouse et al., 2018) of the C-terminal sequence spanning the Munc13-1 C_2C domain (residues 1532-1735). Templates for model building were selected based on the Global Model Quality Estimate (GMQE) score and sequence identity. Final models were built using the RIM1 C2B domain, synaptotagmin-1 C2B domain, synaptotagmin-3 C2A domain and PKC gamma type C2 domain as templates (PDB accession codes 2Q3X, IUOV, 1DQV and 2UZP, respectively).

4.2.8 Munc13-1 rescue vectors and lentivirus production

Construction of Munc13-1 full length (WT), truncated Munc13-1 C_2C domain (Munc13-1 ΔC_2C), Munc13-1 R1598E, Munc13-1 F1618E, Munc13-1 R1598E/F1618E and Munc13-1 K1613A/K1616A constructs was performed by PCR amplification from rat *Unc13a* splice variant (Basu et al., 2005). All PCR products were generated with the appropriate pairs of forward primer and reverse primer harboring a 3xFLAG sequence (Sigma-Aldrich, Hamburg, Germany). The corresponding PCR products with the flag sequence were fused to a P2A linker (Kim et al., 2011) after a nuclear localized GFP sequence. All Munc13-1-flag bicistronic constructs were subsequently cloned into a lentiviral shuttle vector under the expressional

regulation of human synapsin-1 promoter. Lentiviral particles were produced and concentrated as described previously (Lois et al., 2002).

4.2.9 Hippocampal neuronal culture and lentiviral infection

All animal experiments were conducted according to the rules of the Berlin state government agency for Health and Social Services and the animal welfare committees of Charité Medical University Berlin, Germany (license no. T 0220/09). Primary neuronal hippocampal cultures were prepared from embryonic day 18.5 *Munc13-1/2* DKO mouse embryos or postnatal day 0 C57BL/6N mouse. Hippocampi were dissected and enzymatically treated with 25 units ml^{-1} of papain for 45 min at 37°C. After papain inactivation, hippocampi were mechanically dissociated in Neurobasal-A medium containing B-27, Glutamax and penicillin/streptomycin. Hippocampal neurons were seeded at 3 x 10^3 cells onto 30 mm coverslips previously covered with a dotted pattern of microislands of astrocytes for electrophysiological recordings in autaptic cultures, at 100 x 10^3 cells onto 6 mm sapphire disks previously covered with the astrocyte feeder layer for high pressure freezing fixation and at a density of 25 x 10^3 cells onto 10 mm coverslips previously covered with an astrocyte feeder layer for immunocytochemical staining. 24 h after plating neurons were infected with the different lentiviral rescue constructs and incubated at 37°C and 5% CO_2 for 14-18 days.

4.2.10 Immunocytochemistry

Munc13-1/2 DKO or DKO hippocampal neurons infected with the different rescue constructs were fixed in 4% paraformaldehyde in PBS at DIV 16. After fixation neurons were

permeabilized in PBS-Tween 20 (PBS-T), quenched in PBS-T containing glycine, blocked in PBS-T containing 5% normal donkey-serum and incubated overnight at 4°C with mouse monoclonal antibody against Flag® M2 (1:100; Sigma, F3165) and guinea pig polyclonal antibody VGLUT 1 (1:4000; Synaptic System, 135304). Primary antibodies were labeled with Alexa Fluor 488 Affinipure donkey anti-rabbit IgG and Alexa Fluor 647 Affinipure donkey anti-guinea pig IgG (1:500 each; Jackson ImmunoResearch). Coverslips with the hippocampal cultures were mounted with Mowiol 4-88 antifade medium (Polysciences Europe). Neuronal images were acquired using a Leica TCS SP8 confocal laser-scanning microscope equipped with a 63x oil immersion objective and Leica Application Suite X (LAsX) software. Confocal fluorescent images were taken at 1024 x 1024 pixels with a z step size of 0.3 µm. Ten independent neurons for each cultured and three different cultures per group were imaged and analyzed using ImageJ software.

4.2.11 Electrophysiology

Whole-cell voltage clamp recordings were performed on autaptic hippocampal neurons at DIV14-18 at room temperature. Currents were acquired using a Multiclamp 700B amplifier and a Digidata 1440A digitizer (Axon instrument). Series resistance was set at 70% and only cells with series resistances <10 MΩ were selected. Data were recorded using Clampex 10 software (Axon instrument) at 10 kHz and filtered at 3 kHz. Borosilicate glass pipettes with a resistance around 3 MΩ were used and filled with an intracellular solution contained the following (in mM): 136 KCl, 17.8 HEPES, 1 EGTA, 4.6 $MgCl_2$, 4 Na_2ATP, 0.3 Na_2GTP, 12 creatine phosphate, and 50 Uml^{-1} phosphocreatine kinase; 300 mOsm; pH 7.4. Neurons were

continuously perfused with standard extracellular solution including the following (in mM): 140 NaCl, 2.4 KCl, 10 HEPES, 10 glucose, 2 $CaCl_2$, 4 $MgCl_2$; 300 mOsm; pH 7.4. Spontaneous release was measured by recording mEPSC for 30 s at -70 mV and for an equal amount of time in 3 mM of the glutamate antagonist Kynurenic Acid to detect false positives events. For each cell, data were filtered at 1 kHz and analyzed using template-based miniature event detection algorithms implemented in the AxoGraph X software. Action potential-evoked EPSCs were elicited by 2 ms somatic depolarization from −70 to 0 mV. To estimate the readily-releasable pool (RRP) size, 500 mM hypertonic sucrose added to standard extracellular solution, was applied for 5 s using a fast-flow system (Pyott and Rosenmund, 2002). For vesicular release probability (P_{vr}) calculations, the ratio of EPSC charge to RRP charge was determined. Short term plasticity was examined either by evoking 2 AP with 25 ms interval (40 Hz) or a train of 50 AP at an interval of 100 ms (10 Hz) was applied. Data were analyzed offline using Axograph X (Axograph Scientific).

4.2.12 High-pressure freezing fixation and transmission electron microscopy (TEM)

Hippocampal *Munc13-1/2* DKO neurons expressing the different Munc13-1 WT and C2C point mutants, immersed in the recording solution containing 2 mM Ca^{2+} and 4 mM Mg^{2+}, were frozen using the high- pressure freezer EM ICE (Leica). After the cryofixation, samples were processed as previously described (Watanabe et al., 2013). Briefly, samples were transferred to an anhydrous acetone solution containing 1% osmium tetroxide, 1% glutaraldehyde and 1% ddH_20 and processed for the freeze-substitution. The freeze-substitution was performed in AFS2 (Leica) over a period of two days with the following program: −90 °C

for 5 h, 5 °C per hour to −20 °C, 12 h at −20 °C and 10 °C per hour to 20 °C. Once at room temperature, samples were en bloc stained with 0.1% uranyl acetate and infiltrated in increasing concentration of a mixture of epoxy resin (Epon 812) and araldite. Subsequently, samples were flat embedded in resin and cured for 48 h at 60 °C. Serial 40-50 nm thick sections were cut using an Ultracut UCT ultramicrotome (Leica) equipped with a diamond knife (Diatome Ultra 45) and collected onto formvar-coated copper grids. Sections were stained with 1% uranyl acetate and lead citrate for ultrastructural examination. The ultrastructure of the synapse was observed using a FEI Tecnai G20 transmission electron microscope (TEM) operated at 80–120 keV and digital images were acquired with a Veleta 2 K × 2 K CCD camera (Olympus) at 35,000x magnification. Synapses were defined as boutons that contains synaptic vesicles attached to a postsynaptic terminal with a visible postsynaptic density. Around 100-200 synaptic profiles per group were collected blindly and numbers of docked synaptic vesicles per active zone were analyzed using a custom-written analysis program developed for ImageJ and Matlab scripts (Watanabe et al., 2013).

4.2.13 Statistics

Electrophysiological and electron microscopy data were acquired and analyzed blinded. To minimize variability among the electrophysiological datasets, an approximately equal number of autaptic neurons were recorded from control and experimental groups per day. Data were collected from 2 to 3 independent hippocampal cultures and are expressed as mean ± standard error of the mean (SEM). Statistical comparison was performed by Mann Whitney test (in plots with two groups) or by Kruskal- Wallis one-way ANOVA followed by a multiple comparison

Dunn's post hoc test (plots with more that 2 groups). Statistical differences among datasets were considered significant at $p < 0.05$.

4.3 Results

4.3.1 Functional consequences of deleting the Munc13-1 C_2C domain

Using electrophysiological experiments in neuronal autaptic cultures, we previously showed that the conserved C-terminal region spanning the C_1, C_2B, MUN and C_2C domains of Munc13-1 ($C_1C_2BMUNC_2C$) can partially rescue the readily-releasable pool (RRP) and evoked neurotransmitter release in *Munc13- 1/2* double knockout (DKO) neurons, while an analogous fragment lacking the C_2C domain was practically unable to rescue release (Liu et al., 2016). These results supported the notion that the C_2C domain is crucial for Munc13-1 function, but we later showed that the incomplete rescue obtained with $C_1C_2BMUNC_2C$ arises in part because removal of the N-terminal region containing the C_2A domain impairs synaptic vesicle docking (Camacho et al., 2017). Since our model postulates that the C_2C domain plays a key role in membrane bridging by the Munc13-1 C-terminal region and this mechanism might be at least partially redundant with the function of the C_2A domain in docking, it became important to test the functional importance of the C_2C domain in the context of full-length Munc13-1. For this purpose, we used a rescue approach with autaptic neuronal cultures from *Munc13-1/2* DKO mice, where Ca^{2+}- evoked release, spontaneous release and sucrose-induced release, which measures the readily release pool (RRP) of vesicles, are completely abolished (Varoqueaux et al., 2002).

Lentiviral expression of full-length wild type (WT) Munc13-1 in neuronal autaptic cultures from *Munc13-1/2* DKO mice robustly rescue evoked release, as observed previously (Liu et al., 2016), but almost no evoked release was observed when Munc13-1 lacking the C_2C domain (Munc13-1 ΔC_2C) was expressed (Figure 4.1 B,C). Deletion of the C_2C domain also reduced the RRP strongly, although the impairment was not as severe as that observed for evoked release (Figure 4.1 D,E). As a result, the release probability of the few vesicles that were primed was decreased for the Munc13-1 ΔC_2C rescue compared with the WT rescue (Figure 4.1 F). As expected from the decrease in vesicular release probability, we also found that neurons rescued with Munc13-1 ΔC_2C exhibited facilitation upon repetitive stimulation, unlike the rescue with WT Munc13-1 (Figure 4.1 G). These results demonstrate that the Munc13-1 C_2C domain plays a critical role in synaptic exocytosis, in agreement with previous results (Liu et al., 2016, Madison et al., 2005, Stevens et al., 2005), and show that this role is important for vesicle priming but is even more crucial for evoked neurotransmitter release.

4.3.2 The C_2C domain is required for membrane bridging by the Munc13-1 C-terminal region

Multiple attempts to express the isolated Munc13-1 C_2C domain in order to characterize its structure and biochemical properties failed to yield soluble, well-behaved protein fragments. However, a longer fragment including the C_2C domain and the preceding MUN domain ($MUNC_2C$) can be readily expressed in bacteria (Liu et al., 2016), suggesting that the C_2C domain requires packing against the MUN domain for proper folding. To confirm that the C_2C domain is folded within the $MUNC_2C$ fragment, we compared ^{1}H-^{13}C heteronuclear multiple quantum coherence (HMQC) spectra of perdeuterated samples of the Munc13-1 MUN domain

and MUNC$_2$C fragment that were specifically ^{1}H,^{13}C-labeled at Ile, Leu and Val methyl groups (^{2}H,^{13}CH$_3$-ILV-labeled). The spectrum of the MUNC$_2$C fragment contains additional cross-peaks in well-resolved regions (Figure 4.3 A,B), showing that the C$_2$C domain is structured. In addition, the shifts observed in some of the cross-peaks of the MUN domain upon inclusion of the C$_2$C domain support the notion that there are intramolecular interactions between the two domains.

Since yeast-two-hybrid assays indicated that a C-terminal fragment spanning part of the MUN domain and the C$_2$C domain of Munc13-1 bind to syntaxin-1 (Betz et al., 1997), we tested whether the C$_2$C domain contributes to such binding using NMR spectroscopy. For this purpose, we acquired ^{1}H-^{15}N heteronuclear single quantum coherence (HSQC) spectra of ^{15}N-labeled cytoplasmic region of syntaxin-1 (residues 2-253) in the absence and presence of unlabeled Munc13-1 MUN domain and MUNC$_2$C fragment. Both fragments caused similar, limited broadening of the cross-peaks of syntaxin-1(2-253) (Figure 4.3 C-E), but all cross-peaks remained observable. Given the large size of these Munc13-1 fragments (residues 859-1531 and 859-1735, respectively), substantial binding would be expected to induce much stronger broadening (Rizo et al., 2012). Hence, these results show that the two fragments bind very weakly to the syntaxin-1 (2-253) fragment and that the C$_2$C domain does not enhance the weak interaction involving the MUN domain, as the presence of the C$_2$C domain in MUNC$_2$C did not increase the broadening.

In previous experiments, we did not detect binding of the MUNC$_2$C fragment to membranes in liposome co-floatation assays, but the C$_2$C domain appeared to contribute to the

ability of a fragment spanning the entire Munc13-1 C-terminal region ($C_1C_2BMUNC_2C$) to bridge liposomes containing synaptobrevin (V-liposomes) with liposomes containing syntaxin-1-SNAP-25 heterodimers (T-liposomes) (Liu et al., 2016). Since the T-liposomes contained DAG and PIP_2 to mimic the lipid composition of the plasma membrane and the MUN domain has a highly elongated structure (Xu et al., 2017, Yang et al., 2015), with the C_1-C_2B region and the C_2C domain attached at opposite ends, these results suggested that $C_1C_2BMUNC_2C$ bridges the T- and V-liposomes through interactions of the C_1 and C_2B domains with the T-liposomes and the C_2C domain with the V-liposomes (Figure 4.2) (note that the C_1 and C_2B domains bind to DAG and PIP_2, respectively). To test this model and directly visualize whether the $C_1C_2BMUNC_2C$ fragment can indeed bridge two membranes through the ends of its highly elongated structure, we acquired cryo-electron tomography (cryo-ET) images of reconstitution reactions where T-liposomes and V-liposomes were mixed together with Munc13-1 $C_1C_2BMUNC_2C$, Munc18-1, NSF and αSNAP. Indeed, we observed many instances where two liposomes were bridged by highly elongated densities (Figure 4.4 A-E). Measurements made for 70 of these highly elongated densities yielded an average length of 22 nm, consistent with the approximate length that can be predicted for $C_1C_2BMUNC_2C$ based on the crystal structure of the Munc13-1 C_1C_2BMUN fragment (ca. 20 nm long (Xu et al., 2017)). Because the three-dimensional structures of all the other proteins included in the samples are known and none of them has such an elongated shape (Rizo, 2018), these densities can be attributed unambiguously to the Munc13-1 $C_1C_2BMUNC_2C$ fragment. We note that liposomes generally formed clusters where each liposome pair was bridged by at least one, and often more, $C_1C_2BMUNC_2C$ molecules. This observation, together with the fact that no binding of the $MUNC_2C$ fragment to

liposomes was observed in co-floatation assays (Liu et al., 2016), suggest that the interaction of a single C_2C domain with membranes is weak, but the C_2C domain can contribute to membrane-membrane bridging due to cooperativity between $C_1C_2BMUNC_2C$ molecules. In this context, it is worth noting that super-resolution imaging revealed the formation of supramolecular assemblies by multiple Munc13-1 molecules at presynaptic release sites (Sakamoto et al., 2018).

The cryo-ET images provide a direct visualization of how the Munc13-1 $C_1C_2BMUNC_2C$ fragment can bridge two membranes through the sequences located opposite ends of the MUN domain, as previously proposed based on dynamic light scattering (DLS) experiments that revealed the ability of this fragment to cluster liposomes (Liu et al., 2016). The importance of the C_2C domain for bridging might be questioned because the C_1C_2BMUN fragment that we used in previous studies was also able to cluster liposomes (Liu et al., 2016). However, in this previous study we noted that the C_1C_2BMUN fragment used ended at residue 1531 and that the sequence spanning residues 1517 to 1531 is not part of the folded structure of the MUN domain. This sequence is highly hydrophobic and is probably folded in the $C_1C_2BMUNC_2C$ fragment, but is not observable in the structure of C_1C_2BMUN (Xu et al., 2017), remaining exposed and likely mediating non-specific binding to membranes that explains the ability of the C_1C_2BMUN fragment to cluster liposomes (Liu et al., 2016). Therefore, to test to what extent the C_2C domain is important for the vesicle clustering ability of the Munc13-1 C-terminal region, we prepared a new C_1C_2BMUN fragment that ends at residue 1516 ($C_1C_2BMUN1516$) and hence lacks the C-terminal hydrophobic sequence. DLS experiments showed that, while $C_1C_2BMUNC_2C$ fragment robustly clustered V- and T-liposomes in the absence and presence of Ca^{2+}, the $C_1C_2BMUN1516$

fragment exhibited no clustering ability (Figure 4.5 A). These results show that the C_2C domain is crucial for the membrane bridging activity of the Munc13-1 C-terminal region.

All our previous studies with large Munc13-1 fragments used proteins expressed in Sf9 insect cells. As bacterial expression of the Munc13-1 C_1C_2BMUN fragment ending at 1531 was recently described (Kreutzberger et al., 2017), we prepared new vectors for expression of Munc13-1 C_1C_2BMUNC_2C and C_1C_2BMUN1516 in *E. coli*. Although the expression yields of both new fragments were modest, they were sufficient to obtain milligram quantities. DLS experiments showed that the bacterially expressed C_1C_2BMUNC_2C and C_1C_2BMUN1516 fragments have analogous ability or lack thereof to cluster liposomes as the corresponding fragments expressed in Sf9 cells (Figure 4.5 A). We also measured the ability of these fragments to support fusion between reconstituted V- and T-liposomes in the presence of Munc18-1, NSF and α SNAP using an established assay that simultaneously measures lipid and content mixing (Liu et al., 2016). The C_1C_2BMUNC_2C fragments expressed in Sf9 insect cells and *E. coli* exhibited comparable activities, with slow lipid and content mixing in the absence of Ca^{2+} and fast fusion upon Ca^{2+} influx (Figure 4.5 B). In contrast, the C_1C_2BMUN1516 fragments expressed in Sf9 insect cells and *E. coli* were both inactive, which correlates with the vesicle clustering results and shows the critical importance of the C_2C domain for Munc13-1 to support fusion in these assays. We also note that the C_1C_2BMUN1516 fragments made in Sf9 insect cells and in bacteria exhibited the expected chromatographic behavior in gel filtration, with elution volume a little larger than the C_1C_2BMUNC_2C fragments (16.5 versus 16.2 ml in a Superdex S200 10/300 GL column), and a similar ability to bind to T- liposomes in co-sedimentation assays as C_1C_2BMUNC_2C fragments (Figure 4.6). These results indicate that the

C_1C_2BMUN1516 fragments are properly folded and retain the ability of the C_1-C_2B region to bind to liposomes containing DAG and PIP_2, but cannot bridge these liposomes to V- liposomes because they lack the C_2C domain.

4.3.3 Mutations in putative membrane-binding sites of the C_2C domain impair membrane bridging by C_1C_2BMUNC_2C

We next introduced specific mutations in the C_2C domain that could potentially disrupt the membrane bridging activity of the Munc13-1 C_1C_2BMUNC_2C fragment and could thus help us to test the functional importance of this activity for neurotransmitter release in neurons. Many C2 domains bind phospholipids in a Ca^{2+}-dependent manner through loops that also form the Ca^{2+}-binding sites at the tip of a β- sandwich structure, and these loops contain exposed basic and hydrophobic residues that can bind to negatively charged phospholipids and insert into the bilayer, respectively (Chapman and Davis, 1998, Fernandez-Chacon et al., 2001, Rizo and Sudhof, 1998). In addition, some C_2 domains contain a polybasic region on the side of the β-sandwich that can also contribute to membrane binding (e.g. the synaptotagmin-1 C_2B domain (Li et al., 2006)). Although the Munc13-1 C_2C domain is not expected to bind Ca^{2+}, it could bind lipids in a Ca^{2+}-independent manner through similar sequences. Indeed, models of its three-dimensional structure derived from its homology to C_2 domains of known structure such as the synaptotagmin-1 C_2B domain (Fernandez-Chacon et al., 2001) and the RIM1 C_2B domain (Guan et al., 2007) consistently predicted that the Munc13-1 C_2C domain contains exposed basic and hydrophobic residues in its putative membrane-binding loops, as well as a polybasic region on the side of the β-sandwich. Figure 4.7 A illustrates one of these models, including stick models

for residues that we chose for mutagenesis: one basic and one hydrophobic residue from the putative membrane-binding loops (R1598 and F1658, respectively), and two residues from the polybasic region (K1613 and K1616).

To examine whether these loops and the polybasic region confer membrane binding to the Munc13-1 C_2C domain and hence the membrane bridging activity of $C_1C_2BMUNC_2C$, we prepared bacterially expressed WT and mutant versions of $C_1C_2BMUNC_2C$ bearing single residue substitutions (R1598E and F1658E) or double residue substitutions (R1598E/F1658E and K1613A/K1616A) designed to disrupt C_2C domain-lipid interactions. DLS assays that monitored clustering between V- and T-liposomes revealed that the K1613/K1616 mutation partially disrupts the clustering activity of $C_1C_2BMUNC_2C$ (Figure 4.7 B). The single R1598E and F1658E mutations disrupted vesicle clustering strongly, although the R1598E mutant appeared to retain a slight clustering ability. Clustering was completely abolished by the R1598E/F1658E mutation. These results demonstrate the critical importance of the C_2C domain loops for membrane bridging by the Munc13-1 $C_1C_2BMUNC_2C$ fragment, and show that the C_2C domain polybasic region also contributes to this activity.

The mutations in the C_2C domain are expected to disrupt its interaction with membranes but leave the C_1-C_2B region unaffected, thus allowing binding of $C_1C_2BMUNC_2C$ to liposomes through one end of the molecule. To directly visualize this prediction for the $C_1C_2BMUNC_2C$ R1598E/F1658E mutant, we again used cryo-ET and the same liposome preparations used for WT $C_1C_2BMUNC_2C$. The liposomes appeared generally more disperse in specimens containing the $C_1C_2BMUNC_2C$ R1598E/F1658E mutant (Figure 4.4 F-J) than those containing WT

$C_1C_2BMUNC_2C$ (Figure 4.4 A-E), consistent with the DLS data. It was more difficult to identify $C_1C_2BMUNC_2C$ molecules for the R1598E/F1658E mutant than for the WT protein, which we attribute to the tendency of $C_1C_2BMUNC_2C$ to move to the water-air interface in specimens lacking liposomes and the fact that the R1598E/F1658E mutation disrupts its membrane-bridging activity. Nevertheless, we were able to identify $C_1C_2BMUNC_2C$ R1598E/F1658E mutant molecules, and all of them were bound to a single liposome. In contrast, among 123 molecules of WT $C_1C_2BMUNC_2C$ that we identified, 78 were bridging two liposomes and 45 were bound to a single liposome (25 among these 45 likely did not bridge liposomes due to steric hindrance caused by other $C_1C_2BMUNC_2C$ molecules at the liposome-liposome interface). Hence, these data are fully consistent with the DLS results showing complete abrogation of liposome clustering by the R1598E/F1658E mutation.

To investigate the impact of these mutations on the ability of Munc13-1 $C_1C_2BMUNC_2C$ to support membrane fusion in vitro, we monitored lipid and content mixing between reconstituted V- and T-liposomes in the presence of Munc18-1, NSF and αSNAP. In initial experiments, we used $C_1C_2BMUNC_2C$ fragments at 0.1 μM concentration, which allows better discrimination of the effects of mutations than the standard concentrations we normally used in these assays (0.5 μM) (Xu et al., 2017) and somewhat decreases the activity of the WT $C_1C_2BMUNC_2C$ fragment (Figure 4.8). At this concentration, the K1613A/K1616A mutation considerably impaired fusion, whereas the R1598E, F1658E and R1598E/F1658E mutations completely abolished fusion (Figure 4.8 A). To better characterize the effects of the mutations, we then performed titrations where the mutant $C_1C_2BMUNC_2C$ fragments were added at different concentrations. The K1613A/K1616A mutant was much more active at 0.25 and 0.5

μM concentrations than at 0.1 μM, whereas at 0.75 μM K1613A/K1616A we observed a slightly decreased activity that may arise because of appreciable precipitation (Figure 4.8 B). The R1598E was able to support a small amount of lipid mixing at 0.5-2.5 μM concentrations, whereas the F1658E and R1598E/F1658E supported only very small amounts of lipid mixing at 2.5 μM concentration, and any content mixing supported by these three mutants was close to the noise level (Figure 4.8B). These observations were reproduced in multiple experiments with different liposome preparations and were confirmed by quantification in triplicate experiments with the same preparations of the amounts of lipid and content mixing observed after 500 s of reaction with 0.1 μM WT and K1613A/K1616A mutant, and of the lipid mixing observed after 1000 s for 0.5 μM WT and R1598E, F1658E and R1598E/F1658E mutants (Figure 4.9). Overall, these results show that the F1658E and R1598E/F1658E mutations almost completely abolish the ability of Munc13-1 C_1C_2BMUNC_2C to support membrane fusion, whereas the R1598E mutation causes also a very strong but somewhat milder disruption, and the K1613A/K1616A mutation induces only a moderate impairment, mirroring the liposome clustering data.

4.3.4 The mutations in the C_2C domain disrupt synaptic vesicle docking, priming and release

To examine the functional consequences of the mutations in the Munc13-1 C_2C domain, we turned again to rescue experiments in neuronal autaptic cultures from *Munc13-1/2* DKO mice and compared the release observed upon lentiviral expression of full-length Munc13-1 bearing mutations in the C_2C domain with those observed with the WT rescue. The R1598E, F1658E and R1598E/F1658E mutations severely impaired spontaneous, evoked and sucrose-induced release, and the effects were particularly strong for evoked release, which was almost abolished by the

F1658E and R1598E/F1658E mutations (Figure 4.10 A-F). As a consequence of the stronger impairment of evoked release compared to sucrose- induced release, the three mutations led to decreases in the vesicular release probability (Figure 4.9 G), as observed for the Munc13-1 ΔC_2C mutant (Figure 4.1 F). Correspondingly, the paired-pulsed ratios measured for the three mutants were larger than that observed for WT Munc13-1 (Figure 4.10 H), and all the mutant rescues exhibited facilitation upon repetitive stimulation, in contrast to the slight depression observed in the WT rescue (Figure 4.10 I). The WT and mutant Munc13-1 proteins all exhibited presynaptic localization and were expressed at comparable levels (Figure 4.11), showing that the differences in electrophysiological parameters do not arise from mislocalization or aberrant overexpression. In a separate set of experiments, we analyzed the functional effects of the K1613A/K1616A mutation, using WT Munc13-1 again as positive control. This mutation did not impair spontaneous release but led to a moderate decrease in evoked release, and also appeared to decrease the RRP but the difference to WT was not statistically significant (Figure 4.12 A-F). There was also no significant difference in the vesicular release probability and the paired-pulse ratios measured for rescue with WT and K1613A/K1616A mutant Munc13-1 (Figure 4.12 G,H), although the K1613A/K1616A mutant displayed a milder depression upon repetitive stimulation than WT Munc13-1 (Figure 4.12 I).

These results show that the ability of these various mutations in the Munc13-1 C_2C domain to impair liposome clustering and fusion in vitro correlates well with the functional effects of these mutations on synaptic vesicle priming and Ca^{2+}-triggered neurotransmitter release in neurons. We also tested whether overexpression of the four Munc13-1 mutants in neurons from WT mice yielded differences in spontaneous, evoked and sucrose-induced release

with respect to overexpression of WT Munc13-1, but we did not observe any significant differences that would suggest a dominant negative effect of the mutant fragments (Figure 4.13).

Previous studies that used high-pressure freezing/freeze substitution of organotypic hippocampal slice cultures and electron tomography showed that synaptic vesicle docking is strongly impaired in *Munc13-1/2* DKO neurons, defining docking as vesicles that appear to be in direct contact with presynaptic active zone membranes (Imig et al., 2014). Here we used an analogous approach to study the impact of the four Munc13-1 point mutations on the ability of Munc13-1 to support synaptic vesicle docking. In this analysis, we also included the Munc13-1 ΔC_2C mutant. Significant defects in docking were observed for all Munc13-1 mutants, with the R1598E/F1658E mutation having the strongest effect and the K1613E/K161E mutation the mildest (Figure 4.14 A,B). A plot of the normalized number of docked synaptic vesicles observed for the WT and mutant Munc13-1 fragments against the RRP charge shows a strong correlation (Figure 4.14 C), supporting the notion that docking and priming are closely related. Overall, these results demonstrate the critical importance of the Munc13-1 C_2C domain for synaptic vesicle docking, priming and, particularly, Ca^{2+}-triggered neurotransmitter release. Moreover, the correlation between the physiological effects caused by the mutations and those caused on liposome clustering and membrane fusion provide strong evidence that the ability of Munc13-1 to bridge membranes is crucial for neurotransmitter release.

4.4 Discussion

Great advances have been recently made in understanding the mechanism of neurotransmitter release, including the fundamental concept that Munc18-1 and Munc13s orchestrate SNARE complex assembly in an NSF-SNAP-resistant manner (Ma et al., 2013) that explains at least in part the total abrogation of neurotransmitter release observed in the absence of Munc18-1 or Munc13s (Richmond et al., 1999, Varoqueaux et al., 2002, Verhage et al., 2000). Nevertheless, the actual pathway of SNARE complex assembly is still under intense investigation. The critical role of Munc13s in this process has generally been associated to the activity of its MUN domain in facilitating opening of syntaxin-1 (Ma et al., 2011, Richmond et al., 2001, Wang et al., 2017, Yang et al., 2015), but this activity alone does not account for the functional importance of the Munc13 C_2C domain, which was suggested by diverse studies (Liu et al., 2016, Madison et al., 2005, Stevens et al., 2005) and is further supported here (Figure 4.1). An attractive model that assigned a critical function to the C_2C domain postulated that Munc13-1 can bridge the synaptic vesicle and plasma membranes through interactions involving the C_2C domain and the C_1-C_2B region, respectively (Figure 4.2). However, the physiological relevance of this model had not been examined. Here we provide compelling evidence that the highly conserved C-terminal region of Munc13-1 can indeed bridge two membranes, that the C_2C domain is critical for this activity, and that membrane bridging is a key aspect of the function of Munc13-1 in synaptic vesicle docking, priming and fusion. The importance of this bridging function is emphasized by the finding that a single point mutation in this 200 kDa protein abolishes neurotransmitter release almost completely.

This dramatic result suggests that membrane bridging may in fact constitute the primary function of Munc13s, although this notion does not diminish the importance of their role in opening syntaxin-1 and the two activities are likely coupled. Formation of SNARE complexes is hindered not only by the closed conformation of syntaxin-1 (Dulubova et al., 1999) but also by the furled conformation of a Munc18-1 loop that prevents synaptobrevin binding and hence hinders the SNARE complex templating function of Munc18-1 (Sitarska et al., 2017). The bridge between the synaptic vesicle and plasma membranes provided by Munc13-1 (Figure 1 – figure supplement 1) is expected to dramatically increase the number of productive encounters between synaptobrevin and the syntaxin-1-Munc18-1 complex to initiate SNARE complex formation (Xu et al., 2017), further facilitated by the activity of the Munc13-1 MUN domain in opening syntaxin-1 (Ma et al., 2011, Wang et al., 2017, Yang et al., 2015). Note also that a membrane bridging function for Munc13s is not surprising given the homology of their MUN domain with tethering factors from different membrane comparments (Pei et al., 2009, Yu and Hughson, 2010).However, these factors normally do not contain C_1 or C_2 domains. The incorporation of membrane- binding C_1 and C_2 domains at both ends of the Munc13 MUN domain may have occurred during evolution to provide opportunities for regulation of this membrane-bridging activity, as exquisite regulation is a hallmark of neurotransmitter release and Munc13-1 acts as a master regulator of this process (Rizo, 2018). The C_1 and C_2B domains of Munc13s are involved in DAG-phorbol ester-dependent potentiation of release (Basu et al., 2007, Rhee et al., 2002) and Ca^{2+}-PIP_2-dependent short-term plasticity (Shin et al., 2010), respectively. The C_2C domain is not known to be involved in plasticity, but it is tempting to speculate that as yet unidentified

mechanisms (e.g. phosphorylation) may modulate C_2C domain activity to regulate neurotransmitter release.

The finding that the mutations in the Munc13-1 C_2C domain described here impair synaptic vesicle docking, priming and release (Figs. 4.1, 4.10, 4.12, 4.14), in correlation with the impairments they cause in liposome clustering and fusion in vitro (Figs. 4.7, 4.8), suggests that the membrane-bridging activity of the Munc13 C-terminal region is important for more than one of the steps that lead to release. The role in docking-priming is not unexpected, as SNARE complex assembly is believed to be necessary for vesicle docking using the definition that has become widely used recently and we adopt here, i.e. contact between the vesicle and plasma membranes (Imig et al., 2014)(note that, with this definition, docking and priming may constitute the same event, although this equivalence is not fully established (Rizo, 2018)). Moreover, the phenotypic spectra in Munc13-1 mutants and in syntaxin-1 titration experiments are highly similar (Arancillo et al., 2013), supporting the hypothesis that Munc13-1 membrane bridging and SNARE complex assembly are tightly linked. Note however that, *in vivo*, synaptic vesicles are believed to be tethered to the active zone through other mechanisms, for instance through RIM-Rab3 interactions, and Munc13 function may be partially redundant with that of CAPS, which contains a MUN domain and membrane-binding domains and also supports SNARE-dependent fusion in reconstitution assays (James et al., 2009) (reviewed in Rizo and Sudhof, 2012). Such redundancy may explain the finding that the effects of the Munc13-1 C_2C domain mutations on the liposome clustering and fusion assays in vitro (Figs. 4.7, 4.8) are stronger than those observed in vesicle docking and priming in neurons (Figs. 4.1 ,4.10 ,4.12 ,4.14).

Interestingly, the Munc13-1 C_2C mutations also disrupt Ca^{2+}-triggered neurotransmitter release at least as much as they impair docking and priming. In particular, evoked release is almost abolished by the F1658E and R1598E/F1658E mutations (Figure 4.10 E), which correlates with the finding that these mutations abolish liposome clustering and fusion in vitro (Figs. 4.7, 4.8). These observations suggest that the membrane bridging activity of Munc13-1 is as important for release itself as for vesicle docking-priming. Hence, it seems likely that Munc13-1 still bridges the vesicle and plasma membranes after SNARE complex formation and contributes to controlling the probability of Ca^{2+}-triggered synaptic vesicle fusion. It is also plausible that the C_2C domain mutations impair only SNARE complex assembly and a lower number of assembled SNARE complexes results in a stronger impairment of Ca^{2+}-triggered fusion than of sucrose-induced release or the number of docked vesicles. Both explanations are not mutually exclusive, but the notion that Munc13-1 still bridges the primed vesicles to the plasma membrane, forming part of the macromolecular assembly that triggers fusion, is attractive because it can explain the multiple and distinct effects of Munc13-1 mutations on vesicular release probability (Basu et al., 2007, Junge et al., 2004, Shin et al., 2010, Xu et al., 2017). In particular, the finding that phorbol ester stimulation of Munc13-1 C_1 domains acutely increases release probability without changing the number of docked and primed vesicles (Basu et al., 2007, Camacho et al., 2017) strongly suggests that modulation of the Munc13 bridging function may directly regulate the efficiency of the vesicle fusion reaction. This model is also consistent with recent super-resolution imaging data showing that mammalian Munc13-1 and invertebrate Unc13 form supramolecular assemblies that appear to define the sites for

neurotransmitter release in the presynaptic terminal (Reddy-Alla et al., 2017, Sakamoto et al., 2018).

It is worth noting that the Munc13-1 C-terminal region can likely bridge two membranes in at least two different orientations that can favor SNARE complex formation and/or fusion to different extents, or can also inhibit these events, thus acting as a 'gatekeeper' of release. This notion emerged from the finding that the C_1 and C_2B domains have their respective DAG- and Ca^{2+}-PIP_2-binding sites next to each other and can thus cooperate in binding to the plasma membrane in a defined, slanted orientation, but these domains also form a polybasic region that can bind to membranes in a different orientation, more perpendicular to the membrane (Xu et al., 2017). This model provides a basis to understand DAG- and Ca^{2+}-dependent presynaptic plasticity that depends on Munc13, and explains the observation that membrane fusion does not occur or is very slow in the absence of Ca^{2+} even though Munc13-1 $C_1C_2BMUNC_2C$ bridges membranes under these conditions (Figure 4.4), whereas fusion is fast upon Ca^{2+}-binding to the Munc13-1 C_2B domain (Liu et al., 2016) (e.g. Figs. 4.5 B, 4.8 A). Mutagenesis studies of *C. elegans* Unc13 support the idea that Unc13 can exist in two states, one that inhibits release and another that activates release and is favored by Ca^{2+}-binding to the C_2B domain (Michelassi et al., 2017). Our cryo-ET images, which were acquired in the absence of Ca^{2+}, show that Munc13-1 $C_1C_2BMUNC_2C$ can bridge two membranes in a range of orientations, some of which would prevent the membranes from coming closer while others could favor initiation of SNARE complex assembly. We previously proposed that Ca^{2+}, DAG and PIP_2 favor more slanted orientations that can facilitate SNARE complex formation more efficiently and/or membrane

fusion (Xu et al., 2017). Extensive studies varying these different factors under conditions that prevent membrane fusion will be required to test this proposal.

Further research will also be required to investigate how the membrane-bridging activity of Munc13-1 is coupled to other functions, such as its role in opening syntaxin-1. In this context, our NMR data suggest that the C_2C domain does not contribute to syntaxin-1 binding (Figure 4.3 C-E), but weak interactions of the MUN domain with syntaxin-1 are believed to be critical to overcome the energy barrier to open its conformation (Ma et al., 2011, Wang et al., 2017). In addition, Munc13 has been shown to increase the fidelity of SNARE complex assembly by decreasing the number of SNARE complexes that are formed in an antiparallel orientation (Lai et al., 2017), indicating that there are additional interactions of Munc13 with the SNAREs that are functionally important. Such interactions may be reminiscent of those found between tethering factors homologous to the Munc13 MUN domain and their cognate SNAREs (Yu and Hughson, 2010). It is not surprising that a large, highly conserved component of the release machinery such as Munc13-1 has multiple important roles. It appears that much is currently known, but there is still much to learn.

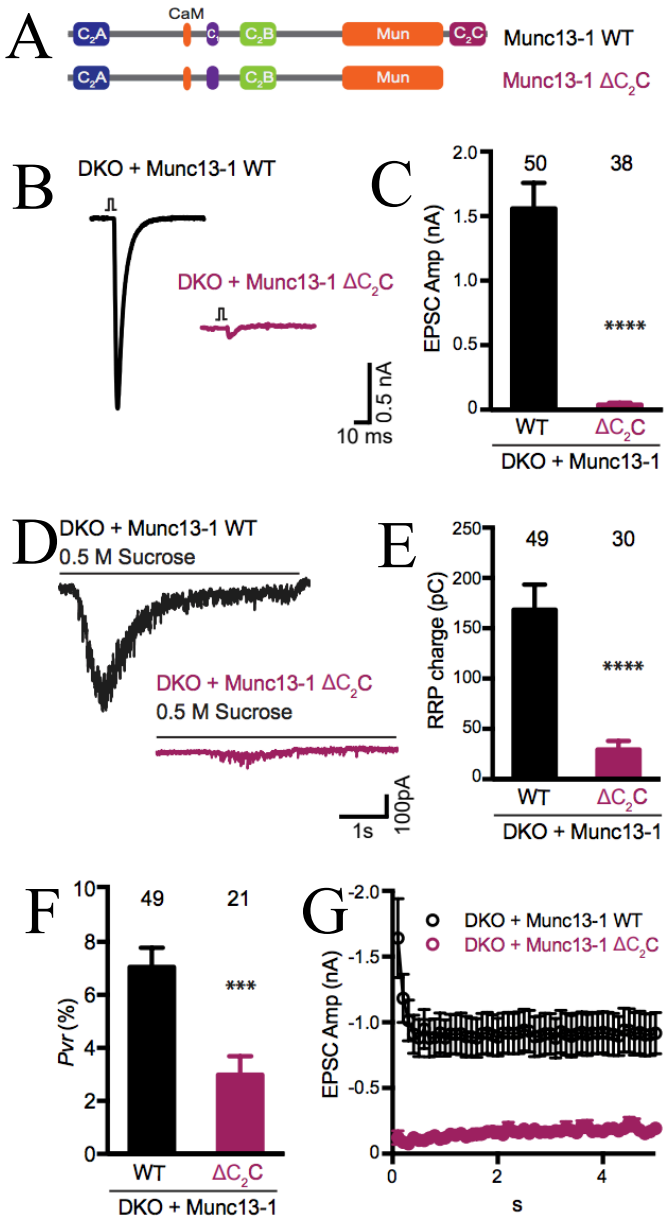

Figure 4.1 Functional effects caused by deleting the Munc13-1 C_2C domain
(A) Cartoon depicting the domain structure of Munc13-1 and Munc13-1ΔC_2C. (B) Example EPSC traces recorded from Munc13-1/2 DKO autaptic hippocampal neurons expressing either Munc13-1 WT (black) or Munc13-1ΔC_2C (Bourgogne red). (C) Plot showing the average EPSC amplitudes obtained from the DKO neurons rescued with Munc13-1 WT or Munc13-1ΔC_2C. (D) Example traces of synaptic current responses induced by 5 s application of 500 mM sucrose from DKO neurons rescued with the WT and the C_2C truncated mutant indicated above. (E) Plot of the average RRP charge for both groups. (F) Plot of the calculated P_{vr} in % for Munc13-1 WT and C_2C truncated mutant. (G) Graph showing the absolute EPSC amplitudes in response to a train of 50 action potentials (APs) with an inter-stimulus interval (ISI) of 100 ms (10Hz) for the WT and truncated C_2C domain mutant. Numbers at the top of the bars represent n values of each group. All data are mean ± SEM. Significance and p values were determined by Mann Whitney test. ****p< 0.0001: ***p<0.001. Data collected by Marcial Camacho.

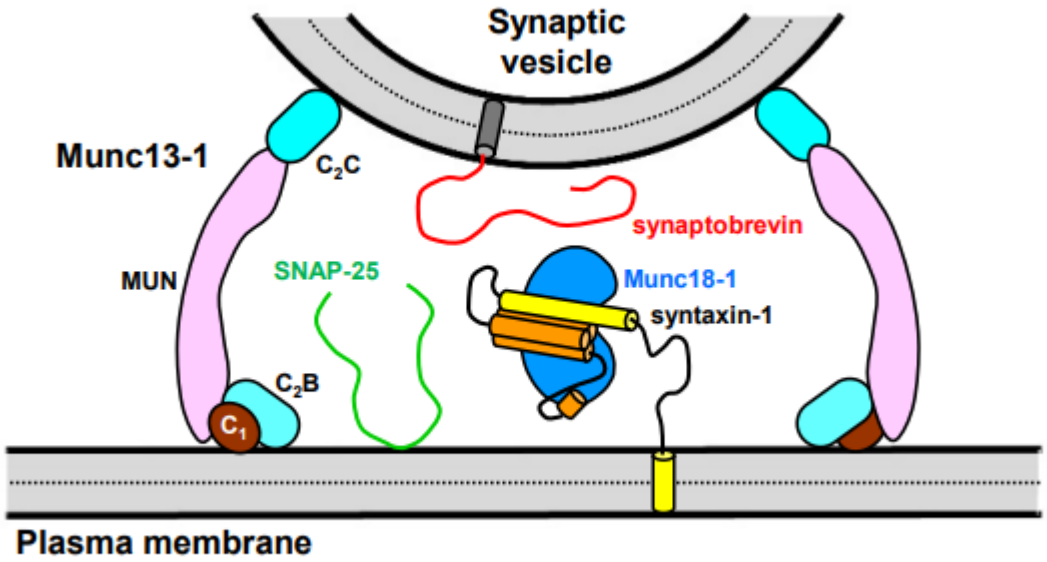

Figure 4.2 Model illustrating how the Munc13-1 C-terminal region can bridge the synaptic vesicle and plasma membranes

The different domains of the Munc13-1 C-terminal region are colored in brown (C_1), cyan (C_2B), pink (MUN), and blue (C_2C). The diagram also shows other components of the release machinery in the state postulated to exist before SNARE complex assembly, with Munc18-1 (blue) bound to syntaxin-1 folded in a closed conformation (yellow and orange), and SNAP-25 (green) and synaptobrevin (red) unstructured.

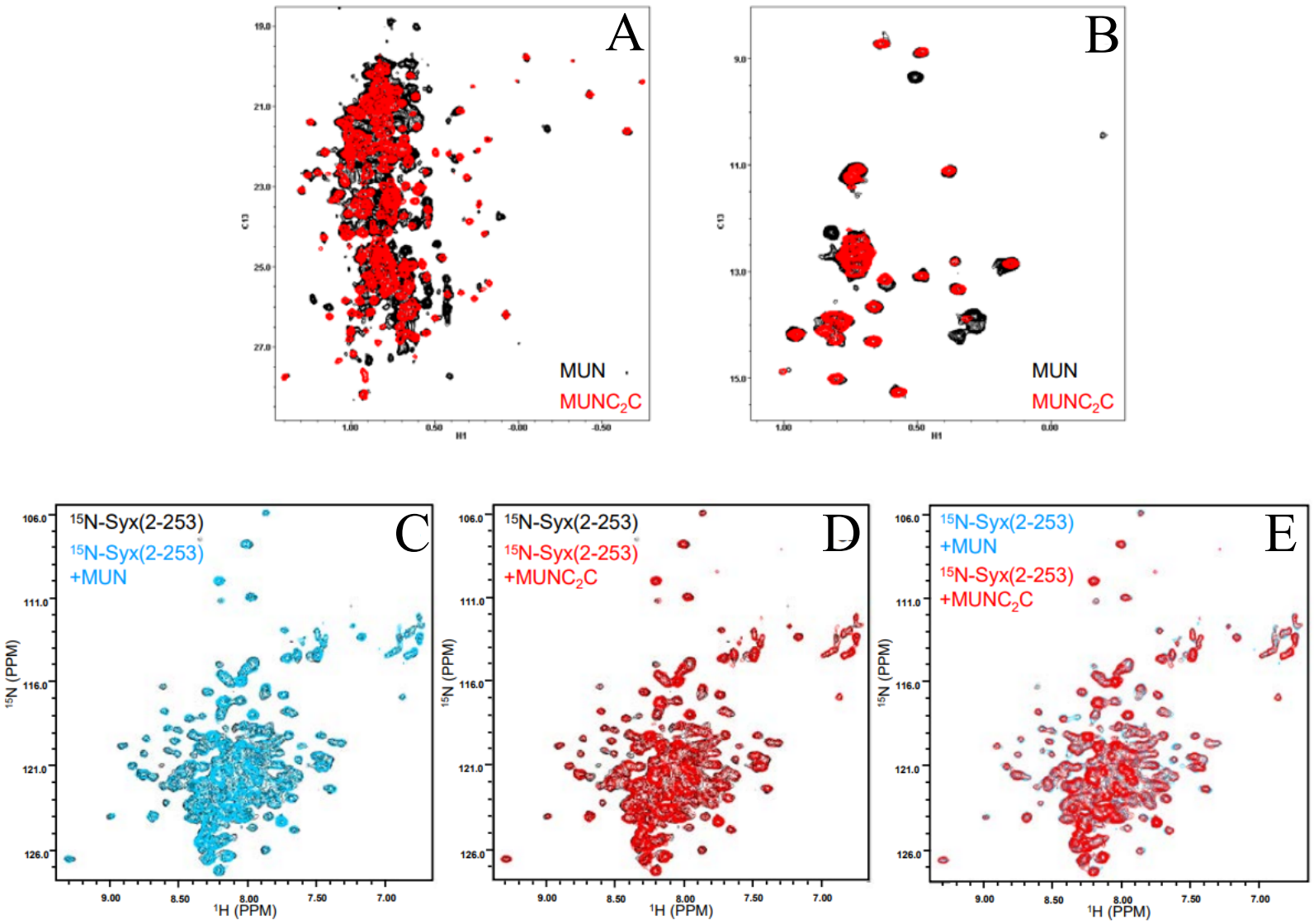

Figure 4.3 NMR analysis of the Munc13-1 MUNC$_2$C fragment and binding to syntaxin-1
(A,B) ^{1}H-^{13}C HMQC spectra of perdeuterated, ^{1}H,^{13}CH$_3$-ILV-labeled samples of the Munc13-1 MUN domain (red countours) and MunC$_2$C (black contours). Note that spectrum of the MUNC$_2$C domain contains additional cross-peaks that appear in well-resolved regions and show that the C$_2$C domain is structured, and that some of the cross-peaks of the MUN domain shift, indicating that it packs against the C$_2$C domain. (C-E) ^{1}H-^{15}N HSQC spectra of ^{15}N-labeled syntaxin-1 2-253 (black contours) in the absence or presence of Munc13-1 MUN domain and the MUNC$_2$C fragment. There is only slight broadening of the syntaxin-1 2-253 cross-peaks (C,D), resulting in very similar spectra (E). Data in panels A and B collected by Wei Li.

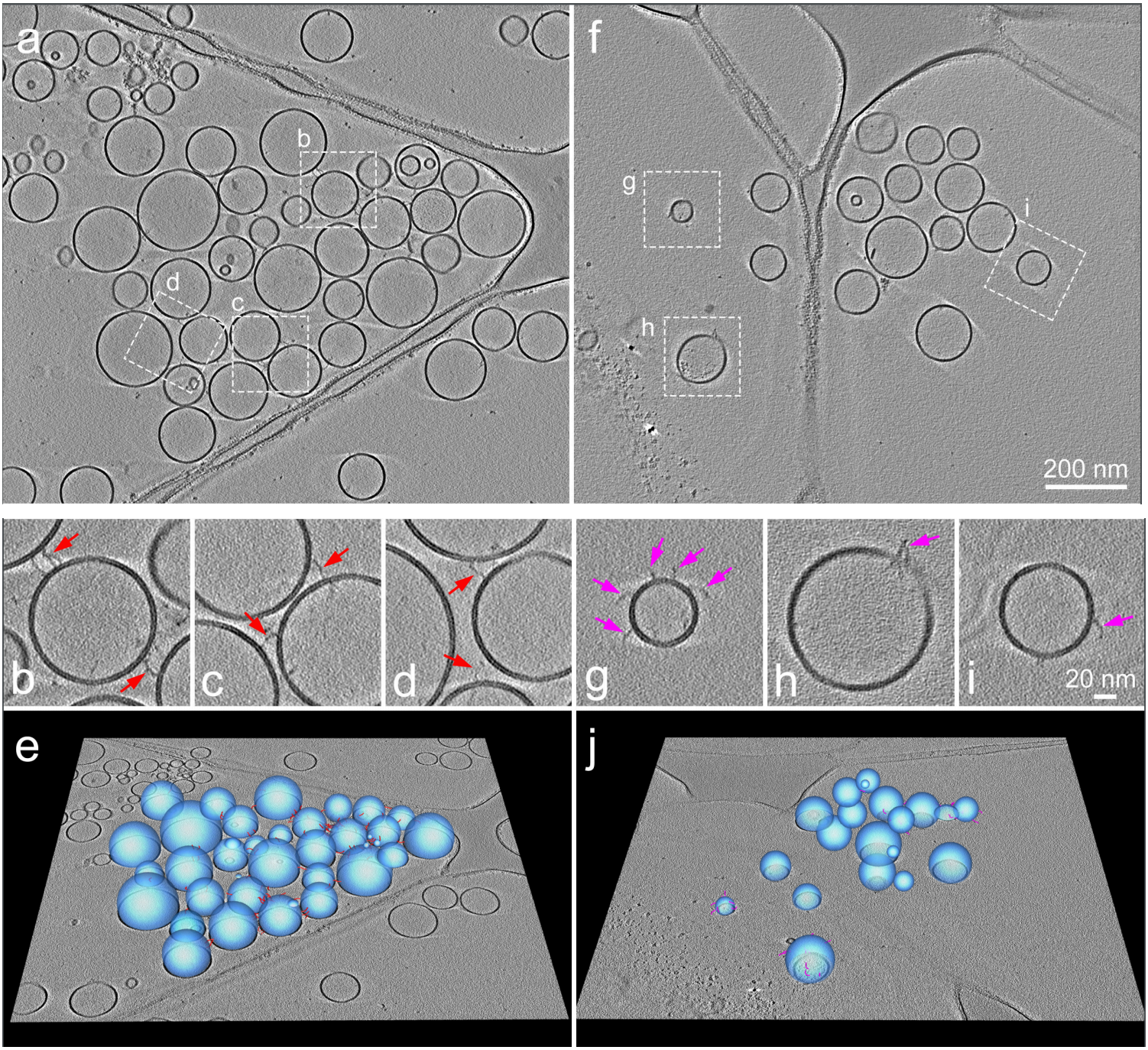

Figure 4.4 Cryo-ET reconstructions showing that Munc13-1 C_1C_2BMUNC_2C can bridge two membranes
Specimens were prepared following our standard protocol to analyze lipid and content mixing between V- and T-liposomes in the presence of Munc18-1, NSF, α-SNAP, 0.1 μM EGTA, and either WT (a-e) or R1598E,F1658E mutant (f-j) Munc13-1 C_1C_2BMUNC_2C (see methods). (a,f) Tomographic slices provide an overview of the reaction mixtures including WT (a) or R1598E,F1658E mutant (f) Munc13-1 C_1C_2BMUNC_2C. (b-d,g-l) Zoom-in of the regions outlined in (a) and (f), respectively. However, note that the tomographic slices may vary slightly in z-height to optimize the visualization of the elongated densities corresponding to Munc13-1 C_1C_2BMUNC_2C. The majority of elongated densities of the WT protein bridge two liposomes (red arrows in b-d), whereas the elongated densities of the R1598E,F1658E mutant protein are bound to a single liposome (pink arrows in g-i). (e,j) 3d graphical models of the tomographic reconstructions show the vesicles (blue) and elongated densities of WT (red) and R1598E,F1658E mutant (pink) Munc13-1 C_1C_2BMUNC_2C in 3D. Data collected by Xiaowei Zhao.

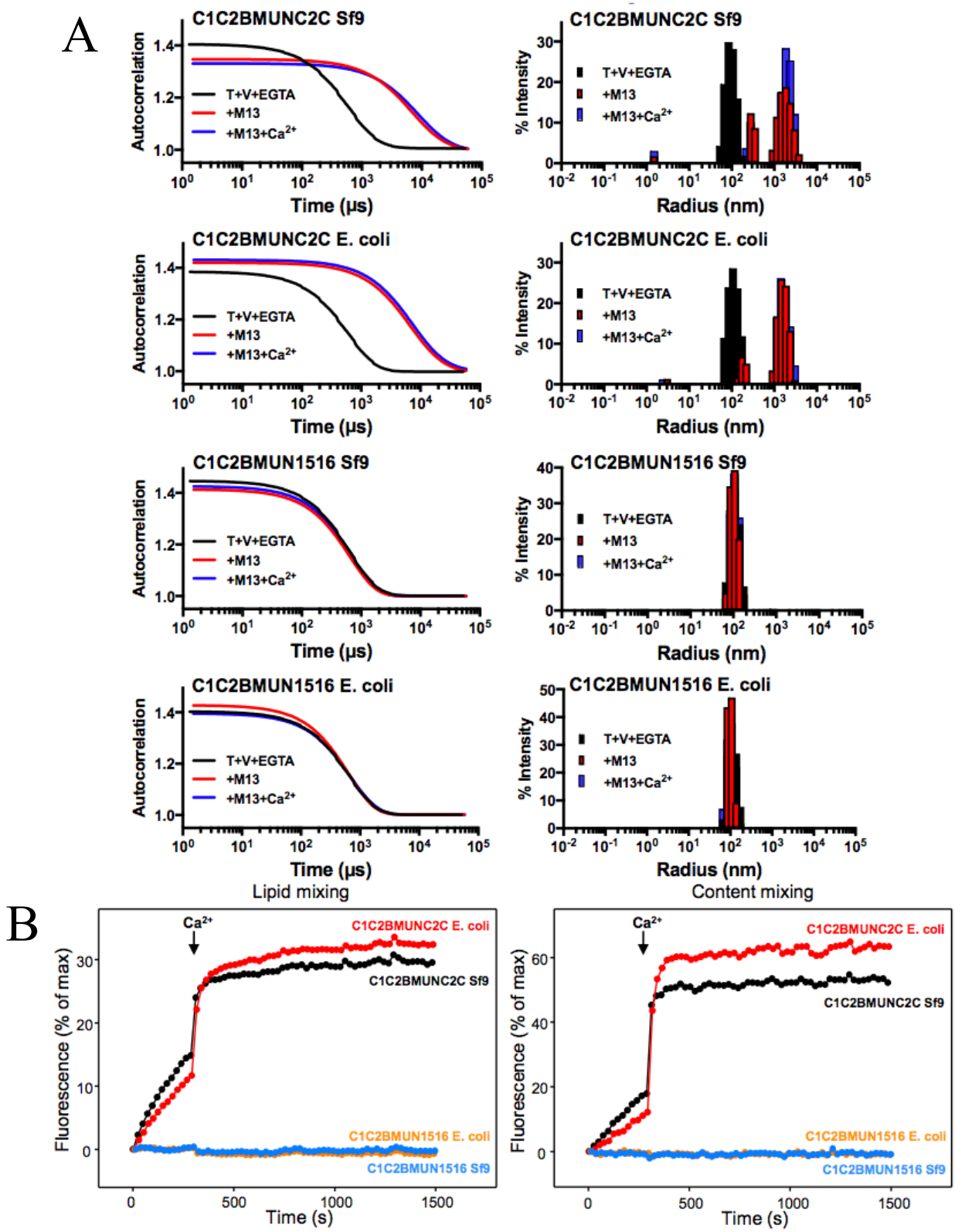

Figure 4.5 The Munc13-1 C_2C domain is required for membrane bridging by the Munc13-1 C-terminal region
(A) DLS analysis of the ability of the Munc13-1 C_1C_2BMUNC_2C or C_1C_2BMUN1516 fragments expressed in Sf9 or *E. coli* to cluster V- and T-liposomes. The diagrams on the left show the autocorrelation curves observed for a mixture of the V- and T-liposomes alone (black) or in the presence of the indicated Munc13-1 fragment and 0.1 mM EGTA (red) or 0.5 mM Ca^{2+} (blue). The diagrams on the right show the particle size distributions corresponding to these curves, with the same color coding. (B) The C_2C domain is required for the ability of the Munc13-1 C-terminal region to support liposome fusion in a reconstituted assay. Lipid mixing (left) between V- and T-liposomes was measured from the fluorescence de-quenching of Marina Blue-labeled lipids and content mixing (right) was monitored from the development of FRET between PhycoE-Biotin trapped in the T-liposomes and Cy5-Streptavidin trapped in the V-liposomes. The assays were performed in the presence of Munc18-1, NSF, α-SNAP and the indicated Munc13-1 fragments. Experiments were started in the presence of 100 µM EGTA and 5 µM streptavidin, and Ca^{2+} (600 µM) was added after 300 seconds.

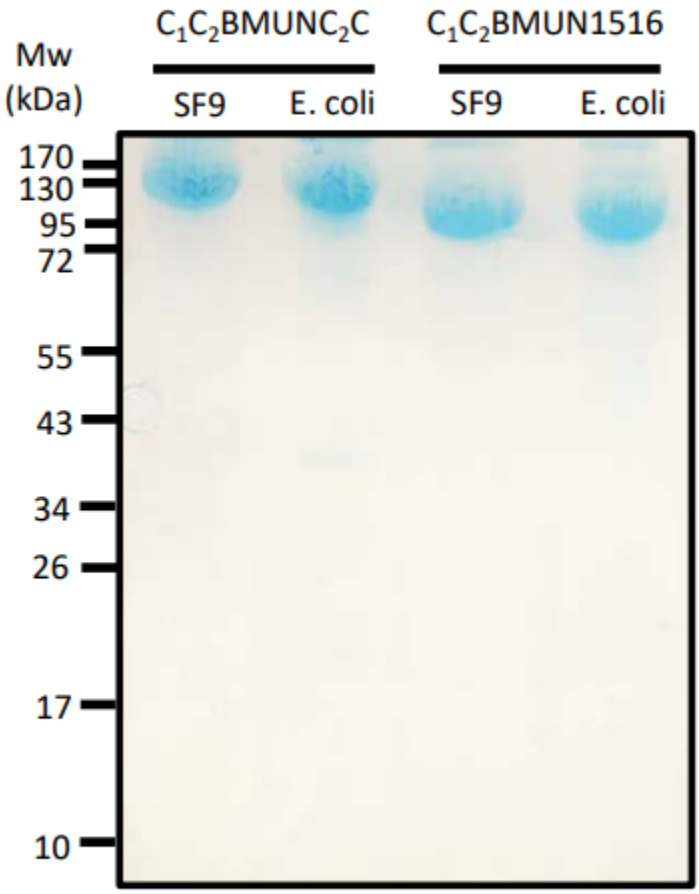

Figure 4.6 The C_1C_2BMUN1516 fragments bind to T-liposomes
Liposome co-sedimentation assays were performed with Munc13-1 C_1C_2BMUNC_2C and C_1C_2BMUN1516 fragments expressed in Sf9 and *E. coli*, and the pellets were analyzed by SDS-PAGE followed by Coomassie blue staining. The positions of the molecular weight markers are indicated on the left.

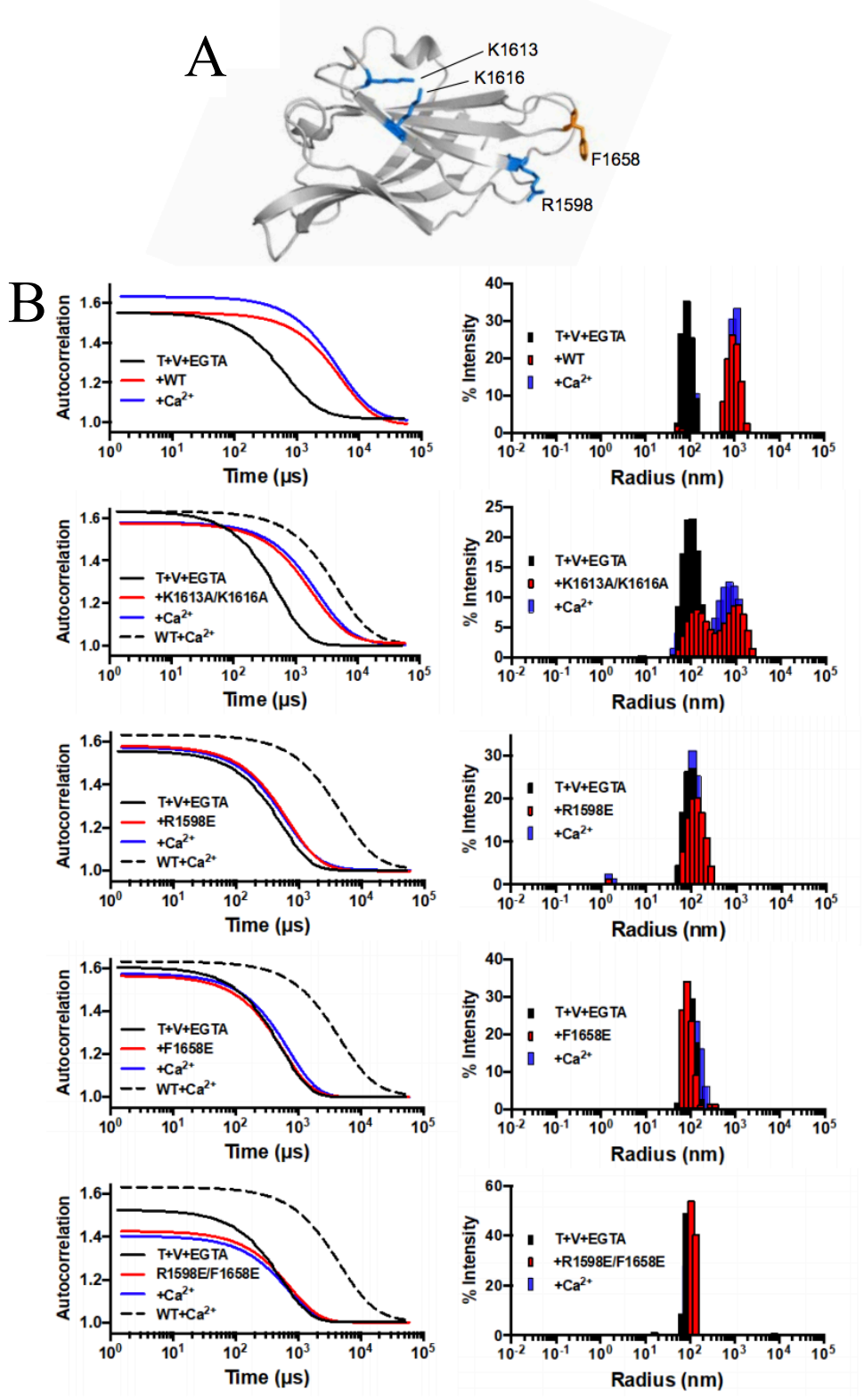

Figure 4.7 Mutations in the putative membrane-binding sites of the Munc13-1 C_2C domain disrupt the membrane-bridging activity of the Munc13-1 C-terminal region

(A) Ribbon diagram of a structural model of the Munc13-1 C_2C domain built based on the crystal structure of the RIM1 C_2B domain (Fernandez, 2001) (PDB ID 2Q3X) and the sequence homology between the two C_2 domains. The Side chains of the residues that were mutated in this study are shown as stick models. (B) DLS analysis of the ability of WT and mutant Munc13-1 $C_1C_2BMUNC_2C$ fragments to cluster V- and T-liposomes. The plots on the left show autocorrelation curves observes for a mixture of the V- and T-liposomes alone (black) or in the presence of the indicated Munc13-1 fragment and 0.1 mM EGTA (red) or 0.6 mM Ca^{2+} (blue). In the plots corresponding to the mutants, the data obtained with WT $C_1C_2BMUNC_2C$ in the presence of Ca^{2+} are shown by the dashed curves for comparison. The diagrams on the right show the particle size distributions corresponding to these curves with the same color coding.

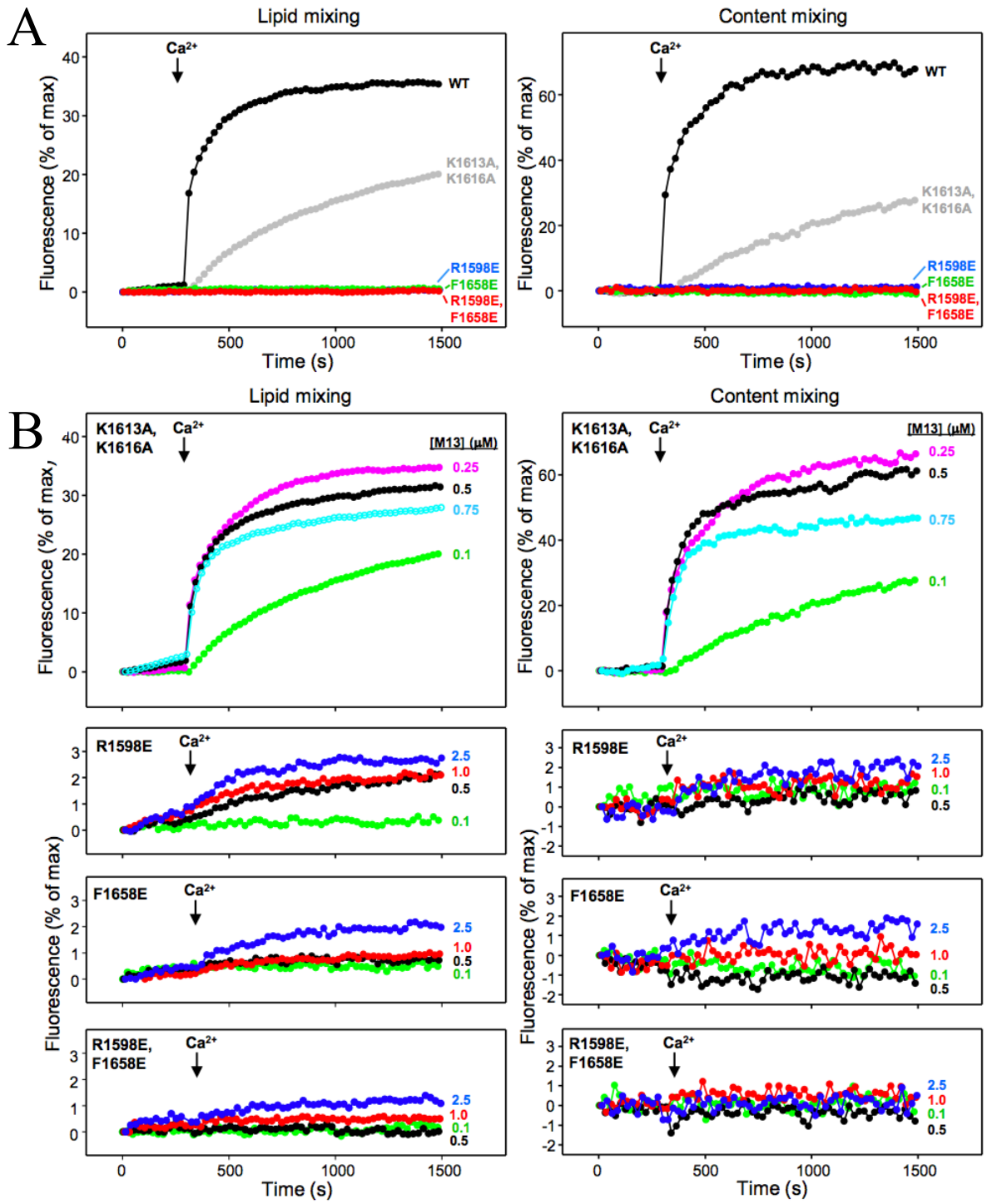

Figure 4.8 Mutations in the putative membrane-binding sites of the Munc13-1 C_2C domain disrupt the ability of the Munc13-1 C-terminal region to support liposome fusion in a reconstituted assay

(A) Lipid mixing (left) between V- and T-liposomes was measured from the fluorescence de-quenching of Marina Blue-labeled lipids and content mixing (right) was monitored from the development of FRET between PhycoE-Biotin trapped in the T-liposomes and Cy5-Streptavidin trapped in the V-liposomes. The assays were performed in the presence of Munc18-1, NSF, α-SNAP and 0.1 μM concentrations of WT or mutant Munc13-1 fragments, as indicated by the color codes. Experiments were started in the presence of 100 μM EGTA and 5 μM streptavidin, and Ca^{2+} (600 μM) was added after 300 seconds. (B) Analogous lipid and content mixing assays performed with different concentrations of mutant Munc13-1 $C_1C_2BMUNC_2C$ fragments as indicated. Note that the scale of the y axis was expanded in the lower plots to help to visualize the small amounts of lipid and content mixing observed.

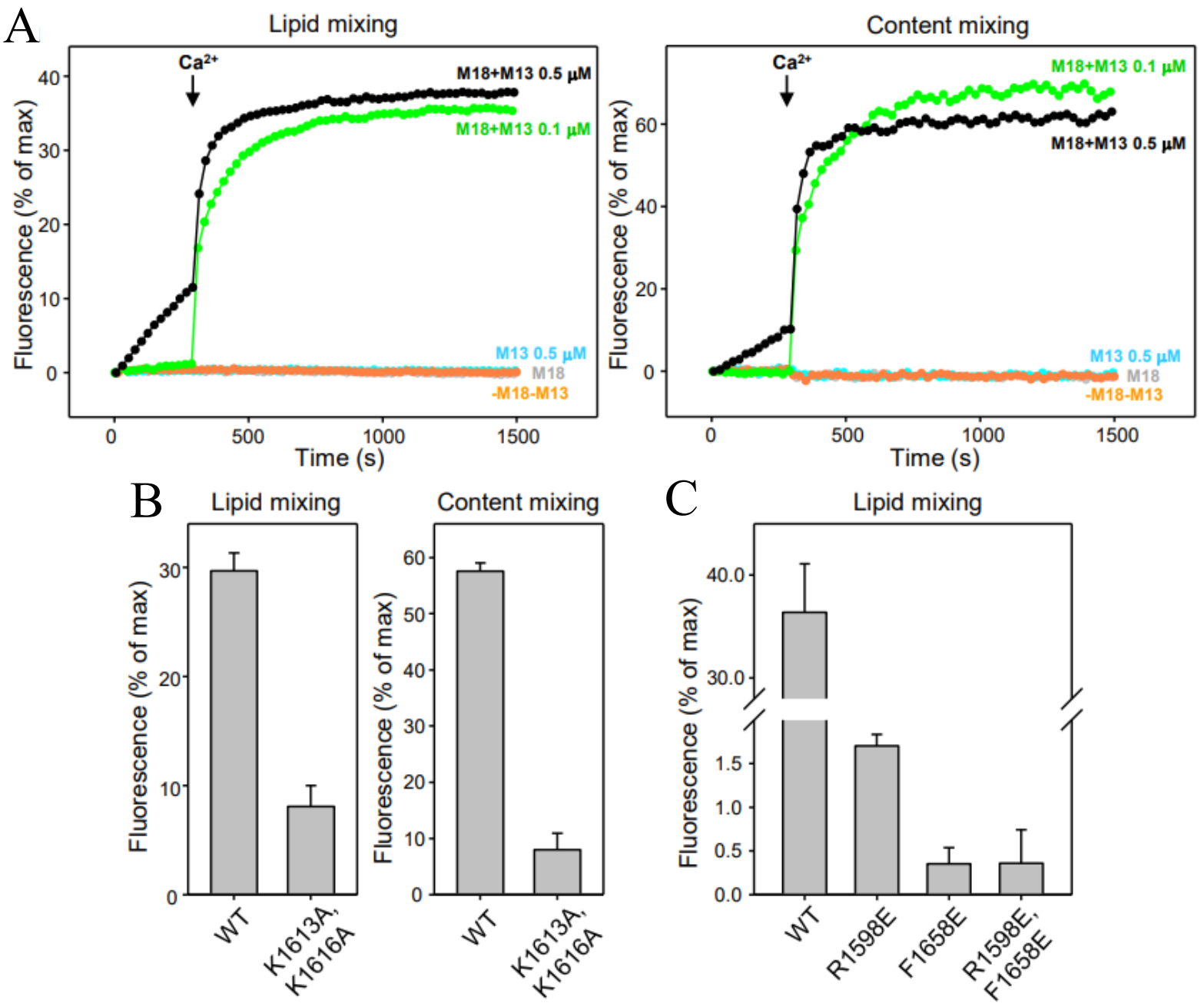

Figure 4.9 Mutations in putative membrane-binding sites of the Munc13-1 C_2C domain disrupt the ability of the Munc13-1 C-terminal region to support liposome fusion in a reconstituted assay

(A) Lipid mixing (left) between V- and T-liposomes was measured from the fluorescence dequenching of Marina Blue-labeled lipids and content mixing (right) was monitored from the development of FRET between PhycoE-Biotin trapped in the T-liposomes and Cy5-Streptavidin trapped in the V-liposomes. The assays were performed in the presence of NSF and α-SNAP with or without Munc18-1 (M18) and without or with WT Munc13-1 $C_1C_2BMUNC_2C$ fragment (M13) at 0.1 or 0.5 µM concentration. Experiments were started in the presence of 100 µM EGTA and 5 µM streptavidin, and Ca^{2+} (600 µM) was added after 300 seconds. The control experiments with Munc18-1 and Munc13-1 (M18), with 0.5 µM Munc13-1 $C_1C_2BMUNC_2C$ and no Munc18-1 (M13 0.5 µM), or without Munc18-1 and Munc13-1 (-M18-M13) illustrate the strict requirement for both proteins to observe liposome fusion in these assays. (B) Quantification of the lipid and content mixing observed after 500 seconds in reconstitution assays performed with 0.1 µM WT or K1613A/K1616A mutant Munc13-1 $C_1C_2BMUNC_2C$ fragment as in 5a. (C) Quantification of the lipid mixing observed after 1000 seconds in reconstitution assays performed with 0.5 µM WT or R1598E, F1658E, R1598E/F1658E mutant Munc13-1 $C_1C_2BMUNC_2C$ fragments as in Fix 5B. In (B,C) bars represent averages of the normalized fluorescence observed after 500 seconds (200 seconds after Ca^{2+} addition) in experimented performed at least in triplicate. Error bars represent standard deviations.

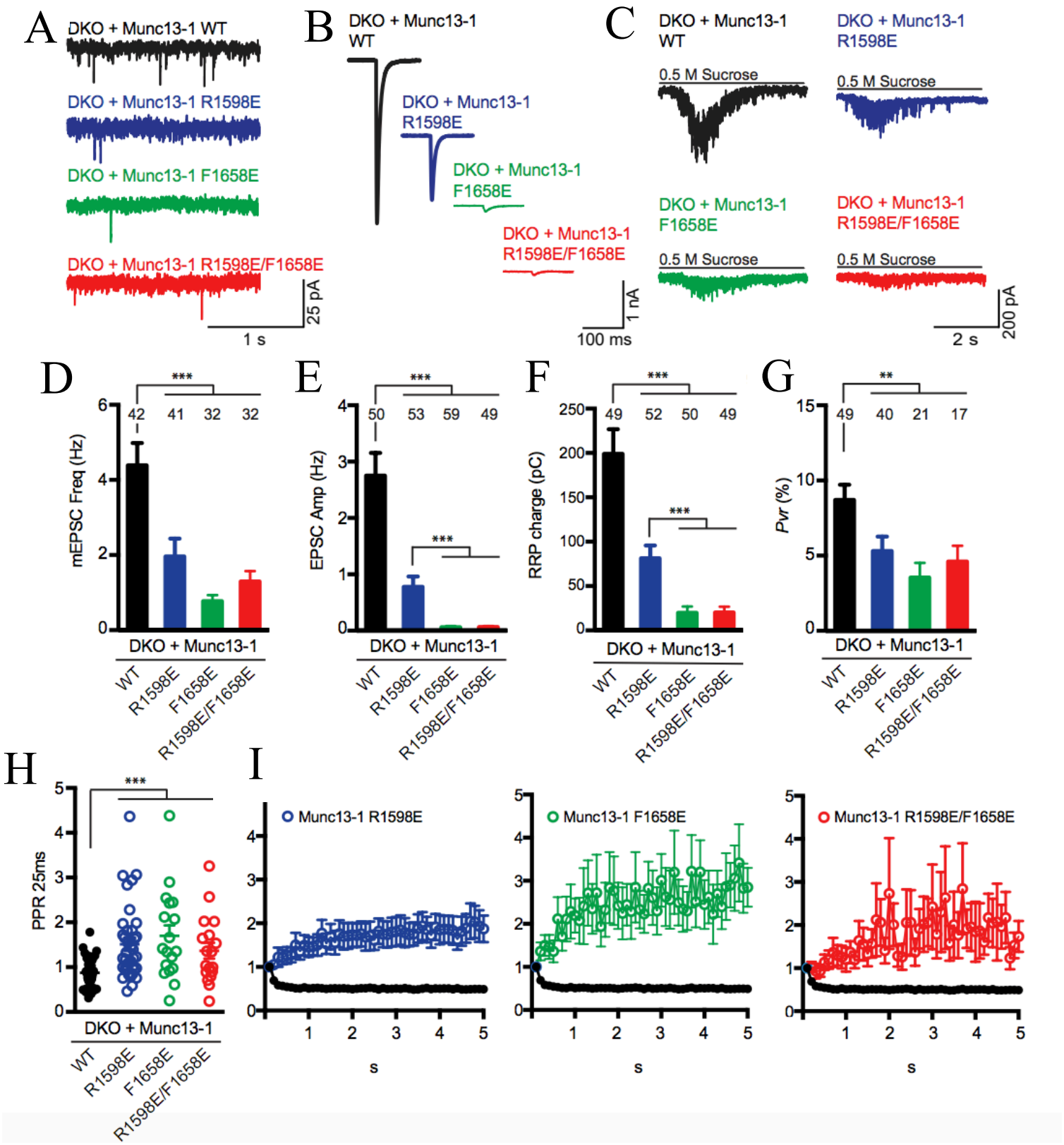

Figure 4.10 Electrophysiological analysis of the functional effects of mutations in the putative membrane-binding loops of the Munc13-1 C_2C domain

(A-C) Representative mEPSCs (A), EPSCs (B), and postsynaptic currents evoked by 0.5 M sucrose (C) in *Munc13-1/2* DKO neurons expressing WT (black), R1598E mutant (blue), F1658E mutant (green), or R1598E/F1658E mutant (red) Munc13-1. (D-G) Mean mEPSC frequencies (D), EPSC amplitudes (E), RRP (F), and P_{vr} (G), measured in the *Munc13-1/2* DKO neuons rescued with WT Munc13-1 and the indicated Mucn13-1 mutants. (H) Paired-pulse ratios of *Munc13-1/2* DKO neurons rescues with the WT Munc13-1 and the indicated Munc13-1 mutants. (I) Normalized EPSC amplitudes in response to a 10 Hz AP train in Munc13-1 DKO neurons rescues with WT (black), R1598E mutant (blue), F1658E mutant (green), or R1598E/F1658E mutant (red) Munc13-1. Numbers above the bars respresent *n* values of each group. All data are mean ± SEM. Significace and p values were determined by Kruskal Wallis test follow by a multiple comparison. *p< 0.05, **p<0.01; *** p<0.001. Data collected by Marcial Camacho.

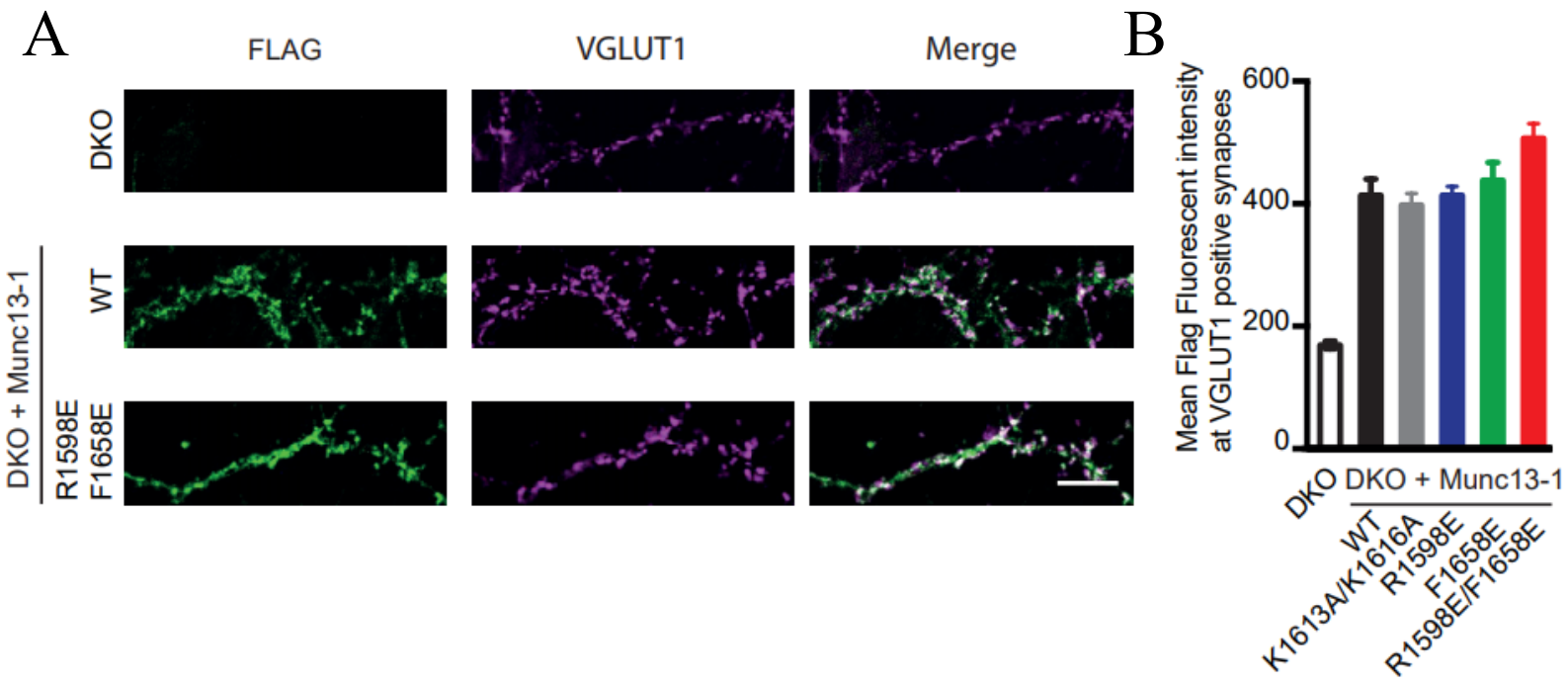

Figure 4.11 Localization and expression levels of WT Munc13-1 and Munc13-1 mutants in rescue experiments
(A) Representative images of *Munc13-1/2* DKO and *Munc13-1/2* DKO hippocampal neurons rescued with FLAG-tagged Munc13-1 WT or Munc13-1 R1598E/F1658E double point mutant, showing synaptic structures with the double labeling for FLAG and the glutamatergic presynaptic marker VGLUT1. Each column of images shows the labeling of FLAG in green, VGLUT1 in magenta, and merge. Scale bar, 10 µm. (B) Quantification of mean FLAG fluorescent intensity per cell of *Munc13-1/2* DKO rescued with Munc13-1 WT and C_2C mutants at VGLUT1 positive compartments. FLAG mean intensity were analyzed in 50 positive synapses per cell, in 10 different cells per group in 2 independent cultures. Data collected by Marcial Camacho.

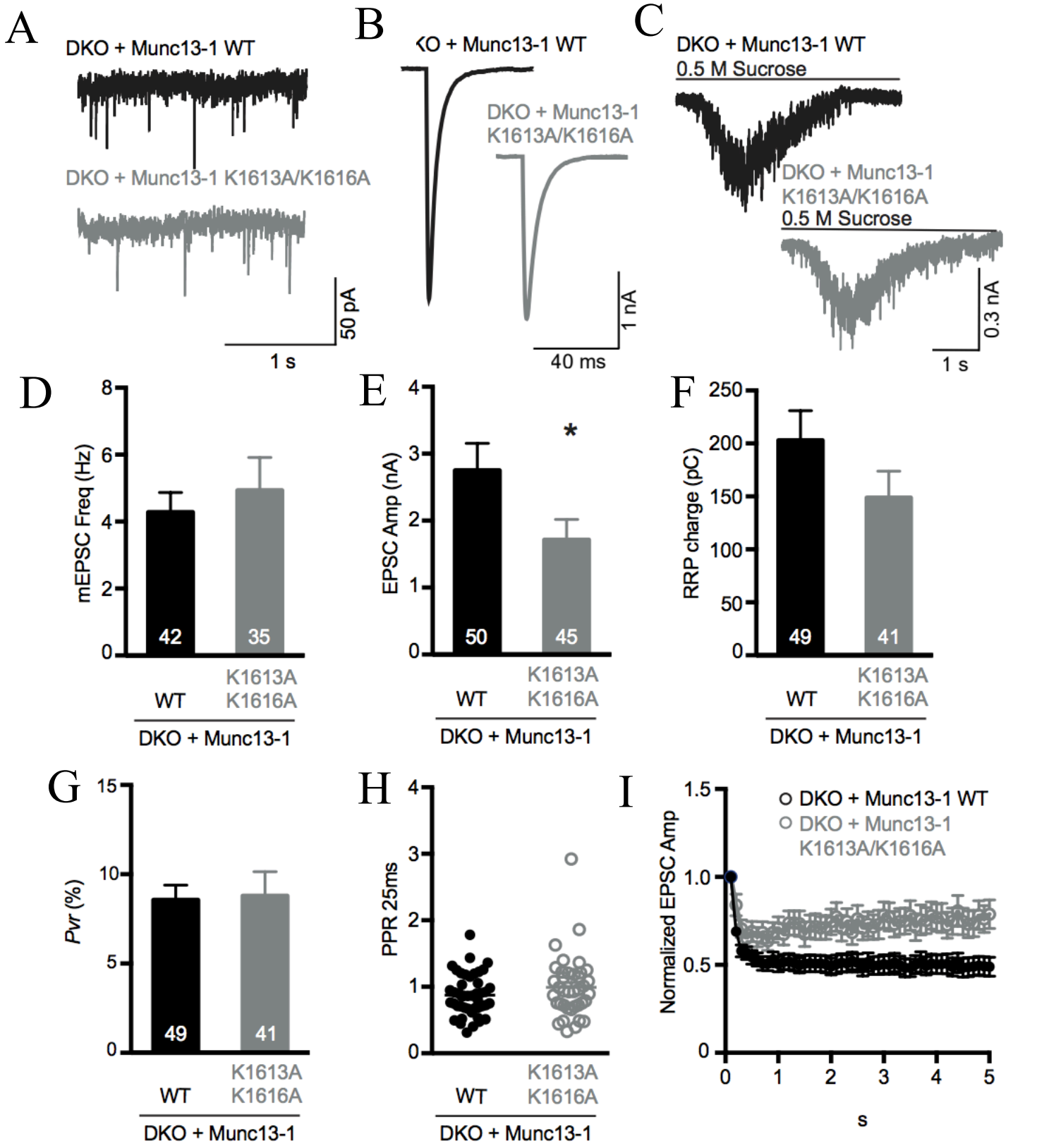

Figure 4.12 Electrophysiological analysis of the functional effects of mutations in the polybasic region of the Munc13-1 C_2C domain

(A-C) Examples of mEPSCs (A), EPSCs (B), and sucrose induced currents (C) recorded from DKO neurons expressing WT Munc13-1 (black) or a Munc13-1 with a double point mutation in the polybasic stretch within the C_2C domain, Munc13-1 K1613A/K1616A (grey). (D-F) Plots showing the average mEPSC frequencies (D), EPSC amplitudes (E), and RRP charges (F), obtained from the DKO neurons rescues with WT or K1613A/K1616A mutant Munc13-1. (G) Calculated P_{vr} in % for Munc13-1 WT and for the polybasic mutant K1613A/K1616A. (H) Graph showing the average paired-pulse rations calculated from 2 Aps with ISI of 25 ms (40 Hz) of DKO rescued with WT or K1613A/K1616A mutant Munc13-1. (I) Analysis of EPSC amplitudes in response to a train of 50 AP with an ISI of 100 ms (10 Hz) normalized to the first EPSC and plotted over time for the WT or K1613A/K1616A mutant Munc13-1 rescues. Numbers within the bars represent *n* values of each group. All data are mean ± SEM. Significance and p values were determined Mann Whitney test. *$p< 0.05$. Data collected by Marcial Camacho.

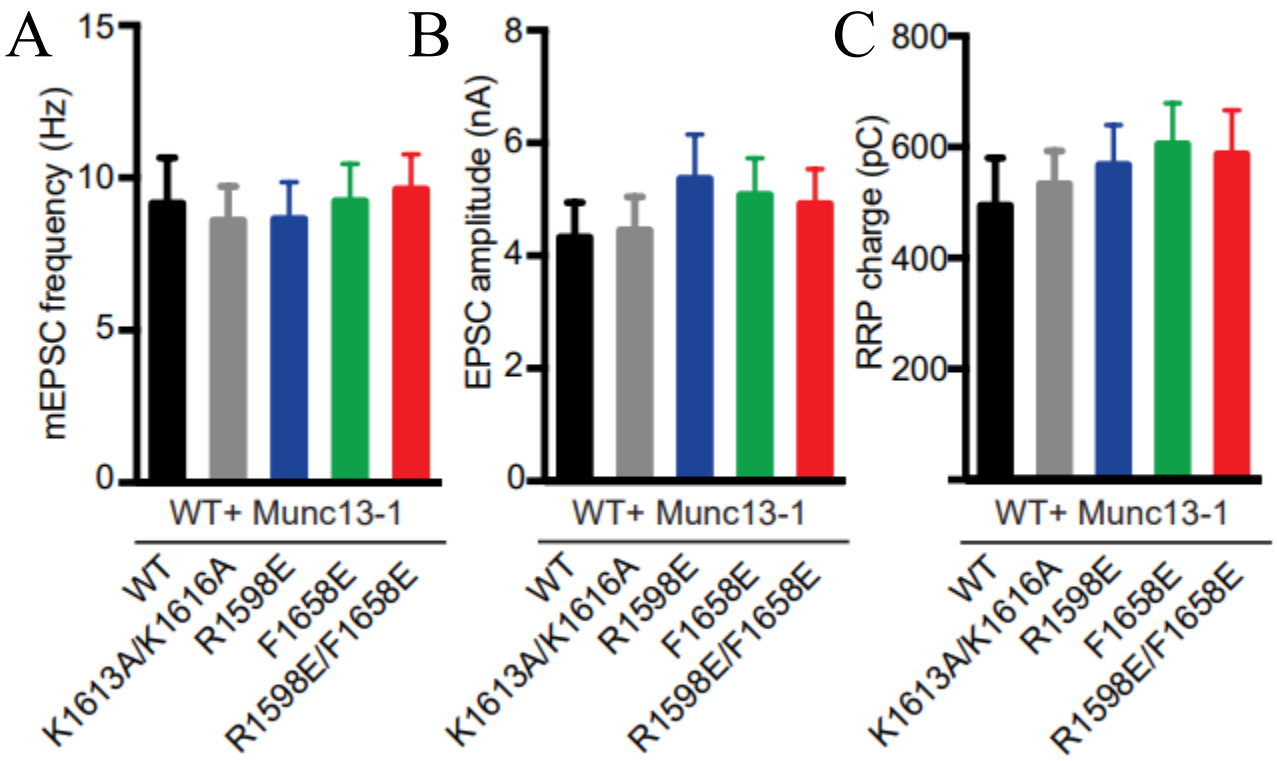

Figure 4.13 Electrophysiological analysis of the functional effects of overexpressing Munc13-1 bearing mutations in the putative membrane-binding loops and the polybasic region of the C_2C domain.
(A-C) Summary plots of average mEPSC frequencies (A), EPSC amplitudes (B), and RRP charges (C) from WT autaptic hippocampal neurons with overexpression of either Munc13-1 WT or the indicated Munc13-1 C_2C point mutants. Numbers in bar graphs present n values for each group. Significances and p values were determined by One-way ANOVA with Kruskal-Wallis test followed by Dunn's post-test. Values indicate mean ± SEM. Data collected by Marcial Camacho.

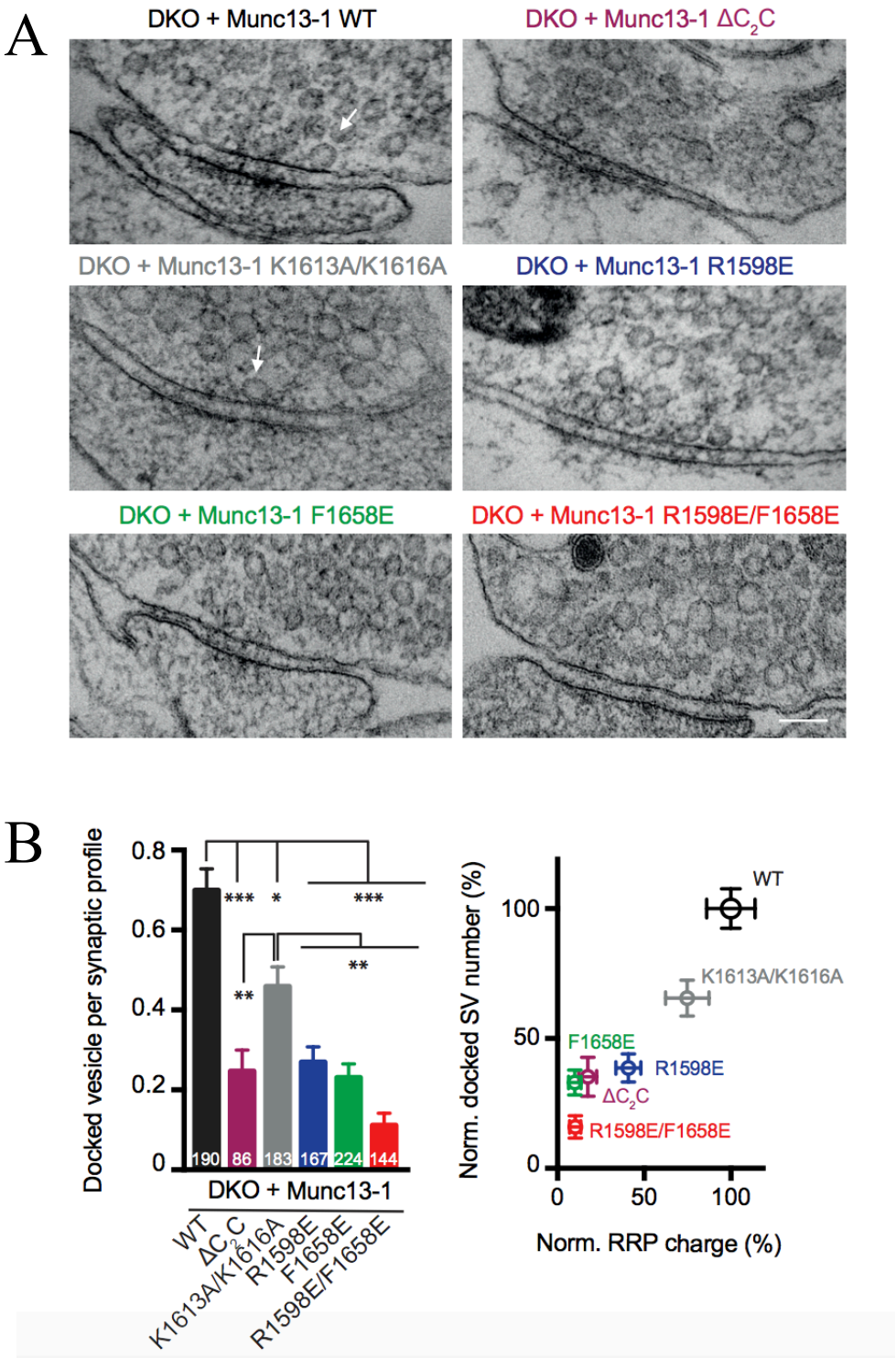

Figure 4.14 Effects of mutations in the Munc13-1 C_2C domain on synaptic vesicle docking

(A) Electron micrographs of synapses from DKO hippocampal cultures rescues with WT Munc13-1 and the indicated Munc13-1 C_2C mutants. White arrows indicate docked synaptic vesicles making contact with plasma membrane active zones. Scale bar represents 100 nm. (B) Mean number of docked synaptic vesicles per synaptic profile for WT Munc13-1 and the indicated Munc13-1 C2C mutants. (C) Plot showing the correlation between primed and docked synaptic vesicles measured after the rescues with WT Munc13-1 and the indicated Munc13-1 mutants. Numbers in bars are n numbers for each mutant group. Error bars represent SEM. Significance and p values were determined by Kruskal Wallis test followed by a multiple comparison. Values indicate mean ± SEM. *p< 0.05; **p<0.01; *** p<0.001 ; p<0.0001. Data collected by Marcial Camacho and Marta Orlando.

CHAPTER 5-Reorientation of Munc13 between membranes modulates the probability of neurotransmitter release

5.1 Introduction

Intracellular membrane fusion is driven by a core set of conserved proteins. At the center of these fusion events are the SNARE proteins syntaxin-1, SNAP25, and synaptobrevin-2 (Wickner and Rizo, 2017). The fusion that precedes neurotransmitter release and enables neurotransmission is different from other types of intracellular membrane fusion because it requires very tight regulation. There are many proteins regulating each step of this fusion process and linking it to a variety of cellular signals that modulate the probability of release. Among these proteins, Munc18-1, Munc13-1, synaptotagmin-1, α-SNAP, and NSF have been demonstrated as essential components of the fusion machinery. Each of these proteins participates in various steps of the synaptic vesicle fusion process from docking and priming all the way through fusion. Cellular messengers such as PIP_2, DAG, and calcium can interact with these proteins to regulate when, where, and how quickly fusion happens. Munc13-1, one of the essential components of the presynaptic fusion machinery, interacts with these cellular messengers so it can integrate a variety of chemical signals to modulate release probabilities.

The necessity of phosphoinositides, such as PIP_2, in presynaptic fusion is well established (Martin, 1998). When phosphoinositide concentrations are decreased in adrenal chromaffin cells by introduction of PLC or removal of ATP, calcium-dependent secretion is drastically reduced (Eberhard et al., 1990). Many presynaptic proteins have been implicated in PIP_2 binding such as synaptotagmin (Bai et al., 2004), syntaxin-1 (van den Bogaart et al., 2011), and Munc13-1(Shin et al., 2010), but the effect that PIP_2 has on these proteins varies. Synaptotagmin-1 has significantly higher calcium affinity in the presence of PIP_2 (van den Bogaart et al., 2012), while

syntaxin-1 is clustered to PIP_2-rich fusion sites (van den Bogaart et al., 2011). The Munc13 C_2B domain binds membranes in a PIP_2- and calcium-dependent manner and is also recruited to PIP_2 microdomains in a calcium-dependent manner (Shin et al., 2010, Kabachinski et al., 2014). Other membrane lipids, such as DAG, can also regulate fusion through Munc13-1 (Rhee et al., 2002). This may be due to translocation of the cytosolic protein to the plasma membrane or modulating biochemical signaling through Munc13-1.

Reconstitution experiments have recapitulated the necessity of PIP_2 and DAG in *in vitro* fusion assays (Liu et al., 2016). Removal of DAG or PIP_2 individually reduces fusion efficiency, but the removal of both significantly slows fusion. This is likely due, at least in part, to the ability of Munc13-1 to bind these cellular messengers since no other protein in the system has a clear dependence on PIP_2 or DAG. In the same study it was also shown that you can achieve fast and efficient calcium-dependent fusion when Munc13-1 is the only calcium-binding protein present and that mutating the calcium-binding sites of Munc13-1 significantly decreases fusion. This is not the case *in vivo* though. Mutating the calcium-binding sites has no effect on single action potential evoked release (Shin et al., 2010). It is only under high frequency, repetitive stimulation that you see depression relative to wild-type neurons, suggesting that calcium binding to C_2B may play a role in synaptic plasticity. These results suggest that Munc13-1 may integrate a variety of cellular signals to modulate the probability of release, allowing it to serve as a master regulator of fusion.

The molecular mechanisms allowing Munc13-1 to modulate the probability of release through DAG, PIP_2, and calcium binding are not well understood, but the recent structure of the conserved C_1C_2BMUN portion of Munc13-1 may provide some insights into these regulatory

mechanisms (Figure 5.1 A) (Xu et al., 2017). C_1C_2BMUN forms a long, 20 nm rod-like structure with the C_1 and C_2B domains situated right next to one another with the DAG-binding site of C_1 and the membrane-binding site of C_2B oriented in the same direction. It is expected that binding of both domains corresponds to the fusion-ready state that only happens in the presence of calcium or high levels of negatively charged phosphoinositides. There are also many positively charged residues on the side of, and adjacent to, the C_1 domain that could permit an alternative binding site that will engage C_1 only. Binding in this orientation may also enable more efficient docking and correspond to an inhibited, prefusion state. Recent evidence from unc13 studies suggest that the C_1 and C_2B domains may facilitate an autoinhibited state that is relieved by calcium-binding to C_2B (Michelassi et al., 2017). This supports the notion that there may be some reorientation between membranes from an inhibited, prefusion state to a calcium-bound fusogenic state. It is expected that under repetitive stimulation the free calcium concentration in the neuron steadily increases, which increases the probability of reorienting into the fusogenic state. This may by the underlying mechanism by which C_2B regulates short-term synaptic plasticity and may provide insights into how Munc13-1 assemblies can tune synaptic strength (Sakamoto et al., 2018, Shin et al., 2010).

To understand how Munc13-1 modulates the probability of release we need to further understand how these ligands change Munc13-1 membrane binding and regulate the membrane-bridging orientation. Using mutations in Munc13-1 that impair binding through specific sites and monitoring clustering by dynamic light scattering experiments, we showed that there are distinct binding sites that are involved in calcium-independent and calcium-dependent membrane binding. By monitoring calcium-independent and calcium-dependent fusion in our

reconstitutions, the observations made by DLS were validated. Using FRET assays that monitor the formation of membrane anchored trans-SNARE complexes, we show that DAG stimulates the formation of the SNARE complex in the absence of calcium, providing a possible link between Munc13-1-dependent DAG binding and priming. To better understand the role of calcium binding to Munc13,-1 we performed calcium-titrations using *in vitro* reconstitutions and show that PIP_2 dramatically increases the calcium sensitivity of Munc13-1. Taken together, these results suggest that calcium-dependent reorientation of Munc13-1 plays a major role in stimulating fusion and that changing the orientation of Munc13-1 between membranes by binding to calcium, PIP_2, and DAG may regulate the probability of release *in vivo*.

5.2 Methods

5.2.1 Plasmids and Recombinant Proteins

Expression and purification of full-length *Homo sapiens* SNAP-25A with its four cysteines mutated to serine, full-length *Rattus norvegicus* synaptobrevin-2, full-length *Rattus norvegicus* Munc18-1, full- length *Cricetulus griseus* NSF V155M mutant, *Rattus norvegicus* synaptotagmin-1 57-421 C74S/C75A/C77S/C79I/C82L/C277S (a kind gift from Thomas Sollner), and full-length *Bos taurus* α-SNAP in *E.* coli were described previously (Chen et al., 2006, Dulubova et al., 1999, Dulubova et al., 2007, Ma et al., 2013, Liu et al., 2016). Standard PCR-based recombinant DNA techniques with custom-designed primers were on the parent DNA to create expression vectors for SNAP-25A M71D/L78D, Munc18-1 D326K, synaptobrevin-2 L26C, syntaxin-1A C145A/C271A/C272A/S186C, and Munc13-1 K603E, K706E, K720E, R769E, K603E/K720E, K706E/R769E, K603E/K706E/K720E/R769E. All

mutant proteins were expressed following the purification protocols for wild type constructs with the addition of extra reducing agent in the cysteine mutants.

All recombinant *Rattus Norvegicus* Munc13-1 fragments contained a deletion in a large variable loop (residues 1408-1452) that improves the solubility (Ma et al., 2011). Expression and purification of His_6-Munc13-1 $C_1C_2BMUNC_2C$ (WT and mutants) encoded in a pET28a vector was performed in *E. coli* BL21 (DE3) cells. Transformed cells were grown in the presence of 50 μg/ml kanamycin to an OD_{600} of ~0.8 and induced overnight at 16°C with 500 μM IPTG. Cells were harvested by centrifugation and re-suspended in 50 mM Tris, pH 8, 250 mM NaCl, 1 mM TCEP, 10% glycerol (v/v) prior to lysis. Cell lysates were centrifuged for 30 minutes at 48,000 x g to clarify the lysate and then incubated with Ni-NTA resin for 30 minutes at room temperature. The resin was washed with re-suspension buffer and re-suspension buffer with 750 mM NaCl to remove contaminants. Nuclease treatment was performed on the beads for 1 hour at room temperature using 250 U of Pierce Universal Nuclease (Thermo Fisher Scientific) per liter of cells. Protein was eluted using re-suspension buffer with 500 mM imidazole and dialyzed against 50 mM Tris, pH 8, 250 mM NaCl, 1 mM TCEP, 2.5 mM CaCl, 10% glycerol (v/v), overnight at 4°C in the presence of thrombin. The solution was re-applied to Ni-NTA resin to remove any uncleaved protein and diluted twentyfold with 20 mM Tris, pH 8, 1 mM TCEP, 10% glycerol (v/v). Diluted protein was subjected to anion exchange chromatography using a HiTrapQ HP column (GE Life Sciences) and eluted in 20 mM Tris, pH 8, 1 mM TCEP, 10% glycerol (v/v) with a linear gradient from 1% to 50% of 1 M NaCl.

His-full-length *s*yntaxin-1A (wild type and mutant) encoded in a pET28a was expressed in BL21 (DE3) *E. coli*. Transformed cells were grown in the presence of 50 μg/ml kanamycin to an OD_{600} of ~0.8 and induced overnight at 20°C with 400 μM IPTG. Cells were harvested by centrifugation and re-suspended in extraction buffer (20 mM Hepes, pH 7.4, 500 mM NaCl, 8 mM imidazole) prior to lysis. Cell lysates were centrifuged at 14,500 x g for 20 minutes. The supernatant was discarded and the pellet containing the protein was re-suspended and pelleted again. The pellet was re-suspended in extraction buffer with 2% Triton-X 100 (Sigma-Aldrich) and 6 M urea and incubated for 1 hour at 4°C to solubilize the protein. Cell debris was pelleted by centrifugation at 48,000 x g for 1 hour and the supernatant was applied to Ni- NTA resin. The resin was washed sequentially with wash buffer (20 mM Hepes, pH 7.4, 500 mM NaCl, 20 mM imidazole) containing 6 M urea, 10% glycerol (v/v), 1% Triton-X 100 and then 20% glycerol (v/v), 1% Triton-X 100 and then 1% Triton-X 100 and finally 0.1% n-Dodecylphosphocholine (DPC; Anatrace). The protein was eluted in elution buffer (20 mM Hepes, pH 7.4, 500 mM NaCl, 400 mM imidazole, 0.1 DPC) and the Hisremoved by thrombin cleavage overnight at 4°C. Gel filtration was performed on a Superdex 200 10/300 GL column (GE Life Science) in 20 mM Tris, pH 7.4, 150 mM NaCl, 1 mM TCEP, 0.2% DPC.

5.2.2 Fluorescent tagging of syntaxin-1A and synaptobrevin-2

Single cysteine mutants of syntaxin-1A and synaptobrevin-2 were labeled with tetramethylrhodamine (Thermo Fisher Scientific) and Alexa Fluor 488 (Thermo Fisher Scientfic) respectively using maleimide chemistry. Full-length synaptobrevin-2 L26C was buffer exchanged into 20 mM Tris, pH 7.4, 150 mM NaCl, 1 mM TCEP, 1% octyl β-glucopyranoside (β-OG) and mixed with a 20-fold excess of Alexa Fluor 488 for 2 hours at room temperature.

Unreacted dye was removed using cation exchange chromatography on a HiTrap SP column (GE Life Science) in 25 mM sodium acetate, pH 5.5, 1 mM TCEP, 1% β-OG using a linear gradient from 0 to 1000 mM NaCl. Full length syntaxin-1A C145A/C271A/C272A/S186C in 20 mM Tris, pH 7.4, 150 mM NaCl, 1 mM TCEP, 0.2% DPC was mixed with a 20-fold excess of tetramethylrhodamine for 2 hours at room temperature. Unreacted dye was removed using anion exchange chromatography on a HiTrap Q HP (GE Life Sciences) in 20 mM Tris, pH 7.4, 1 mM TCEP, 0.1% DPS using a linear gradient from 0 to 1000 mM NaCl.

5.2.3 Liposome Fusion Assays

Liposome lipid and content mixing assays were performed as previously described (Liu et al., 2016, Liu et al., 2017). To prepare the phospholipid vesicles, POPC, DOPS, POPE, PIP2, DAG, 1,2- dipalmitoyl-*sn*-glycero-3-phosphoethanolamine-N-(7-nitro-2-1,3-benzoxadiazol-4-yl) (ammonium salt) (NBD-PE), 1,2-Dihexadecanoyl-*sn*-glycero-3-phosphoethanolamine (Marina Blue DHPE), and cholesterol in chloroform were mixed at the desired ratio and dried under a stream of nitrogen gas. T-liposomes contained 38% POPC, 18% DOPS, 20% POPE, 2% PIP2, 2% DAG, and 20% Cholesterol, and V-liposomes contained 39% POPC, 19% DOPS, 19% POPE, 20% Cholesterol, 1.5% NBD PE, and 1.5% Marina Blue DHPE. The dried lipids were left overnight in a vacuum chamber to remove the organic solvent. The next day the lipid films were hydrated with 25 mM Hepes, pH 7.4, 150 mM KCl, 1 mM TCEP, 2% n-Octyl-β-D-glucoside (β-OG) and 10% glycerol (v/v) by vortexing for 5 minutes. Rehydrated lipids for T-liposomes were mixed with protein and dye to get a final concentration of 4 mM lipid, 5 μM full-length syntaxin-1, 25 μM full-length SNAP-25, and 4 μM R-phycoerythrin biotin-XX conjugate (Invitrogen). Rehydrated lipids for V-liposomes were mixed with protein and dye to get a final

concentration of 4 mM lipid, 8 μM full-length synaptobrevin, and 8 μM Cy5-streptavidin conjugate (Seracare Life Sciences Inc.). Lipid mixtures were dialyzed 1 hr, 2 hr and overnight at 4°C in 25 mM Hepes, pH 7.4, 150 mM KCl, 1 mM TCEP, 10% glycerol (v/v) in the presence of Amberlyte XAD-2 beads (Sigma) to remove the detergent and promote the formation of proteoliposomes. The next day the proteoliposomes were harvested and mixed with Histodenz (Sigma) to a final concentration of 35%. Proteoliposome mixtures were added to a centrifuge tube with 25% Histodenz and 25 mM Hepes, pH 7.4, 150 mM KCl, 1 mM TCEP, 10% glycerol layered on top. The proteoliposomes were spun at 4°C for 1.5 hours at 55,000 RPM in an SW-60 TI rotor and the top layer was collected. Concentrations of the final T-proteoliposomes were measured by the Stewart method (Stewart, 1980). V-proteoliposome concentrations were estimated from the UV-vis absorption using a standard curve made using known quantities of liposomes containing 1.5% NBD-PE.

To perform the fusion assays, T-liposomes (250 μM total lipid) were first incubated with 1 μM Munc18-1 wild type and mutant, 0.8 μM NSF, 2 μM αSNAP, 2 mM ATP, 2.5 mM Mg^{2+}, 5 μM streptavidin, and 100 μM EGTA for 15-25 minutes at 37°C, and then were mixed with V-liposomes (125 μM total lipid), 1 μM SNAP-25, and wild type Munc13-1 fragments at the specified concentration. After 5 minutes 0.6 mM Ca^{2+} was added to stimulate fusion, and 1% β-OG was added after 25 minutes to solubilize the liposomes. The fluorescence signals from Marina Blue (excitation at 370 nm, emission at 465 nm) and Cy5 (excitation at 565 nm, emission at 670 nm) were recorded to monitor lipid and content mixing, respectively. The lipid mixing data were normalized to the maximum fluorescence signal observed upon detergent addition.

The content mixing data were normalized to the maximum Cy5 fluorescence observed after detergent addition in control experiments without external streptavidin.

5.2.4 Dynamic Light Scattering

To prepare phospholipid vesicles, 1-palmitoyl-2-oleoyl-sn-glycero-3-phosphocholine (POPC), 1,2- dioleoyl-sn-glycero-3-phospho-L-serine (DOPS), 1-palmitoyl-2-oleoyl-sn-glycero-3-phosphoethanolamine (POPE), L-a-Phosphatidylinositol-4,5-bisphosphate (PIP_2), 1-palmitoyl-2-oleoyl-*sn*-glycerol (DAG), and cholesterol dissolved in chloroform were mixed at the desired ratios and then dried under a stream of nitrogen gas. T-type liposomes contained 38% POPC, 18% DOPS, 20% POPE, 2% PIP2, 2% DAG, and 20% Cholesterol, and V-type liposomes contained 39% POPC, 19% DOPS, 22% POPE, and 20% Cholesterol. The dried lipids were left overnight in a vacuum chamber to remove the organic solvent. The next day the lipid films were hydrated with 25 mM HEPES, pH 7.4, 150 mM KCl, 10% glycerol (v/v) and vortexed for 5 minutes followed by five freeze-thaw cycles. Large unilamellar vesicles were prepared by extruding the hydrated lipid solution through a 100 nm polycarbonate filter 31 times with an Avanti Mini-Extruder. T-proteoliposomes containing syntaxin-1/SNAP-25 complex and V-proteoliposomes containing synaptobrevin-2 proteoliposomes were prepared using dialysis following the standard reconstitution protocol in the previous section. In the noted preparations DAG and PIP_2 were replaced by an equivalent percentage of POPC.

Liposome clustering induced by Munc13 fragments was analyzed using a Wyatt Dynapro Nanostar (Wyatt Technology) dynamic light scattering instrument equipped with a temperature controlled microsampler as previously described (Liu et al., 2016). Briefly, the specified

Munc13-1 fragment (500 nM) was incubated at room temperature for 2 minutes with T-liposomes (250 μM total lipid) and V-liposomes (125 μM total lipid) in 25 mM HEPES, pH 7.4, 150 mM KCl, 100 μM EGTA, 10% glycerol (v/v) prior to measuring the particle size. After the addition of 600 μM Ca^{2+} (to achieve a 500 μM free Ca^{2+} concentration) the sample was incubated for an additional 3 minutes before measurement.

5.2.5 Measuring Calcium Concentrations During Liposome Fusion Assays

Liposome lipid mixing assays were performed basically as previously described (Liu et al., 2016, Liu et al., 2017). To prepare the phospholipid vesicles, POPC, DOPS, POPE, PIP2, DAG, and cholesterol in chloroform and 1,1'-dioctadecyl-3,3,3',3'-tetramethylindodicarbocyanine, 4-chlorobenzenesulfonate salt (DiD, Invitrogen) in DMSO were mixed at the desired ratio and dried under a stream of nitrogen gas. T-liposomes contained 38% POPC, 18% DOPS, 20% POPE, 2% PIP2, 2% DAG, and 20% Cholesterol, and V-liposomes contained 38.5% POPC, 19% DOPS, 19% POPE, 20% Cholesterol, and 3.5% DiD. In the noted experiments PIP_2 was replaced with an equivalent percentage of POPC. The dried lipids were left overnight in a vacuum chamber to remove the organic solvent. The next day the lipid films were hydrated with 25 mM Hepes, pH 7.4, 150 mM KCl, 1 mM TCEP, 2% n-Octyl-β-D-glucoside (β-OG) and 10% glycerol (v/v) by vortexing for 5 minutes. Rehydrated lipids for T-liposomes were mixed with protein to get a final concentration of 4 mM lipid, 5 μM full-length syntaxin-1, 25 μM full-length SNAP-25. Rehydrated lipids for V-liposomes were mixed with protein to get a final concentration of 4 mM lipid and 8 μM full-length synaptobrevin. Lipid mixtures were dialyzed 1 hr, 2 hr and overnight at 4°C in 25 mM Hepes, pH 7.4, 150 mM KCl, 1

mM TCEP, 10% glycerol (v/v) in the presence of Amberlyte XAD-2 beads (Sigma) to remove the detergent and promote the formation of proteoliposomes.

To perform the fusion assays, T-liposomes (250 μM total lipid, with and without PIP2) were first incubated with 1 μM Munc18-1 wild type, 0.8 μM NSF, 2 μM αSNAP, 2 mM ATP, 2.5 mM Mg^{2+}, 5 μM streptavidin, EGTA (100 μM for samples with PIP2 and 10 μM for samples without PIP_2), and 0.5 μM Fluo-4, pentapotassium salt (Invitrogen, no Fluo-4 was used in the samples with no PIP_2) for 15-25 minutes at 37°C. To initiate the reaction preincubated T-liposomes were mixed with V-liposomes (125 μM total lipid), 1 μM SNAP-25, and 0.1 μM $C_1C_2BMUNC_2C$. After 5 minutes Ca^{2+} was added to stimulate fusion, and 1% β-OG was added after 25 minutes to solubilize the liposomes. Throughout the reaction lipid mixing was monitored using DiD dequenching with excitation at 560 nm and emission measured at 670 nm. After solubilization of samples containing PIP2, the Fluo-4 emission intensity was measured from 505 to 540 nm with excitation at 465 nm. To measure the maximum fluorescence of Fluo-4, 10 mM Ca^{2+} was added to each sample before measuring a second time. Calcium concentrations were calculated as previously described (Grynkiewicz et al., 1985). Calcium concentrations for samples lacking PIP_2 were assumed to be near the total calcium concentration due to the low amount of EGTA and large amount of calcium used for each sample.

5.2.6 SNARE Complex Assembly Assay

Proteoliposomes used in this assay were prepared similar to previously described (Liu et al., 2016, Liu et al., 2017). To prepare the phospholipid vesicles, POPC, DOPS, POPE, PIP2, DAG, and cholesterol in chloroform were mixed at the desired ratio and dried under a stream of

nitrogen gas. Standard T-liposomes with syntaxin-1A/SNAP-25 contained 38% POPC, 18% DOPS, 20% POPE, 2% PIP2, 2% DAG, and 20% Cholesterol, V-liposomes with synaptobrevin-2 contained 39% POPC, 19% DOPS, 22% POPE, and 20% Cholesterol, and V-liposomes with synaptobrevin-2 and synaptotagmin-1 contained 40% POPC, 6.8% DOPS, 33.2% POPE, 20% cholesterol. In the noted experiments DAG or PIP_2 were replaced with an equivalent percentage of POPC. The dried lipids were left overnight in a vacuum chamber to remove the organic solvent. The next day the lipid films were hydrated with 25 mM Hepes, pH 7.4, 150 mM KCl, 1 mM TCEP, and 2% n-Octyl-β-D- glucoside (β-OG) by vortexing for 5 minutes. Rehydrated lipids for T-liposomes were mixed with protein to get a final concentration of 4 mM lipid, 5 μM full-length tetramethylrhodamine labeled syntaxin-1, 25 μM full-length SNAP-25 M71D/L78D. Rehydrated lipids for V-liposomes with synaptobrevin-2 were mixed with protein to get a final concentration of 4 mM lipid and 0.4 μM full-length Alexa 488 labeled synaptobrevin-2. Rehydrated lipids for V-liposomes with synaptobrevin-2 and synaptotagmin-1 were mixed with protein to get a final concentration of 2.5 mM lipid, 0.25 μM full-length Alexa 488 labeled synaptobrevin, 2.5 μM full-length synaptotagmin-1, and 600 mM KCl. Lipid mixtures were dialyzed 1 hr, 2 hr and overnight at 4°C in 25 mM Hepes, pH 7.4, 150 mM KCl, and 1 mM TCEP in the presence of Amberlyte XAD-2 beads (Sigma) to remove the detergent and promote the formation of proteoliposomes.

All FRET experiments were performed at 37°C on a PTI Quantamaster 400 spectrofluorometer with all slits set to 1.25 mm and a GG495 longpass filter to filter scattered light. Kinetic measurements were made by monitoring the decrease in Alexa 488 fluorescence at 518 nm (excitation at 468 nm) as FRET with tetramethylrhodamine increases. V-liposomes

containing synaptobrevin-2 or synaptobrevin-2 and synaptotagmin-1 were mixed at 0.0625 μM with 1 μM Munc18-1, 0.8 μM NSF, 2 μM αSNAP, 2 mM ATP, 2.5 mM Mg^{2+}, 100 μM EGTA,1 μM SNAP-25 M71D/L78D, and 0.1 μM or 0.5 μM $C_1C_2BMUNC_2C$. Reactions were incubated for 3 minutes as the baseline Alex488 fluorescence stabilizes and then T-liposomes with the specified composition were mixed in to initiate the reaction. Reactions were allowed to proceed independent of calcium until equilibrium or 600 μM Ca^{2+} was added after 5 minutes. Data was processed by correcting for dilution from added components and then dividing each point by the maximum Alexa 488 fluorescence.

5.3 Results

5.3.1 Defining calcium-dependent and calcium-independent membrane binding interfaces

Based on the previous structure of C_1C_2BMUN, it was hypothesized that Munc13-1 has calcium-independent and calcium-dependent membrane binding sites (Xu et al., 2017). The presence of the calcium-independent binding site is further supported by cryo-electron tomography of reconstitution samples showing that Munc13-1 binds nearly perpendicular to the membrane in the absence of calcium and does not appear to engage along the C_1C_2B interface (Figure 4.4). With this in mind, we identified a series of basic residue clusters expected to bind membranes independent and dependent of calcium, and made several charge reversal mutations to impair membrane binding (Figure 5.1B). The calcium-independent interface is referred to as interface 1 while the calcium-dependent interface is referred to as interface 2.

We tested the ability of the interface 1 and interface 2 mutants to cluster T- and V-composition liposomes with and without calcium using dynamic light scattering. As previously reported, wild-type $C_1C_2BMUNC_2C$ clusters plasma membrane and synaptic vesicle liposomes in the absence of calcium, with no significant increase upon calcium addition (Figure 5.2 A). The K603E, K720E, and K603E/K720E mutants, which bear charge reversal mutations in interface 1, are no longer able to cluster upon protein addition, but cluster liposomes as well as wild-type upon calcium addition (Figure 5.2 B,D,F). The K706E mutant, which contains a charge reversal within interface 2, has clustering abilities similar to wild-type because interface 1 is unchanged and that drives clustering by $C_1C_2BMUNC_2C$ (Figure 5.2 C). While C1C2BMUNC2C has no calcium-dependence on clustering, we expect this mutant to impact calcium-dependent fusion. The R769E single mutant and K706E/R769E double mutant impair calcium-independent clustering (Figure 5.2 E,G), which was unexpected due to their location within the membrane-binding loops of the C_2B domain. These mutants were originally designed to impair interface 2, but it appears that R769E is involved in both and may serve as a hinge between the two interfaces. Interestingly, the K706E/R769E mutant appears to cluster liposomes somewhat less efficiently than wild-type upon calcium addition, hinting that this mutation may impair calcium-dependent fusion. Finally, the K603E/K706E/K720E/R769E quadruple mutant lacks the ability to cluster because both interface 1 and interface 2 are broken (Figure 5.2 H).

To understand the effect of these mutants on calcium-dependent fusion, we used these mutants in place of wild-type $C_1C_2BMUNC_2C$ in full system reconstitutions. The K603E, K720E, and K603E/K720E mutants within interface 1 had no impact on calcium-dependent fusion (Figure 5.3 A,B,E), which is in line with the dynamic light scattering data. The K706E

and R769E mutants within interface 2 also had very little impact on calcium-dependent fusion (Figure 5.3 A,B,E), most likely because a single charge reversal is not sufficient to overcome the high affinity calcium-dependent membrane binding. The K706E/R769E double mutant within interface 2 has a strong impact on calcium-dependent fusion that arises from significant charge reversal in this region, while the K603E/K706E/K720E/R769E mutant of interface 1 and 2 completely lacks the ability to stimulate fusion (Figure 5.3 A,B,E). Using the full system reconstitutions to study the impact of interface 1 mutations is problematic because there is little calcium-independent fusion using this system. To overcome this issue, we introduced the previously studied gain-of-function D326K Munc18-1 mutant into our system. Since D326K Munc18-1 enables calcium-independent SNARE complex formation and fusion (Sitarska et al., 2017), we are able to monitor calcium-independent changes that result from Munc13-1 mutations. Strikingly, the K603E and K603E/K720E interface 1 mutants as well as the R769E and K706E/R769E interface 2 mutants lack the ability to stimulate calcium-independent fusion (Figure 5.3 C,D,F). The dynamic light scattering results showed that these mutants are unable to cluster liposomes without calcium, so they have a corresponding decrease in calcium-independent fusion. Interestingly, the K720E interface 1 and the K706E interface 2 mutant show similar decreases in calcium-independent fusion because they both retain some ability to cluster independent of calcium. As expected, the K603E/K706E/K720E/R769E quadruple mutant lacks the ability to catalyze calcium-independent fusion because it is no longer able to cluster. The dynamic light scattering and reconstitution data suggest that the notion of distinct calcium-dependent and calcium-independent membrane binding sites is correct, but the boundaries for both sites are not clear. This becomes evident with the impact of the R769E mutation on both

calcium-dependent and calcium-independent fusion. Given this residues location within the membrane-binding loops of C_2B, it is probably a hinge residue involved in both interfaces (Figure 5.1B).

5.3.2 DAG and PIP_2 increase trans-SNARE complex formation

To assess the role of DAG and PIP_2 in fusion I monitored trans-SNARE complex formation in the presence and absence of PIP_2, DAG, and calcium. Synaptobrevin-2 is tagged with a FRET donor and synataxin-1 is tagged with a FRET acceptor, so when SNARE complex forms the probes are brought in close proximity and a decrease in FRET donor fluorescence can be measured. In assays containing the SNAREs, synaptotagmin-1 full-length, NSF, α-SNAP, Munc18-1, and $C_1C_2BMUNC_2C$, there is a small amount of trans-SNARE complex that forms independent of calcium with a significant increase in formation after calcium addition (Figure 5.4 A). Removal of DAG or PIP_2 alone has little impact on calcium-dependent SNARE complex formation, but removal of both DAG and PIP_2 results in slower trans-SNARE complex formation. The decrease in trans-SNARE complex formation corresponds with a decrease in clustering between T- and V-composition liposomes when DAG and PIP_2 are removed from the T-composition (Figure 5.5 D). Interestingly, there is a small decrease in calcium-independent trans-SNARE complex formation in all samples lacking DAG (Figure 5.4 A). To further test this conclusion, I performed the same assay in the absence of synaptotagmin-1 full-length and five-fold more $C_1C_2BMUNC_2C$. There is a roughly 3-fold decrease in the amount of trans-SNARE complex that forms in the absence of DAG and calcium, suggesting that DAG may influence priming through Munc13-1. It was initially expected that DAG may decrease calcium-

independent clustering, but it turns out that clustering with membranes lacking DAG is comparable to standard plasma membrane composition vesicles (Figure 5.5 B). From the structure of C_1C_2BMUN, it appears that favoring binding through the C_1 domain will bring the plasma membrane and synaptic vesicle closer together than if Munc13-1 engages the membrane in a perpendicular orientation. This slight reorientation may enable formation of the N-terminus of the SNARE complex and underlie the ability of DAG to stimulate Munc13-dependent fusion.

5.3.3 Measuring the calcium affinity of C_1C_2BMUNC_2C stimulated fusion

Since there is evidence that short-term plasticity is regulated by residual calcium binding to the C_2B domain of Munc13-1, I was interested in the amount of calcium required to stimulate fusion in our reconstitution systems. Even with extensive water purification there is enough free calcium available in the water to stimulate nearly complete membrane fusion in our reconstitution system (Figure 5.6 A), so I used a calcium-sensitive fluorophore, called Fluo-4, to measure the free calcium concentration in various reaction conditions (Figure 5.6 B). The free calcium concentration can then be correlated with the percent of lipid mixing to measure the EC50 of the reconstitution system. From previous experiments it was expected that the EC50 would be lower than single digit micromolar (Liu et al., 2016), but an absolute value was never measured. Using the standard full system reconstitution including the SNAREs, NSF, α-SNAP, Munc18-1, and C_1C_2BMUNC_2C, an EC50 of ~1 μM was derived (Figure 5.7 A,B). The resting calcium concentration at the presynapse is roughly 100 nM, so with this EC50 it is expected that a small fraction of Munc13-1 may be activated prior to fusion. As the residual calcium climbs under repetitive stimulation the number of Munc13-1 molecules in the active state will increase,

thereby increasing the probability of release. This increase in probability of release will result in a lower amount of synaptic depression under high-frequency stimulation. One should keep in mind that the EC50 from this experiment may not match the EC50 *in vivo* because this system lacks factors that localize Munc13-1 to the site of fusion as well as other proteins and ligands that may enhance the calcium affinity of Munc13-1. In fact, this should be an upper bound estimate for the EC50 because the reconstitution system is incomplete.

I performed the same experiment again, but with plasma membrane composition liposomes lacking PIP_2 to see if PIP_2 enhances the calcium affinity of Munc13-1. This would not be an unexpected finding because PIP_2 dramatically increases the calcium affinity of other calcium-sensing C_2 domain proteins such as synaptotagmin-1 (van den Bogaart et al., 2012) and PIP_2 was shown to strongly enhance binding of Munc13-1 C_2B to membranes (Shin et al., 2010). In this case the experiments were performed in the absence of a calcium-sensitive fluorophore because the concentrations of calcium needed to stimulate fusion in the absence of PIP_2 are much higher than the amount of EGTA needed to inhibit fusion (data not shown), making the total calcium concentration a reasonable approximation of free calcium. This experiment resulted in an EC50 of ~30 μM (Figure 5.7 C,D), which is significantly lower than the value of ~1 μM derived in the presence of PIP_2. This finding validates the previously proposed hypothesis that suggests that regulating PIP_2 levels in the presynaptic membrane can tune synaptic plasticity (Cremona and De Camilli, 2001). Increases in PIP_2 will increase the calcium sensitivity of Munc13-1 and in turn increase the probability of release at resting calcium concentrations. Since phosphorylation and dephosphorylation can happen on the timescale of short-term plasticity it is

that likely that these biochemical pathways can modulate PIP_2 levels to facilitate or depress neurons in a Munc13-1-dependent manner (Eberhard and Holz, 1991, Shin et al., 2010).

5.3.4 A basic model for Munc13-dependent presynaptic plasticity.

With the previous experiments in mind, one can propose a basic model for Munc13-1-dependent presynaptic plasticity (Figure 5.8). Initially, Munc13-1 is localized to the active zone through interactions between the C_2A domain and αRIMs. Upon localization the C_1C_2B interface will engage with the plasma membrane in a nearly perpendicular orientation mediated through basic charges on the side of C_1 and C_2B. In this extended orientation the C_2C domain of Munc13 is free to bind synaptic vesicles, but the rigid separation between the synaptic vesicle and plasma membrane inhibits SNARE complex formation. If DAG is in the plasma membrane at high enough concentrations, the C1 domain of Munc13-1 will fully engage with the membrane, resulting in a slight reorientation that enables the opening of syntaxin-1 by the MUN domain and formation of the N-terminus of the SNARE complex on Munc18-1. The balance between free intracellular calcium and PIP_2 will facilitate calcium binding to a fraction of Munc13-1 molecules, resulting in an even greater tilt that brings the machinery closer together and increases the probability of release. Since each distinct release site has multiple Munc13-1 molecules, there will be an overall balance between ligand-bound and ligand-free Munc13-1 that dictates the overall release probability at each site, and modulating intracellular calcium, PIP_2, and DAG concentrations at each site will tip the balance to favor facilitation or depression.

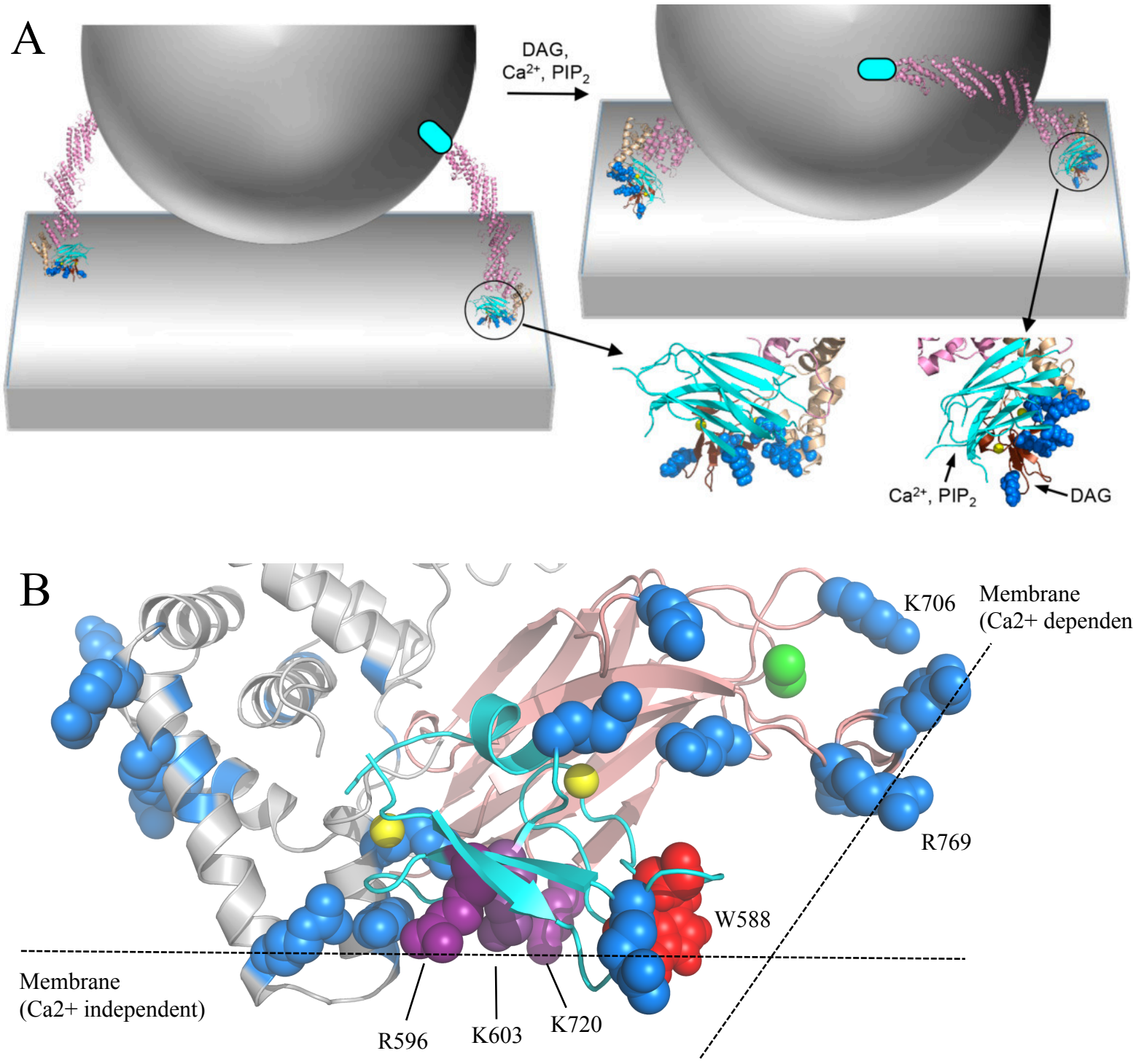

Figure 5.1 A model for Munc13-dependent movement of synaptic vesicles
(A) A simple model using the structure of C_1C_2BMUN showing a potential range of orientations upon ligand binding to C_1 and C_2B. In the ligand-free state there should be separation between the plasma membrane and synaptic vesicle, with the distance between membranes decreasing in the presence of calcium, PIP_2, or DAG. Zoom ins show the finer details of the distinct membrane binding sites. (B) A zoom in of the C_1C_2B interface with dashed lines representing the expected calcium-independent membrane binding site, referred to as interface 1, and calcium-dependent membrane binding site, referred to as interface 2. The structure of the calcium-bound C_2B was superposed over the calcium-free C_2B in the C_1C_2BMUN structure. Blue spheres represent basic residues that may be involved in membrane binding. Yellow spheres represent zinc ions. Green spheres represent calcium ions. Red spheres represent the DAG sensing tryptophan of C_1. Panel A adapted from Rizo, 2018.

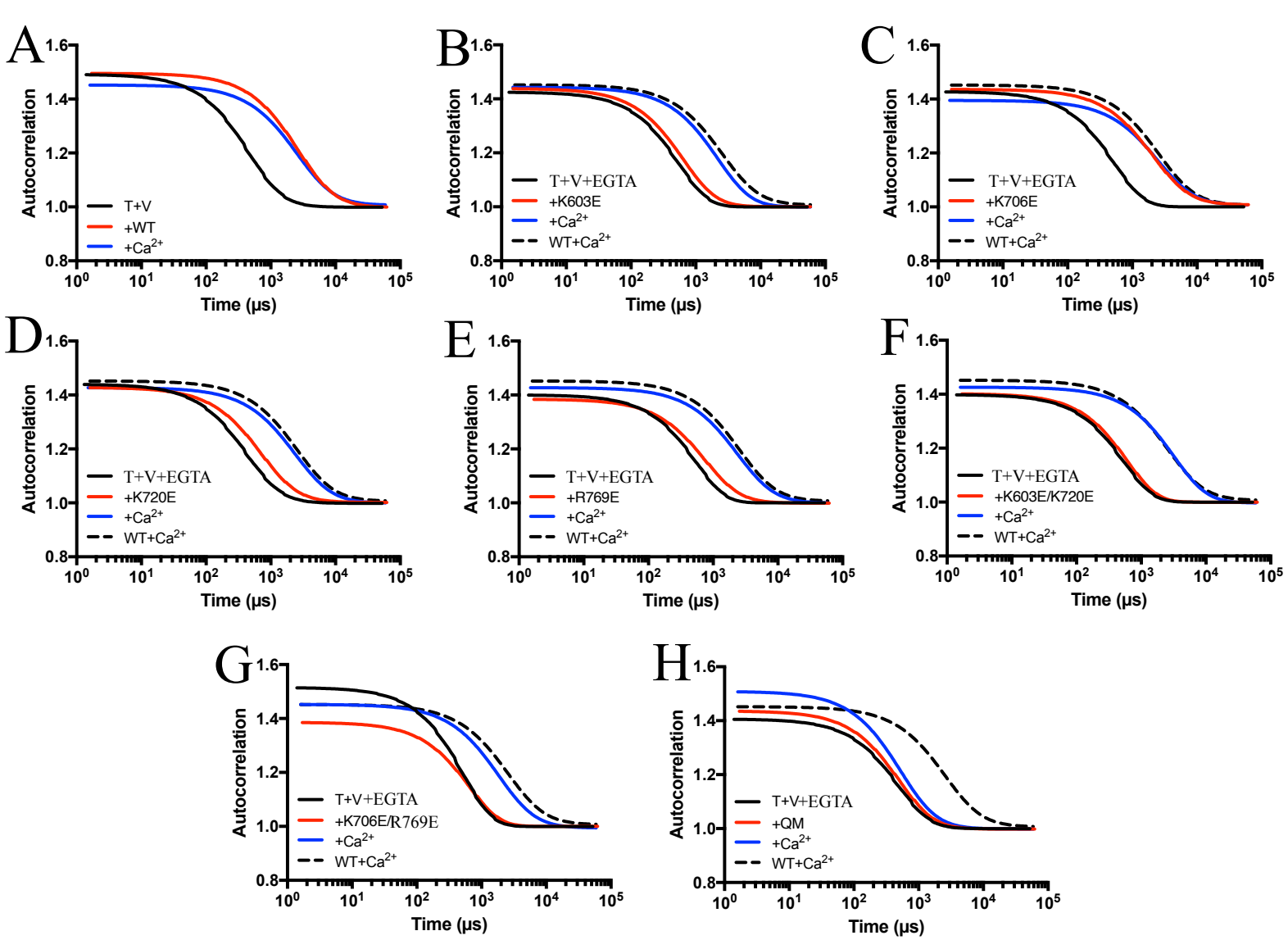

Figure 5.2 Dynamic light scattering analysis of clustering by various $C_1C_2BMUNC_2C$ mutants suggests distinct calcium-independent and calcium-dependent membrane binding sites

Clustering of protein free liposomes with plasma membrane and synaptic vesicle composition was monitored by dynamic light scattering in the presence of various $C_1C_2BMUNC_2C$ mutants. A shift to the right in the autocorrelation curve represents an increase in vesicle clustering. Wild-type $C_1C_2BMUNC_2C$ (A) fully clusters independent of calcium. Interface 1 mutants (B,D,F) abolish protein-dependent clustering until calcium is added. Calcium-dependent mutants (C,E,G) have mixed effects with the R769E mutant abolishing protein-dependent clustering and the K706E mutant having no impact on clustering as expect. The K603E/K706E/K720E/R769E mutant (H, labeled QM for quadruple mutant) significantly reduces protein-dependent and calcium-dependent clustering.

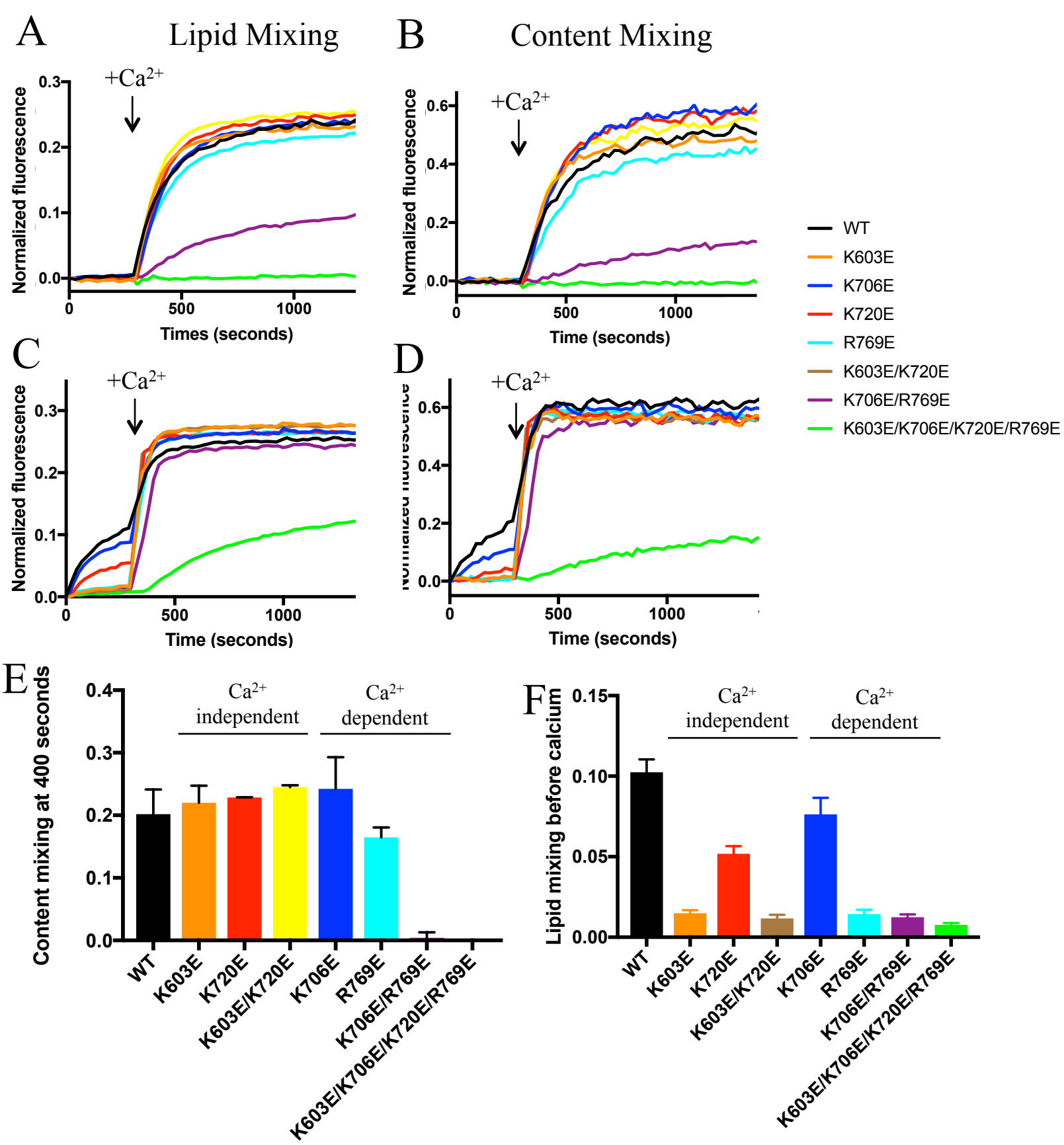

Figure 5.3 Mutations in the calcium-dependent and calcium-independent membrane binding faces reduce fusion efficiency in the corresponding phases of reconstitutions

Lipid and content mixing assays for the standard full-system reconstitution (A,B) and for reconstitutions with D326K mutant Munc18-1 (C,D) show dramatic effects on calcium-dependent and calcium-independent fusion, as expected. Content mixing shortly after calcium addition was quantified by triplicate experiments performed with one set of liposomes (E). Lipid mixing before calcium was quantified for the D326K mutant Munc18-1 reconstitutions by triplicate experiments performed with one preparation of liposomes (F).

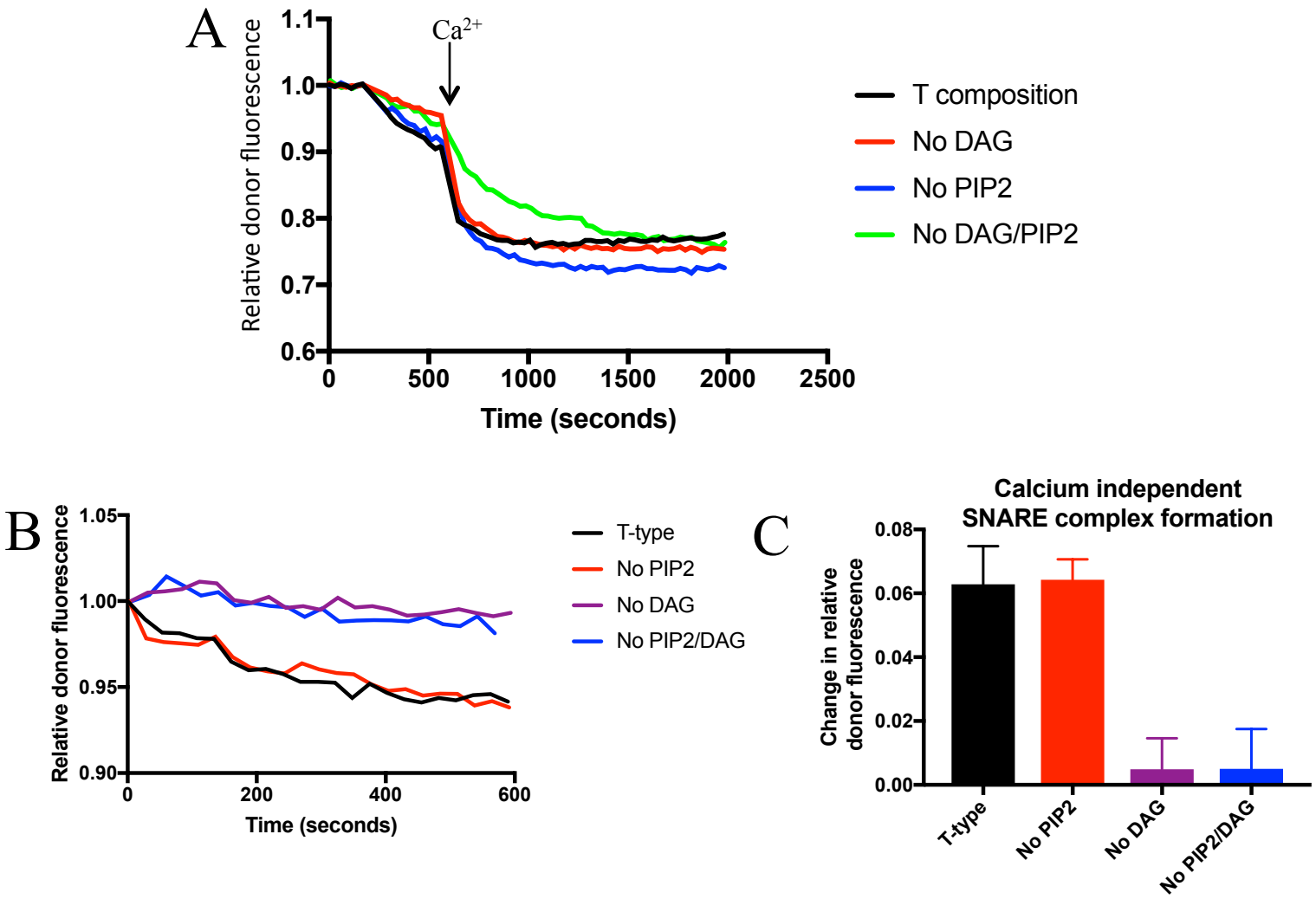

Figure 5.4 Removing PIP_2 and DAG from liposomes reduces calcium-dependent SNARE complex formation while DAG removal decreases calcium-independent SNARE complex formation

(A) SNARE assembly was monitored as a function of time in the presence of V-liposomes containing synaptobrevin and synaptotagmin, T-liposomes containing syntaxin and SNAP-25, Munc18, NSF, α-SNAP, and $C_1C_2BMUNC_2C$. The decrease in donor fluorescence due to FRET was used to monitor SNARE complex formation. Removal of DAG and PIP_2 from T-liposomes significantly reduces the rate of calcium-dependent SNARE complex formation. (B) Using the same assay, but with V-liposomes containing synaptobrevin only, there is a significant decrease in calcium-independent formation of SNARE complex upon removal of DAG from the membrane. (C) Quantification of the amount of SNARE complex formed at 600 seconds was done using triplicate experiments from the same preparation.

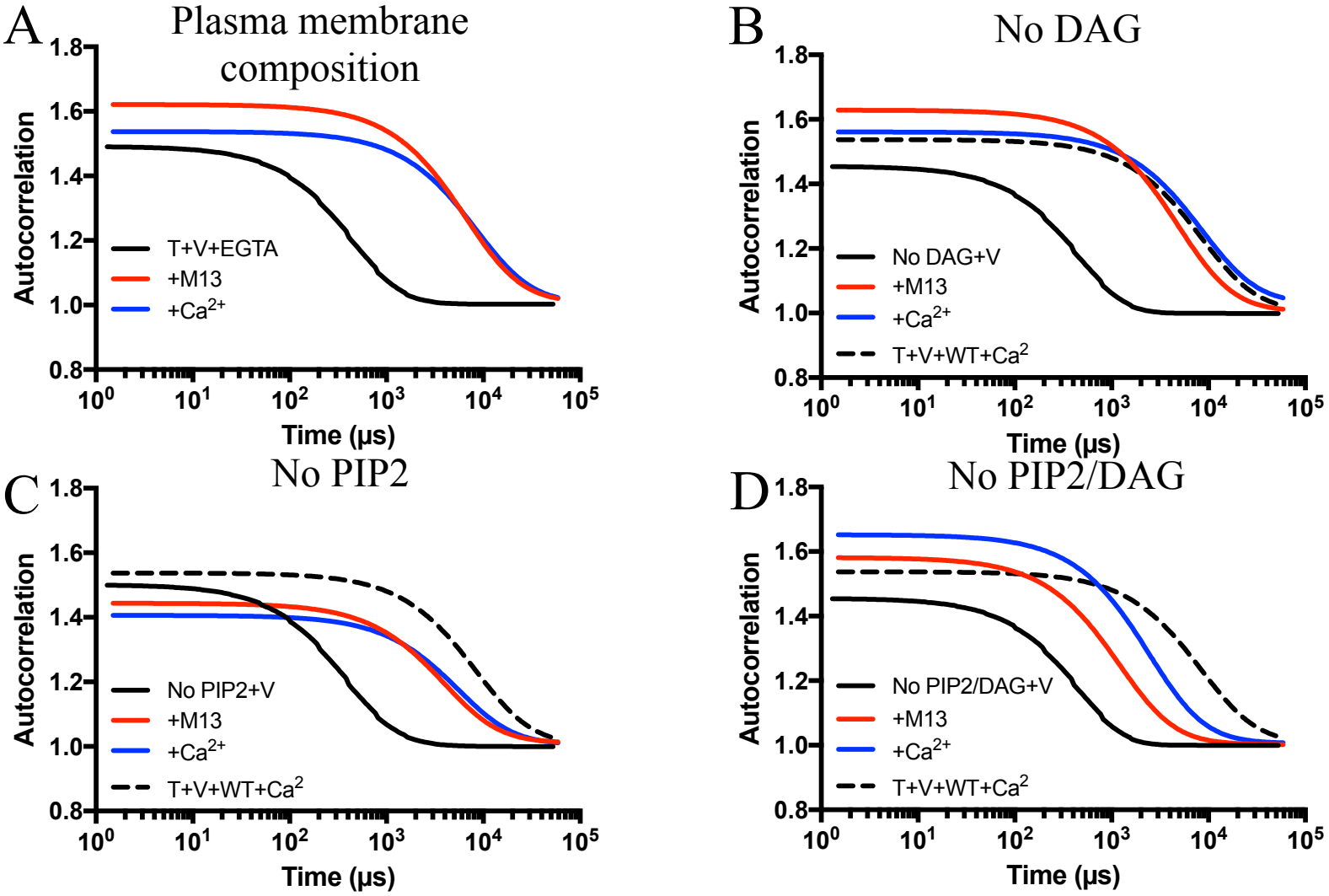

Figure 5.5 Removing DAG has minimal impact on the ability of $C_1C_2BMUNC_2$ to cluster liposomes with synaptic vesicle and plasma membrane composition while removing PIP_2 or both decreases clustering

Clustering of protein free liposomes with synaptic vesicle composition and the noted composition was monitored by dynamic light scattering. A shift to the right in the autocorrelation curve represents an increase in vesicle clustering. As expected, $C_1C_2BMUNC_2$ clusters standard plasma membrane composition liposomes containing PIP_2 and DAG with synaptic vesicle composition (A), while liposomes lacking PIP_2 or both PIP_2 and DAG cluster less (C and D respectively). DAG removal has a negligible impact on clustering (B).

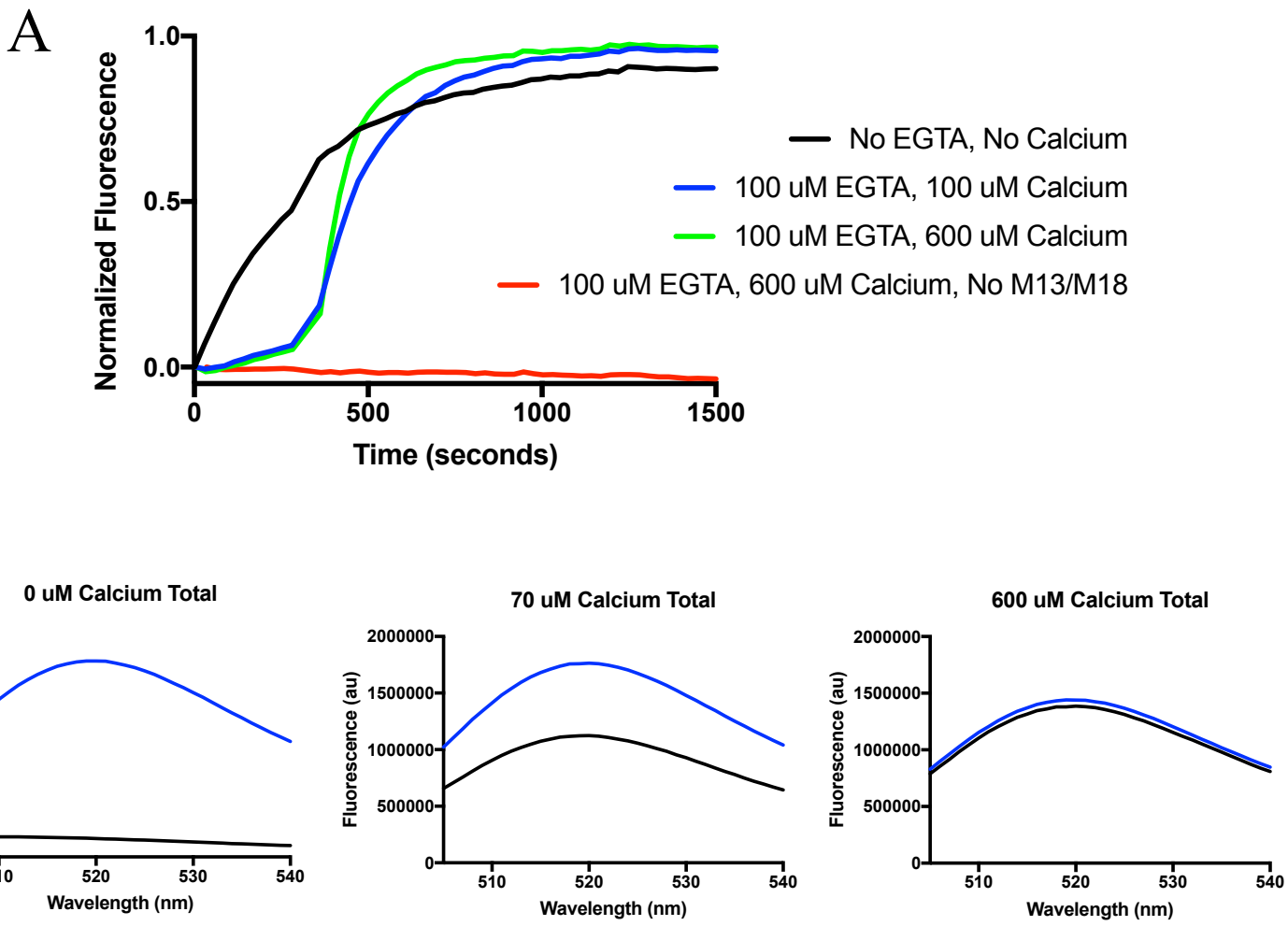

Figure 5.6 Maximum lipid mixing between plasma membrane and synaptic vesicle composition liposomes occurs with micromolar concentrations of calcium and Fluo-4 fluorescence changes based on the calcium concentration
Standard fusion assays were performed with T-liposomes containing syntaxin-1 and SNAP-25, V-liposomes containing synaptobrevin-2, Munc18-1, NSF, α-SNAP, and C_1C_2BMUNC_2C and dequenching of membrane-bound DiD was monitored as a proxy for lipid mixing. (A) Lipid mixing occurs readily with no EGTA and no calcium (black curve) while no lipid mixing is observed in samples containing 100 μM EGTA until 100 μM (blue curve) or 600 μM (green curve) calcium is added. (B) Examples of Fluo-4 wavelength scans from reconstitution samples containing the noted quantity of calcium (black curve) or with 5 mM calcium (blue curve).

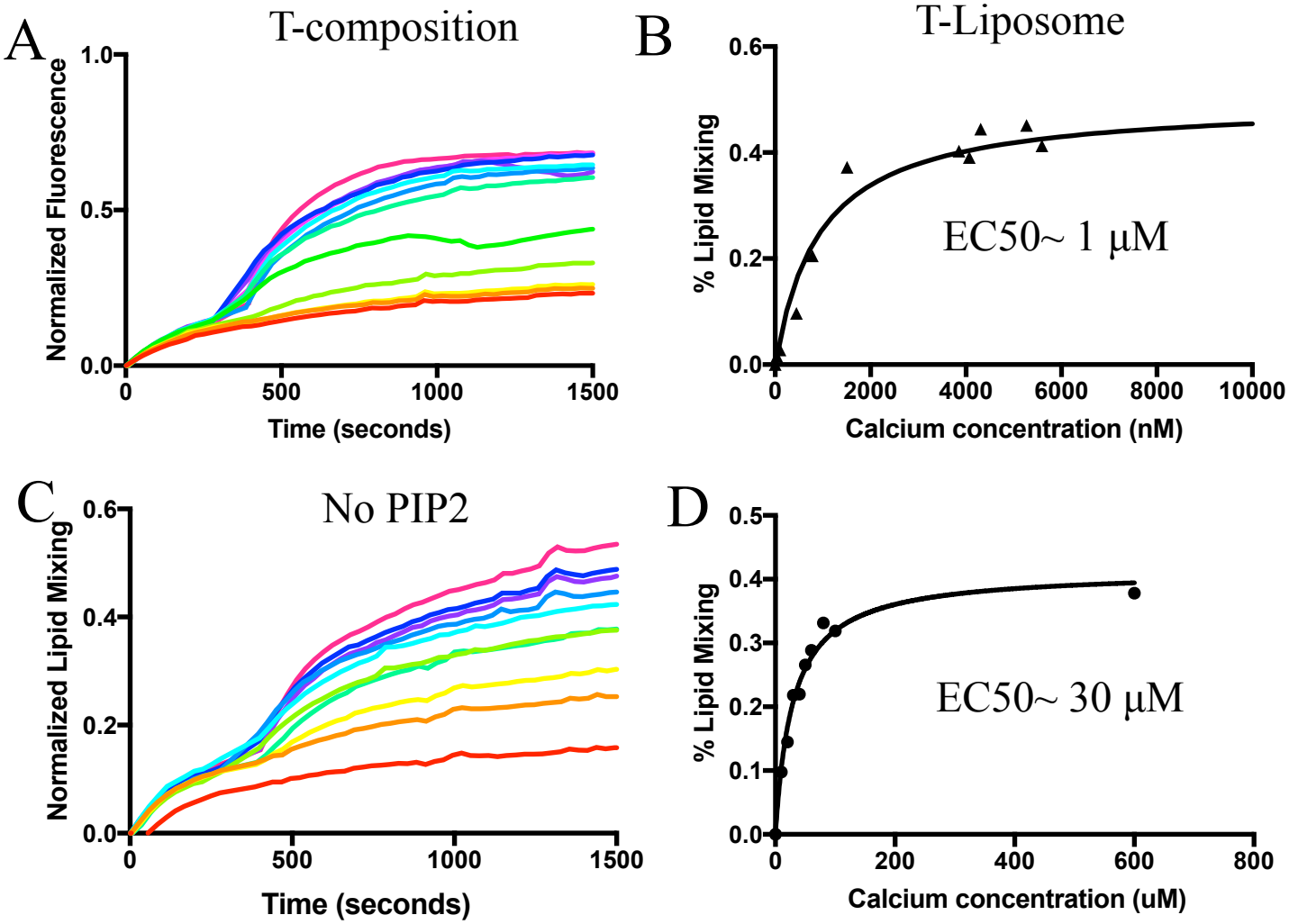

Figure 5.7 The EC50 for $C_1C_2BMUNC_2C$-mediated calcium-dependent fusion is ~1 μM and is dramatically increased by PIP2

Standard fusion assays were performed with T-liposomes containing syntaxin-1 and SNAP-25, V-liposomes containing synaptobrevin-2, Munc18-1, NSF, α-SNAP, and $C_1C_2BMUNC_2C$. Time-dependent dequenching of membrane-bound DiD was monitored as a readout for lipid mixing (A). Increasing concentrations of calcium stimulated fusion and the concentration was measured using a fluorescent probe. Percent of lipid mixing was plotted against calcium concentration and fit with a nonlinear regression using a one site specific binding model to get an EC50 of ~1 μM (B). The same experiment was performed with the removal of PIP2 from the T-composition membrane (C) and the EC50 for calcium was decreased thirty-fold (D).

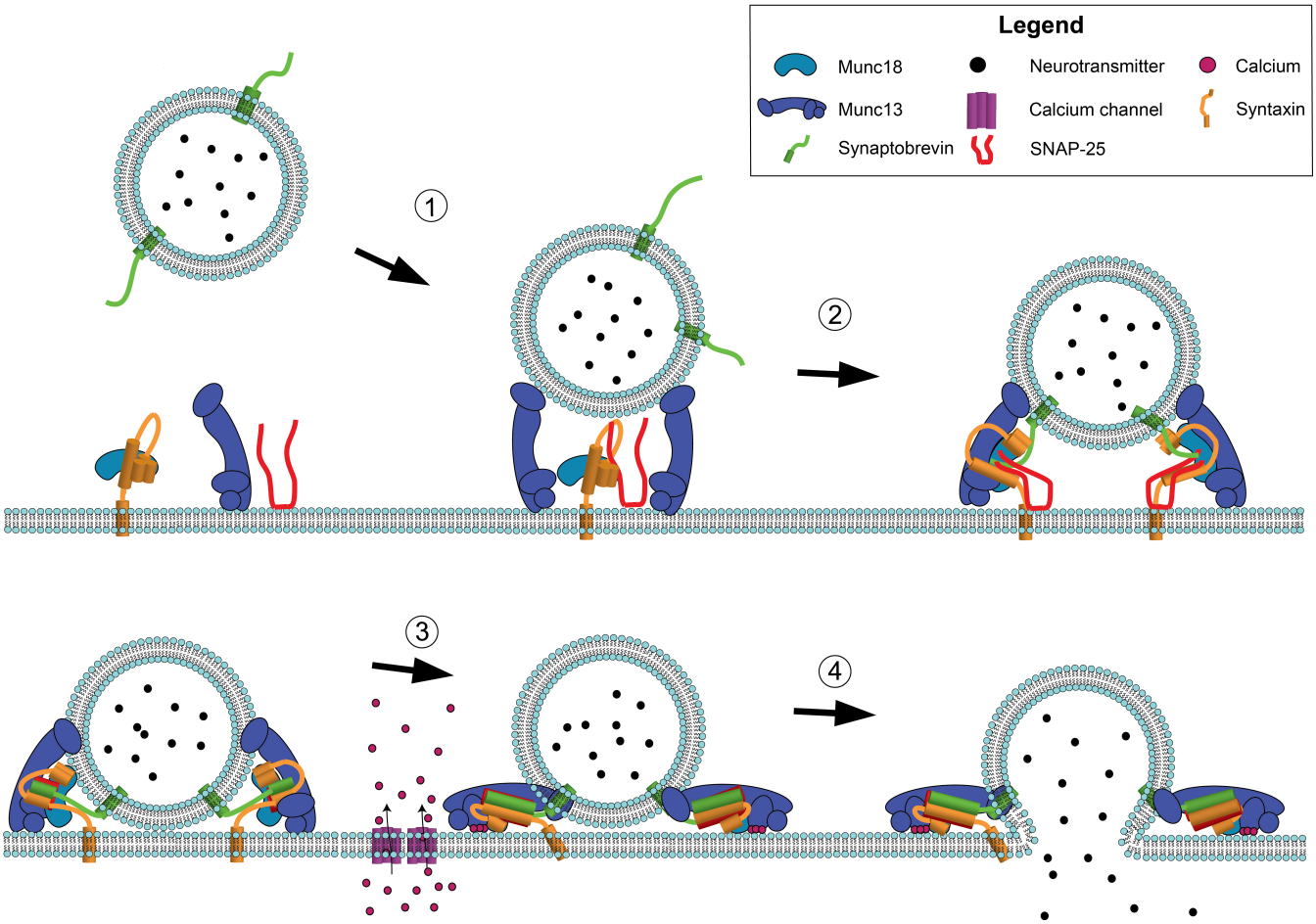

Figure 5.8 A model for Munc13-1-mediated presynaptic plasticity
Munc13-1 in the active zone docks the synaptic vesicle to the plasma membrane (1) and spaces the membranes apart so that the SNARE complex cannot form. DAG in the plasma membrane or residual calcium in the axon terminal reorient Munc13 so that the SNAREs can engage and the N-terminus of the SNARE complex can begin to form on Munc18 (2). Elevated concentrations of calcium or low calcium concentrations coupled with high PIP_2 levels will favor a tilted orientation that brings the membranes closer together enabling folding of the SNARE complex (3) and fusion (4).

CHAPTER 6-Future Directions

Over the years, many *in vivo* and *in vitro* assays have established the essential nature of Munc13-1 in synaptic vesicle fusion. In the early days it was thought that the main role of Munc13-1 is opening syntaxin-1 and catalyzing the formation of the SNARE complex, but over time Munc13-1 has been shown to be involved in various stages of the synaptic vesicle cycle. This dissertation provides additional insights into the role of Munc13-1 in fusion by establishing the physiological relevance of vesicle docking by Munc13-1 and is providing the basis for understanding the molecular mechanisms driving Munc13-1-dependent presynaptic plasticity. While these experiments have provided many valuable insights into the Munc13 family, they leave more unanswered than answered questions.

One of the keys to understanding the molecular basis for the function of Munc13-1 in synaptic vesicle fusion will come from structural studies of large fragments including the entire highly conserved C-terminal $C_1C_2BMUNC_2C$ fragment. As it stands, there is no structure of the C_2C domain, $C_1C_2BMUNC_2C$, or of the full-length Munc13-1. A structure including C2C and the adjacent MUN domain or another similar fragment would provide the orientation of the membrane binding loops of C_2C relative to the MUN domain, enabling prediction of a more accurate membrane bridging distance and orientation. A full-length Munc13-1 structure including C_2A would be even more informative and would facilitate understanding the molecular basis by which C_2A homodimerization inhibits Munc13-1-dependent neurotransmitter release. Once a full-length Munc13-1 protein is available for structural studies, an obvious next step would be adding full-length Munc13-1 to reconstitution systems to see if C_2A homodimerization is sufficient to inhibit fusion. From here, adding additional components to the reconstitution and

attempting to create a synthetic active zone would yield tremendous insights into presynaptic organization and vesicle trafficking. Since Munc13-1 forms a tight complex with RIMs and RAB3a, these would be additional components worth adding in early stages.

While chapter 5 helps to pave the way to understanding Munc13-1-dependent presynaptic plasticity, none of the experiments fully validate the hypothesis put forth. The major missing piece is visual evidence that C_1C_2BMUNC_2C undergoes a membrane reorientation. Ideally, we can use cryo-electron tomography to visualize reconstitution samples or samples with C_1C_2BMUNC_2C with plasma membrane composition vesicles to see if there is a reorientation in the presence of different ligands. This would provide irrefutable evidence that this reorientation happens and this, coupled with the other assays performed, suggests that reorientation underlies the ability of Munc13-1 to regulate presynaptic plasticity. We also need to validate the various mutants by studying them *in vivo* using electrophysiology. If the reconstitution and electrophysiology are consistent, it provides much stronger evidence in support of the reorientation hypothesis and broadens the implications of this hypothesis. This work is ongoing in the lab and in our collaborators lab and with time we hope to fully understand the role of Munc13-1 in presynaptic plasticity.

BIBLIOGRAPHY

ABUL-HUSN, N. S., BUSHLIN, I., MORON, J. A., JENKINS, S. L., DOLIOS, G., WANG, R., IYENGAR, R., MA'AYAN, A. & DEVI, L. A. 2009. Systems approach to explore components and interactions in the presynapse. *Proteomics,* 9**,** 3303-15.

ARAC, D., CHEN, X., KHANT, H. A., UBACH, J., LUDTKE, S. J., KIKKAWA, M., JOHNSON, A. E., CHIU, W., SUDHOF, T. C. & RIZO, J. 2006. Close membrane-membrane proximity induced by Ca(2+)-dependent multivalent binding of synaptotagmin-1 to phospholipids. *Nat Struct Mol Biol,* 13**,** 209-17.

ARANCILLO, M., MIN, S. W., GERBER, S., MUNSTER-WANDOWSKI, A., WU, Y. J., HERMAN, M., TRIMBUCH, T., RAH, J. C., AHNERT-HILGER, G., RIEDEL, D., SUDHOF, T. C. & ROSENMUND, C. 2013. Titration of Syntaxin1 in mammalian synapses reveals multiple roles in vesicle docking, priming, and release probability. *J Neurosci,* 33**,** 16698-714.

AUGUSTIN, I., ROSENMUND, C., SUDHOF, T. C. & BROSE, N. 1999. Munc13-1 is essential for fusion competence of glutamatergic synaptic vesicles. *Nature,* 400**,** 457-61.

BAI, J., TUCKER, W. C. & CHAPMAN, E. R. 2004. PIP2 increases the speed of response of synaptotagmin and steers its membrane-penetration activity toward the plasma membrane. *Nat Struct Mol Biol,* 11**,** 36-44.

BAKER, R. W., JEFFREY, P. D., ZICK, M., PHILLIPS, B. P., WICKNER, W. T. & HUGHSON, F. M. 2015. A direct role for the Sec1/Munc18-family protein Vps33 as a template for SNARE assembly. *Science,* 349**,** 1111-4.

BASU, J., BETZ, A., BROSE, N. & ROSENMUND, C. 2007. Munc13-1 C1 domain activation lowers the energy barrier for synaptic vesicle fusion. *J Neurosci,* 27**,** 1200-10.

BASU, J., SHEN, N., DULUBOVA, I., LU, J., GUAN, R., GURYEV, O., GRISHIN, N. V., ROSENMUND, C. & RIZO, J. 2005. A minimal domain responsible for Munc13 activity. *Nat Struct Mol Biol,* 12**,** 1017-8.

BETZ, A., ASHERY, U., RICKMANN, M., AUGUSTIN, I., NEHER, E., SUDHOF, T. C., RETTIG, J. & BROSE, N. 1998. Munc13-1 is a presynaptic phorbol ester receptor that enhances neurotransmitter release. *Neuron,* 21**,** 123-36.

BETZ, A., OKAMOTO, M., BENSELER, F. & BROSE, N. 1997. Direct interaction of the rat unc-13 homologue Munc13-1 with the N terminus of syntaxin. *J Biol Chem,* 272**,** 2520-6.

BETZ, A., THAKUR, P., JUNGE, H. J., ASHERY, U., RHEE, J. S., SCHEUSS, V., ROSENMUND, C., RETTIG, J. & BROSE, N. 2001. Functional interaction of the active zone proteins Munc13-1 and RIM1 in synaptic vesicle priming. *Neuron,* 30**,** 183-96.

BETZ, W. J. 1970. Depression of transmitter release at the neuromuscular junction of the frog. *J Physiol,* 206**,** 629-44.

BRENNER, S. 1974. The genetics of Caenorhabditis elegans. *Genetics,* 77**,** 71-94.

BREWER, K. D., BACAJ, T., CAVALLI, A., CAMILLONI, C., SWARBRICK, J. D., LIU, J., ZHOU, A., ZHOU, P., BARLOW, N., XU, J., SEVEN, A. B., PRINSLOW, E. A., VOLETI, R., HAUSSINGER, D., BONVIN, A. M., TOMCHICK, D. R., VENDRUSCOLO, M., GRAHAM, B., SUDHOF, T. C. & RIZO, J. 2015. Dynamic binding mode of a Synaptotagmin-1-SNARE complex in solution. *Nat Struct Mol Biol,* 22**,** 555-64.

BROSE, N., HOFMANN, K., HATA, Y. & SUDHOF, T. C. 1995. Mammalian homologues of Caenorhabditis elegans unc-13 gene define novel family of C2-domain proteins. *J Biol Chem,* 270**,** 25273-80.

BROSE, N., PETRENKO, A. G., SUDHOF, T. C. & JAHN, R. 1992. Synaptotagmin: a calcium sensor on the synaptic vesicle surface. *Science,* 256**,** 1021-5.

BRUNGER, A. T., CHOI, U. B., LAI, Y., LEITZ, J. & ZHOU, Q. 2018. Molecular Mechanisms of Fast Neurotransmitter Release. *Annu Rev Biophys,* 47**,** 469-497.

BURKHARDT, P., HATTENDORF, D. A., WEIS, W. I. & FASSHAUER, D. 2008. Munc18a controls SNARE assembly through its interaction with the syntaxin N-peptide. *EMBO J,* 27**,** 923-33.

CAMACHO, M., BASU, J., TRIMBUCH, T., CHANG, S., PULIDO-LOZANO, C., CHANG, S. S., DULUVOVA, I., ABO-RADY, M., RIZO, J. & ROSENMUND, C. 2017. Heterodimerization of Munc13 C2A domain with RIM regulates synaptic vesicle docking and priming. *Nat Commun,* 8**,** 15293.

CARRASCO, S. & MERIDA, I. 2007. Diacylglycerol, when simplicity becomes complex. *Trends Biochem Sci,* 32**,** 27-36.

CASTILLO, P. E., JANZ, R., SUDHOF, T. C., TZOUNOPOULOS, T., MALENKA, R. C. & NICOLL, R. A. 1997. Rab3A is essential for mossy fibre long-term potentiation in the hippocampus. *Nature,* 388**,** 590-3.

CASTILLO, P. E., SCHOCH, S., SCHMITZ, F., SUDHOF, T. C. & MALENKA, R. C. 2002. RIM1alpha is required for presynaptic long-term potentiation. *Nature,* 415**,** 327-30.

CECCARELLI, B., HURLBUT, W. P. & MAURO, A. 1973. Turnover of transmitter and synaptic vesicles at the frog neuromuscular junction. *J Cell Biol,* 57**,** 499-524.

CHANADAY, N. L. & KAVALALI, E. T. 2017. How do you recognize and reconstitute a synaptic vesicle after fusion? *F1000Res,* 6**,** 1734.

CHANG, S., TRIMBUCH, T. & ROSENMUND, C. 2018. Synaptotagmin-1 drives synchronous Ca(2+)-triggered fusion by C2B-domain-mediated synaptic-vesicle-membrane attachment. *Nat Neurosci,* 21**,** 33-40.

CHAPMAN, E. R. & DAVIS, A. F. 1998. Direct interaction of a Ca2+-binding loop of synaptotagmin with lipid bilayers. *J Biol Chem,* 273**,** 13995-4001.

CHEN, X., ARAC, D., WANG, T. M., GILPIN, C. J., ZIMMERBERG, J. & RIZO, J. 2006. SNARE-mediated lipid mixing depends on the physical state of the vesicles. *Biophys J,* 90**,** 2062-74.

CHEN, X., LU, J., DULUBOVA, I. & RIZO, J. 2008. NMR analysis of the closed conformation of syntaxin-1. *J Biomol NMR,* 41**,** 43-54.

CHEN, Y. A. & SCHELLER, R. H. 2001. SNARE-mediated membrane fusion. *Nat Rev Mol Cell Biol,* 2**,** 98-106.

CITRI, A. & MALENKA, R. C. 2008. Synaptic plasticity: multiple forms, functions, and mechanisms. *Neuropsychopharmacology,* 33**,** 18-41.
CLARY, D. O., GRIFF, I. C. & ROTHMAN, J. E. 1990. SNAPs, a family of NSF attachment proteins involved in intracellular membrane fusion in animals and yeast. *Cell,* 61**,** 709-21.
CREMONA, O. & DE CAMILLI, P. 2001. Phosphoinositides in membrane traffic at the synapse. *J Cell Sci,* 114**,** 1041-52.
DELAGLIO, F., GRZESIEK, S., VUISTER, G. W., ZHU, G., PFEIFER, J. & BAX, A. 1995. NMRPipe: a multidimensional spectral processing system based on UNIX pipes. *J Biomol NMR,* 6**,** 277-93.
DENG, L., KAESER, P. S., XU, W. & SUDHOF, T. C. 2011. RIM proteins activate vesicle priming by reversing autoinhibitory homodimerization of Munc13. *Neuron,* 69**,** 317-31.
DULUBOVA, I., KHVOTCHEV, M., LIU, S., HURYEVA, I., SUDHOF, T. C. & RIZO, J. 2007. Munc18-1 binds directly to the neuronal SNARE complex. *Proc Natl Acad Sci U S A,* 104**,** 2697-702.
DULUBOVA, I., LOU, X., LU, J., HURYEVA, I., ALAM, A., SCHNEGGENBURGER, R., SUDHOF, T. C. & RIZO, J. 2005. A Munc13/RIM/Rab3 tripartite complex: from priming to plasticity? *EMBO J,* 24**,** 2839-50.
DULUBOVA, I., SUGITA, S., HILL, S., HOSAKA, M., FERNANDEZ, I., SUDHOF, T. C. & RIZO, J. 1999. A conformational switch in syntaxin during exocytosis: role of munc18. *EMBO J,* 18**,** 4372-82.
EBERHARD, D. A., COOPER, C. L., LOW, M. G. & HOLZ, R. W. 1990. Evidence that the inositol phospholipids are necessary for exocytosis. Loss of inositol phospholipids and inhibition of secretion in permeabilized cells caused by a bacterial phospholipase C and removal of ATP. *Biochem J,* 268**,** 15-25.
EBERHARD, D. A. & HOLZ, R. W. 1991. Calcium promotes the accumulation of polyphosphoinositides in intact and permeabilized bovine adrenal chromaffin cells. *Cell Mol Neurobiol,* 11**,** 357-70.
FASSHAUER, D., SUTTON, R. B., BRUNGER, A. T. & JAHN, R. 1998. Conserved structural features of the synaptic fusion complex: SNARE proteins reclassified as Q- and R-SNAREs. *Proc Natl Acad Sci U S A,* 95**,** 15781-6.
FERNANDEZ-CHACON, R., KONIGSTORFER, A., GERBER, S. H., GARCIA, J., MATOS, M. F., STEVENS, C. F., BROSE, N., RIZO, J., ROSENMUND, C. & SUDHOF, T. C. 2001. Synaptotagmin I functions as a calcium regulator of release probability. *Nature,* 410**,** 41-9.
FERNANDEZ, I., ARAC, D., UBACH, J., GERBER, S. H., SHIN, O., GAO, Y., ANDERSON, R. G., SUDHOF, T. C. & RIZO, J. 2001. Three-dimensional structure of the synaptotagmin 1 C2B-domain: synaptotagmin 1 as a phospholipid binding machine. *Neuron,* 32**,** 1057-69.
FERNANDEZ, I., UBACH, J., DULUBOVA, I., ZHANG, X., SUDHOF, T. C. & RIZO, J. 1998. Three-dimensional structure of an evolutionarily conserved N-terminal domain of syntaxin 1A. *Cell,* 94**,** 841-9.

GAD, H., LOW, P., ZOTOVA, E., BRODIN, L. & SHUPLIAKOV, O. 1998. Dissociation between Ca2+-triggered synaptic vesicle exocytosis and clathrin-mediated endocytosis at a central synapse. *Neuron,* 21**,** 607-16.

GENGYO-ANDO, K., KAMIYA, Y., YAMAKAWA, A., KODAIRA, K., NISHIWAKI, K., MIWA, J., HORI, I. & HOSONO, R. 1993. The C. elegans unc-18 gene encodes a protein expressed in motor neurons. *Neuron,* 11**,** 703-11.

GEPPERT, M., GODA, Y., HAMMER, R. E., LI, C., ROSAHL, T. W., STEVENS, C. F. & SUDHOF, T. C. 1994. Synaptotagmin I: a major Ca2+ sensor for transmitter release at a central synapse. *Cell,* 79**,** 717-27.

GILLESPIE, J. R. & SHORTLE, D. 1997. Characterization of long-range structure in the denatured state of staphylococcal nuclease. II. Distance restraints from paramagnetic relaxation and calculation of an ensemble of structures. *J Mol Biol,* 268**,** 170-84.

GRYNKIEWICZ, G., POENIE, M. & TSIEN, R. Y. 1985. A new generation of Ca2+ indicators with greatly improved fluorescence properties. *J Biol Chem,* 260**,** 3440-50.

GUAN, R., DAI, H. & RIZO, J. 2008. Binding of the Munc13-1 MUN domain to membrane-anchored SNARE complexes. *Biochemistry,* 47**,** 1474-81.

GUAN, R., DAI, H., TOMCHICK, D. R., DULUBOVA, I., MACHIUS, M., SUDHOF, T. C. & RIZO, J. 2007. Crystal structure of the RIM1alpha C2B domain at 1.7 A resolution. *Biochemistry,* 46**,** 8988-98.

HAGEN, W. J. H., WAN, W. & BRIGGS, J. A. G. 2017. Implementation of a cryo-electron tomography tilt-scheme optimized for high resolution subtomogram averaging. *J Struct Biol,* 197**,** 191-198.

HANSON, P. I., ROTH, R., MORISAKI, H., JAHN, R. & HEUSER, J. E. 1997. Structure and conformational changes in NSF and its membrane receptor complexes visualized by quick-freeze/deep-etch electron microscopy. *Cell,* 90**,** 523-35.

HATA, Y., SLAUGHTER, C. A. & SUDHOF, T. C. 1993. Synaptic vesicle fusion complex contains unc-18 homologue bound to syntaxin. *Nature,* 366**,** 347-51.

HEUSER, J. E. & REESE, T. S. 1973. Evidence for recycling of synaptic vesicle membrane during transmitter release at the frog neuromuscular junction. *J Cell Biol,* 57**,** 315-44.

HONG, W. & LEV, S. 2014. Tethering the assembly of SNARE complexes. *Trends Cell Biol,* 24**,** 35-43.

HOOPMANN, P., PUNGE, A., BARYSCH, S. V., WESTPHAL, V., BUCKERS, J., OPAZO, F., BETHANI, I., LAUTERBACH, M. A., HELL, S. W. & RIZZOLI, S. O. 2010. Endosomal sorting of readily releasable synaptic vesicles. *Proc Natl Acad Sci U S A,* 107**,** 19055-60.

HOSONO, R. & KAMIYA, Y. 1991. Additional genes which result in an elevation of acetylcholine levels by mutations in Caenorhabditis elegans. *Neurosci Lett,* 128**,** 243-4.

HOSONO, R., SASSA, T. & KUNO, S. 1987. Mutations affecting acetylcholine levels in the nematode Caenorhabditis elegans. *J Neurochem,* 49**,** 1820-3.

IANCU, C. V., TIVOL, W. F., SCHOOLER, J. B., DIAS, D. P., HENDERSON, G. P., MURPHY, G. E., WRIGHT, E. R., LI, Z., YU, Z., BRIEGEL, A., GAN, L., HE, Y. & JENSEN, G. J. 2006. Electron cryotomography sample preparation using the Vitrobot. *Nat Protoc,* 1**,** 2813-9.

IMIG, C., MIN, S. W., KRINNER, S., ARANCILLO, M., ROSENMUND, C., SUDHOF, T. C., RHEE, J., BROSE, N. & COOPER, B. H. 2014. The morphological and molecular nature of synaptic vesicle priming at presynaptic active zones. *Neuron,* 84**,** 416-31.

JAMES, D. J., KOWALCHYK, J., DAILY, N., PETRIE, M. & MARTIN, T. F. 2009. CAPS drives trans-SNARE complex formation and membrane fusion through syntaxin interactions. *Proc Natl Acad Sci U S A,* 106**,** 17308-13.

JOHNSON, B. A. & BLEVINS, R. A. 1994. NMR View: A computer program for the visualization and analysis of NMR data. *J Biomol NMR,* 4**,** 603-14.

JUNGE, H. J., RHEE, J. S., JAHN, O., VAROQUEAUX, F., SPIESS, J., WAXHAM, M. N., ROSENMUND, C. & BROSE, N. 2004. Calmodulin and Munc13 form a Ca2+ sensor/effector complex that controls short-term synaptic plasticity. *Cell,* 118**,** 389-401.

KABACHINSKI, G., YAMAGA, M., KIELAR-GREVSTAD, D. M., BRUINSMA, S. & MARTIN, T. F. 2014. CAPS and Munc13 utilize distinct PIP2-linked mechanisms to promote vesicle exocytosis. *Mol Biol Cell,* 25**,** 508-21.

KATZ, B. & MILEDI, R. 1967. A study of synaptic transmission in the absence of nerve impulses. *J Physiol,* 192**,** 407-36.

KHVOTCHEV, M., DULUBOVA, I., SUN, J., DAI, H., RIZO, J. & SUDHOF, T. C. 2007. Dual modes of Munc18-1/SNARE interactions are coupled by functionally critical binding to syntaxin-1 N terminus. *J Neurosci,* 27**,** 12147-55.

KIM, J. H., LEE, S. R., LI, L. H., PARK, H. J., PARK, J. H., LEE, K. Y., KIM, M. K., SHIN, B. A. & CHOI, S. Y. 2011. High cleavage efficiency of a 2A peptide derived from porcine teschovirus-1 in human cell lines, zebrafish and mice. *PLoS One,* 6**,** e18556.

KREMER, J. R., MASTRONARDE, D. N. & MCINTOSH, J. R. 1996. Computer visualization of three-dimensional image data using IMOD. *J Struct Biol,* 116**,** 71-6.

KREUTZBERGER, A. J. B., KIESSLING, V., LIANG, B., SEELHEIM, P., JAKHANWAL, S., JAHN, R., CASTLE, J. D. & TAMM, L. K. 2017. Reconstitution of calcium-mediated exocytosis of dense-core vesicles. *Sci Adv,* 3**,** e1603208.

LAI, Y., CHOI, U. B., LEITZ, J., RHEE, H. J., LEE, C., ALTAS, B., ZHAO, M., PFUETZNER, R. A., WANG, A. L., BROSE, N., RHEE, J. & BRUNGER, A. T. 2017. Molecular Mechanisms of Synaptic Vesicle Priming by Munc13 and Munc18. *Neuron,* 95**,** 591-607 e10.

LEITNER, A., FAINI, M., STENGEL, F. & AEBERSOLD, R. 2016. Crosslinking and Mass Spectrometry: An Integrated Technology to Understand the Structure and Function of Molecular Machines. *Trends Biochem Sci,* 41**,** 20-32.

LI, L., SHIN, O. H., RHEE, J. S., ARAC, D., RAH, J. C., RIZO, J., SUDHOF, T. & ROSENMUND, C. 2006. Phosphatidylinositol phosphates as co-activators of Ca2+ binding to C2 domains of synaptotagmin 1. *J Biol Chem,* 281**,** 15845-52.

LI, W., MA, C., GUAN, R., XU, Y., TOMCHICK, D. R. & RIZO, J. 2011. The crystal structure of a Munc13 C-terminal module exhibits a remarkable similarity to vesicle tethering factors. *Structure,* 19**,** 1443-55.

LINK, E., EDELMANN, L., CHOU, J. H., BINZ, T., YAMASAKI, S., EISEL, U., BAUMERT, M., SUDHOF, T. C., NIEMANN, H. & JAHN, R. 1992. Tetanus toxin action: inhibition of neurotransmitter release linked to synaptobrevin proteolysis. *Biochem Biophys Res Commun,* 189**,** 1017-23.

LIU, X., SEVEN, A. B., CAMACHO, M., ESSER, V., XU, J., TRIMBUCH, T., QUADE, B., SU, L., MA, C., ROSENMUND, C. & RIZO, J. 2016. Functional synergy between the Munc13 C-terminal C1 and C2 domains. *Elife,* 5.

LIU, X., SEVEN, A. B., XU, J., ESSER, V., SU, L., MA, C. & RIZO, J. 2017. Simultaneous lipid and content mixing assays for in vitro reconstitution studies of synaptic vesicle fusion. *Nat Protoc,* 12**,** 2014-2028.

LOIS, C., HONG, E. J., PEASE, S., BROWN, E. J. & BALTIMORE, D. 2002. Germline transmission and tissue-specific expression of transgenes delivered by lentiviral vectors. *Science,* 295**,** 868-72.

LU, J., MACHIUS, M., DULUBOVA, I., DAI, H., SUDHOF, T. C., TOMCHICK, D. R. & RIZO, J. 2006. Structural basis for a Munc13-1 homodimer to Munc13-1/RIM heterodimer switch. *PLoS Biol,* 4**,** e192.

MA, C., LI, W., XU, Y. & RIZO, J. 2011. Munc13 mediates the transition from the closed syntaxin-Munc18 complex to the SNARE complex. *Nat Struct Mol Biol,* 18**,** 542-9.

MA, C., SU, L., SEVEN, A. B., XU, Y. & RIZO, J. 2013. Reconstitution of the vital functions of Munc18 and Munc13 in neurotransmitter release. *Science,* 339**,** 421-5.

MADISON, J. M., NURRISH, S. & KAPLAN, J. M. 2005. UNC-13 interaction with syntaxin is required for synaptic transmission. *Curr Biol,* 15**,** 2236-42.

MARTIN, T. F. 1998. Phosphoinositide lipids as signaling molecules: common themes for signal transduction, cytoskeletal regulation, and membrane trafficking. *Annu Rev Cell Dev Biol,* 14**,** 231-64.

MASTRONARDE, D. N. 2005. Automated electron microscope tomography using robust prediction of specimen movements. *J Struct Biol,* 152**,** 36-51.

MATTHEW, W. D., TSAVALER, L. & REICHARDT, L. F. 1981. Identification of a synaptic vesicle-specific membrane protein with a wide distribution in neuronal and neurosecretory tissue. *J Cell Biol,* 91**,** 257-69.

MICHELASSI, F., LIU, H., HU, Z. & DITTMAN, J. S. 2017. A C1-C2 Module in Munc13 Inhibits Calcium-Dependent Neurotransmitter Release. *Neuron,* 95**,** 577-590 e5.

MISURA, K. M., GONZALEZ, L. C., JR., MAY, A. P., SCHELLER, R. H. & WEIS, W. I. 2001. Crystal structure and biophysical properties of a complex between the N-terminal SNARE region of SNAP25 and syntaxin 1a. *J Biol Chem,* 276**,** 41301-9.

MISURA, K. M., SCHELLER, R. H. & WEIS, W. I. 2000. Three-dimensional structure of the neuronal-Sec1-syntaxin 1a complex. *Nature,* 404**,** 355-62.
NALEFSKI, E. A. & FALKE, J. J. 1996. The C2 domain calcium-binding motif: structural and functional diversity. *Protein Sci,* 5**,** 2375-90.
PAPKE, D., GONZALEZ-GUTIERREZ, G. & GROSMAN, C. 2011. Desensitization of neurotransmitter-gated ion channels during high-frequency stimulation: a comparative study of Cys-loop, AMPA and purinergic receptors. *J Physiol,* 589**,** 1571-85.
PARISOTTO, D., PFAU, M., SCHEUTZOW, A., WILD, K., MAYER, M. P., MALSAM, J., SINNING, I. & SOLLNER, T. H. 2014. An extended helical conformation in domain 3a of Munc18-1 provides a template for SNARE (soluble N-ethylmaleimide-sensitive factor attachment protein receptor) complex assembly. *J Biol Chem,* 289**,** 9639-50.
PARK, S., BIN, N. R., YU, B., WONG, R., SITARSKA, E., SUGITA, K., MA, K., XU, J., TIEN, C. W., ALGOUNEH, A., TURLOVA, E., WANG, S., SIRIYA, P., SHAHID, W., KALIA, L., FENG, Z. P., MONNIER, P. P., SUN, H. S., ZHEN, M., GAO, S., RIZO, J. & SUGITA, S. 2017. UNC-18 and Tomosyn Antagonistically Control Synaptic Vesicle Priming Downstream of UNC-13 in Caenorhabditis elegans. *J Neurosci,* 37**,** 8797-8815.
PEI, J., MA, C., RIZO, J. & GRISHIN, N. V. 2009. Remote homology between Munc13 MUN domain and vesicle tethering complexes. *J Mol Biol,* 391**,** 509-17.
PERIN, M. S., FRIED, V. A., MIGNERY, G. A., JAHN, R. & SUDHOF, T. C. 1990. Phospholipid binding by a synaptic vesicle protein homologous to the regulatory region of protein kinase C. *Nature,* 345**,** 260-3.
PINTACUDA, G., PARK, A. Y., KENIRY, M. A., DIXON, N. E. & OTTING, G. 2006. Lanthanide labeling offers fast NMR approach to 3D structure determinations of protein-protein complexes. *J Am Chem Soc,* 128**,** 3696-702.
POIRIER, M. A., XIAO, W., MACOSKO, J. C., CHAN, C., SHIN, Y. K. & BENNETT, M. K. 1998. The synaptic SNARE complex is a parallel four-stranded helical bundle. *Nat Struct Biol,* 5**,** 765-9.
PYOTT, S. J. & ROSENMUND, C. 2002. The effects of temperature on vesicular supply and release in autaptic cultures of rat and mouse hippocampal neurons. *J Physiol,* 539**,** 523-35.
RAMÓN Y CAJAL, S. 1909. *Histologie du système nerveux de l'homme & des vertébrés.,* Paris, Maloine.
REDDY-ALLA, S., BOHME, M. A., REYNOLDS, E., BEIS, C., GRASSKAMP, A. T., MAMPELL, M. M., MAGLIONE, M., JUSYTE, M., REY, U., BABIKIR, H., MCCARTHY, A. W., QUENTIN, C., MATKOVIC, T., BERGERON, D. D., MUSHTAQ, Z., GOTTFERT, F., OWALD, D., MIELKE, T., HELL, S. W., SIGRIST, S. J. & WALTER, A. M. 2017. Stable Positioning of Unc13 Restricts Synaptic Vesicle Fusion to Defined Release Sites to Promote Synchronous Neurotransmission. *Neuron,* 95**,** 1350-1364 e12.
RHEE, J. S., BETZ, A., PYOTT, S., REIM, K., VAROQUEAUX, F., AUGUSTIN, I., HESSE, D., SUDHOF, T. C., TAKAHASHI, M., ROSENMUND, C. & BROSE,

N. 2002. Beta phorbol ester- and diacylglycerol-induced augmentation of transmitter release is mediated by Munc13s and not by PKCs. *Cell,* 108**,** 121-33.

RICHMOND, J. E., DAVIS, W. S. & JORGENSEN, E. M. 1999. UNC-13 is required for synaptic vesicle fusion in C. elegans. *Nat Neurosci,* 2**,** 959-64.

RICHMOND, J. E., WEIMER, R. M. & JORGENSEN, E. M. 2001. An open form of syntaxin bypasses the requirement for UNC-13 in vesicle priming. *Nature,* 412**,** 338-41.

RIZO, J. 2018. Mechanism of neurotransmitter release coming into focus. *Protein Sci,* 27**,** 1364-1391.

RIZO, J., ROSEN, M. K. & GARDNER, K. H. 2012. Enlightening molecular mechanisms through study of protein interactions. *J Mol Cell Biol,* 4**,** 270-83.

RIZO, J. & SUDHOF, T. C. 1998. C2-domains, structure and function of a universal Ca2+-binding domain. *J Biol Chem,* 273**,** 15879-82.

RIZO, J. & SUDHOF, T. C. 2012. The membrane fusion enigma: SNAREs, Sec1/Munc18 proteins, and their accomplices--guilty as charged? *Annu Rev Cell Dev Biol,* 28**,** 279-308.

ROSAHL, T. W., GEPPERT, M., SPILLANE, D., HERZ, J., HAMMER, R. E., MALENKA, R. C. & SUDHOF, T. C. 1993. Short-term synaptic plasticity is altered in mice lacking synapsin I. *Cell,* 75**,** 661-70.

SAKAMOTO, H., ARIYOSHI, T., KIMPARA, N., SUGAO, K., TAIKO, I., TAKIKAWA, K., ASANUMA, D., NAMIKI, S. & HIROSE, K. 2018. Synaptic weight set by Munc13-1 supramolecular assemblies. *Nat Neurosci,* 21**,** 41-49.

SAKISAKA, T., YAMAMOTO, Y., MOCHIDA, S., NAKAMURA, M., NISHIKAWA, K., ISHIZAKI, H., OKAMOTO-TANAKA, M., MIYOSHI, J., FUJIYOSHI, Y., MANABE, T. & TAKAI, Y. 2008. Dual inhibition of SNARE complex formation by tomosyn ensures controlled neurotransmitter release. *J Cell Biol,* 183**,** 323-37.

SCHIAVO, G., BENFENATI, F., POULAIN, B., ROSSETTO, O., POLVERINO DE LAURETO, P., DASGUPTA, B. R. & MONTECUCCO, C. 1992. Tetanus and botulinum-B neurotoxins block neurotransmitter release by proteolytic cleavage of synaptobrevin. *Nature,* 359**,** 832-5.

SCHOCH, S., CASTILLO, P. E., JO, T., MUKHERJEE, K., GEPPERT, M., WANG, Y., SCHMITZ, F., MALENKA, R. C. & SUDHOF, T. C. 2002. RIM1alpha forms a protein scaffold for regulating neurotransmitter release at the active zone. *Nature,* 415**,** 321-6.

SHEN, N., GURYEV, O. & RIZO, J. 2005. Intramolecular occlusion of the diacylglycerol-binding site in the C1 domain of munc13-1. *Biochemistry,* 44**,** 1089-96.

SHERRINGTON, C. S. 1906. *The integrative action of the nervous system,* New Haven, CT, Yale University Press.

SHIN, O. H., LU, J., RHEE, J. S., TOMCHICK, D. R., PANG, Z. P., WOJCIK, S. M., CAMACHO-PEREZ, M., BROSE, N., MACHIUS, M., RIZO, J., ROSENMUND, C. & SUDHOF, T. C. 2010. Munc13 C2B domain is an activity-dependent Ca2+ regulator of synaptic exocytosis. *Nat Struct Mol Biol,* 17**,** 280-8.

SITARSKA, E., XU, J., PARK, S., LIU, X., QUADE, B., STEPIEN, K., SUGITA, K., BRAUTIGAM, C. A., SUGITA, S. & RIZO, J. 2017. Autoinhibition of Munc18-1 modulates synaptobrevin binding and helps to enable Munc13-dependent regulation of membrane fusion. *Elife,* 6.

SOLLNER, T., BENNETT, M. K., WHITEHEART, S. W., SCHELLER, R. H. & ROTHMAN, J. E. 1993a. A protein assembly-disassembly pathway in vitro that may correspond to sequential steps of synaptic vesicle docking, activation, and fusion. *Cell,* 75**,** 409-18.

SOLLNER, T., WHITEHEART, S. W., BRUNNER, M., ERDJUMENT-BROMAGE, H., GEROMANOS, S., TEMPST, P. & ROTHMAN, J. E. 1993b. SNAP receptors implicated in vesicle targeting and fusion. *Nature,* 362**,** 318-24.

STEVENS, D. R., WU, Z. X., MATTI, U., JUNGE, H. J., SCHIRRA, C., BECHERER, U., WOJCIK, S. M., BROSE, N. & RETTIG, J. 2005. Identification of the minimal protein domain required for priming activity of Munc13-1. *Curr Biol,* 15**,** 2243-8.

STEWART, J. C. 1980. Colorimetric determination of phospholipids with ammonium ferrothiocyanate. *Anal Biochem,* 104**,** 10-4.

SUDHOF, T. C. 2004. The synaptic vesicle cycle. *Annu Rev Neurosci,* 27**,** 509-47.

SUDHOF, T. C. 2013. Neurotransmitter release: the last millisecond in the life of a synaptic vesicle. *Neuron,* 80**,** 675-90.

SUDHOF, T. C. & ROTHMAN, J. E. 2009. Membrane fusion: grappling with SNARE and SM proteins. *Science,* 323**,** 474-7.

SUTTON, R. B., DAVLETOV, B. A., BERGHUIS, A. M., SUDHOF, T. C. & SPRANG, S. R. 1995. Structure of the first C2 domain of synaptotagmin I: a novel Ca2+/phospholipid-binding fold. *Cell,* 80**,** 929-38.

SUTTON, R. B., FASSHAUER, D., JAHN, R. & BRUNGER, A. T. 1998. Crystal structure of a SNARE complex involved in synaptic exocytosis at 2.4 A resolution. *Nature,* 395**,** 347-53.

SZULE, J. A. & COORSSEN, J. R. 2003. Revisiting the role of SNAREs in exocytosis and membrane fusion. *Biochim Biophys Acta,* 1641**,** 121-35.

TAKAMORI, S., HOLT, M., STENIUS, K., LEMKE, E. A., GRONBORG, M., RIEDEL, D., URLAUB, H., SCHENCK, S., BRUGGER, B., RINGLER, P., MULLER, S. A., RAMMNER, B., GRATER, F., HUB, J. S., DE GROOT, B. L., MIESKES, G., MORIYAMA, Y., KLINGAUF, J., GRUBMULLER, H., HEUSER, J., WIELAND, F. & JAHN, R. 2006. Molecular anatomy of a trafficking organelle. *Cell,* 127**,** 831-46.

TUCKER, W. C., WEBER, T. & CHAPMAN, E. R. 2004. Reconstitution of Ca2+-regulated membrane fusion by synaptotagmin and SNAREs. *Science,* 304**,** 435-8.

TUGARINOV, V., SPRANGERS, R. & KAY, L. E. 2004. Line narrowing in methyl-TROSY using zero-quantum 1H-13C NMR spectroscopy. *J Am Chem Soc,* 126**,** 4921-5.

UNGAR, D. & HUGHSON, F. M. 2003. SNARE protein structure and function. *Annu Rev Cell Dev Biol,* 19**,** 493-517.

VAN DEN BOGAART, G., MEYENBERG, K., DIEDERICHSEN, U. & JAHN, R. 2012. Phosphatidylinositol 4,5-bisphosphate increases Ca2+ affinity of synaptotagmin-1 by 40-fold. *J Biol Chem,* 287**,** 16447-53.
VAN DEN BOGAART, G., MEYENBERG, K., RISSELADA, H. J., AMIN, H., WILLIG, K. I., HUBRICH, B. E., DIER, M., HELL, S. W., GRUBMULLER, H., DIEDERICHSEN, U. & JAHN, R. 2011. Membrane protein sequestering by ionic protein-lipid interactions. *Nature,* 479**,** 552-5.
VAROQUEAUX, F., SIGLER, A., RHEE, J. S., BROSE, N., ENK, C., REIM, K. & ROSENMUND, C. 2002. Total arrest of spontaneous and evoked synaptic transmission but normal synaptogenesis in the absence of Munc13-mediated vesicle priming. *Proc Natl Acad Sci U S A,* 99**,** 9037-42.
VERHAGE, M., MAIA, A. S., PLOMP, J. J., BRUSSAARD, A. B., HEEROMA, J. H., VERMEER, H., TOONEN, R. F., HAMMER, R. E., VAN DEN BERG, T. K., MISSLER, M., GEUZE, H. J. & SUDHOF, T. C. 2000. Synaptic assembly of the brain in the absence of neurotransmitter secretion. *Science,* 287**,** 864-9.
WANG, D. & HIESINGER, P. R. 2013. The vesicular ATPase: a missing link between acidification and exocytosis. *J Cell Biol,* 203**,** 171-3.
WANG, S., CHOI, U. B., GONG, J., YANG, X., LI, Y., WANG, A. L., YANG, X., BRUNGER, A. T. & MA, C. 2017. Conformational change of syntaxin linker region induced by Munc13s initiates SNARE complex formation in synaptic exocytosis. *EMBO J,* 36**,** 816-829.
WATANABE, S., ROST, B. R., CAMACHO-PEREZ, M., DAVIS, M. W., SOHL-KIELCZYNSKI, B., ROSENMUND, C. & JORGENSEN, E. M. 2013. Ultrafast endocytosis at mouse hippocampal synapses. *Nature,* 504**,** 242-247.
WATERHOUSE, A., BERTONI, M., BIENERT, S., STUDER, G., TAURIELLO, G., GUMIENNY, R., HEER, F. T., DE BEER, T. A. P., REMPFER, C., BORDOLI, L., LEPORE, R. & SCHWEDE, T. 2018. SWISS-MODEL: homology modelling of protein structures and complexes. *Nucleic Acids Res,* 46**,** W296-W303.
WEBER, T., ZEMELMAN, B. V., MCNEW, J. A., WESTERMANN, B., GMACHL, M., PARLATI, F., SOLLNER, T. H. & ROTHMAN, J. E. 1998. SNAREpins: minimal machinery for membrane fusion. *Cell,* 92**,** 759-72.
WICKNER, W. & RIZO, J. 2017. A cascade of multiple proteins and lipids catalyzes membrane fusion. *Mol Biol Cell,* 28**,** 707-711.
WILHELM, B. G., MANDAD, S., TRUCKENBRODT, S., KROHNERT, K., SCHAFER, C., RAMMNER, B., KOO, S. J., CLASSEN, G. A., KRAUSS, M., HAUCKE, V., URLAUB, H. & RIZZOLI, S. O. 2014. Composition of isolated synaptic boutons reveals the amounts of vesicle trafficking proteins. *Science,* 344**,** 1023-8.
WILLIAMS, R. W. & HERRUP, K. 1988. The control of neuron number. *Annu Rev Neurosci,* 11**,** 423-53.
WILSON, D. W., WILCOX, C. A., FLYNN, G. C., CHEN, E., KUANG, W. J., HENZEL, W. J., BLOCK, M. R., ULLRICH, A. & ROTHMAN, J. E. 1989. A fusion protein required for vesicle-mediated transport in both mammalian cells and yeast. *Nature,* 339**,** 355-9.

WINTER, U., CHEN, X. & FASSHAUER, D. 2009. A conserved membrane attachment site in alpha-SNAP facilitates N-ethylmaleimide-sensitive factor (NSF)-driven SNARE complex disassembly. *J Biol Chem,* 284**,** 31817-26.

WOJCIK, S. M., TANTRA, M., STEPNIAK, B., MAN, K. N., MULLER-RIBBE, K., BEGEMANN, M., JU, A., PAPIOL, S., RONNENBERG, A., GURVICH, A., SHIN, Y., AUGUSTIN, I., BROSE, N. & EHRENREICH, H. 2013. Genetic markers of a Munc13 protein family member, BAIAP3, are gender specifically associated with anxiety and benzodiazepine abuse in mice and humans. *Mol Med,* 19**,** 135-48.

XU, J., CAMACHO, M., XU, Y., ESSER, V., LIU, X., TRIMBUCH, T., PAN, Y. Z., MA, C., TOMCHICK, D. R., ROSENMUND, C. & RIZO, J. 2017. Mechanistic insights into neurotransmitter release and presynaptic plasticity from the crystal structure of Munc13-1 C1C2BMUN. *Elife,* 6.

XU, Y., SU, L. & RIZO, J. 2010. Binding of Munc18-1 to synaptobrevin and to the SNARE four-helix bundle. *Biochemistry,* 49**,** 1568-76.

YANG, B., STEEGMAIER, M., GONZALEZ, L. C., JR. & SCHELLER, R. H. 2000. nSec1 binds a closed conformation of syntaxin1A. *J Cell Biol,* 148**,** 247-52.

YANG, X., WANG, S., SHENG, Y., ZHANG, M., ZOU, W., WU, L., KANG, L., RIZO, J., ZHANG, R., XU, T. & MA, C. 2015. Syntaxin opening by the MUN domain underlies the function of Munc13 in synaptic-vesicle priming. *Nat Struct Mol Biol,* 22**,** 547-54.

YU, I. M. & HUGHSON, F. M. 2010. Tethering factors as organizers of intracellular vesicular traffic. *Annu Rev Cell Dev Biol,* 26**,** 137-56.

ZHANG, O., KAY, L. E., OLIVIER, J. P. & FORMAN-KAY, J. D. 1994. Backbone 1H and 15N resonance assignments of the N-terminal SH3 domain of drk in folded and unfolded states using enhanced-sensitivity pulsed field gradient NMR techniques. *J Biomol NMR,* 4**,** 845-58.

ZHAO, M., WU, S., ZHOU, Q., VIVONA, S., CIPRIANO, D. J., CHENG, Y. & BRUNGER, A. T. 2015. Mechanistic insights into the recycling machine of the SNARE complex. *Nature,* 518**,** 61-7.

ZHOU, P., BACAJ, T., YANG, X., PANG, Z. P. & SUDHOF, T. C. 2013. Lipid-anchored SNAREs lacking transmembrane regions fully support membrane fusion during neurotransmitter release. *Neuron,* 80**,** 470-83.

ZHOU, Q., LAI, Y., BACAJ, T., ZHAO, M., LYUBIMOV, A. Y., UERVIROJNANGKOORN, M., ZELDIN, O. B., BREWSTER, A. S., SAUTER, N. K., COHEN, A. E., SOLTIS, S. M., ALONSO-MORI, R., CHOLLET, M., LEMKE, H. T., PFUETZNER, R. A., CHOI, U. B., WEIS, W. I., DIAO, J., SUDHOF, T. C. & BRUNGER, A. T. 2015. Architecture of the synaptotagmin-SNARE machinery for neuronal exocytosis. *Nature,* 525**,** 62-7.

ZHOU, Q., ZHOU, P., WANG, A. L., WU, D., ZHAO, M., SUDHOF, T. C. & BRUNGER, A. T. 2017. The primed SNARE-complexin-synaptotagmin complex for neuronal exocytosis. *Nature,* 548**,** 420-425.